

Atom interferometry with cold metastable helium

Citation for published version (APA):

Jansen, M. A. H. M. (2007). *Atom interferometry with cold metastable helium*. [Phd Thesis 1 (Research TU/e / Graduation TU/e), Applied Physics and Science Education]. Technische Universiteit Eindhoven.
<https://doi.org/10.6100/IR623089>

DOI:

[10.6100/IR623089](https://doi.org/10.6100/IR623089)

Document status and date:

Published: 01/01/2007

Document Version:

Publisher's PDF, also known as Version of Record (includes final page, issue and volume numbers)

Please check the document version of this publication:

- A submitted manuscript is the version of the article upon submission and before peer-review. There can be important differences between the submitted version and the official published version of record. People interested in the research are advised to contact the author for the final version of the publication, or visit the DOI to the publisher's website.
- The final author version and the galley proof are versions of the publication after peer review.
- The final published version features the final layout of the paper including the volume, issue and page numbers.

[Link to publication](#)

General rights

Copyright and moral rights for the publications made accessible in the public portal are retained by the authors and/or other copyright owners and it is a condition of accessing publications that users recognise and abide by the legal requirements associated with these rights.

- Users may download and print one copy of any publication from the public portal for the purpose of private study or research.
- You may not further distribute the material or use it for any profit-making activity or commercial gain
- You may freely distribute the URL identifying the publication in the public portal.

If the publication is distributed under the terms of Article 25fa of the Dutch Copyright Act, indicated by the "Taverne" license above, please follow below link for the End User Agreement:

www.tue.nl/taverne

Take down policy

If you believe that this document breaches copyright please contact us at:

openaccess@tue.nl

providing details and we will investigate your claim.

Atom Interferometry with Cold Metastable Helium

PROEFSCHRIFT

ter verkrijging van de graad van doctor aan de
Technische Universiteit Eindhoven, op gezag van de
Rector Magnificus, prof.dr.ir. C.J. van Duijn, voor een
commissie aangewezen door het College voor
Promoties in het openbaar te verdedigen
op dinsdag 20 maart 2007 om 16.00 uur

door

Maarten Arnoldus Hubertus Maria Jansen

geboren te Waalwijk

Dit proefschrift is goedgekeurd door de promotoren:

prof.dr. K.A.H. van Leeuwen

en

prof.dr. H.C.W. Beijerinck

Druk: Universiteitsdrukkerij Technische Universiteit Eindhoven
Ontwerp Omslag: Paul Verspaget

CIP-DATA LIBRARY TECHNISCHE UNIVERSITEIT EINDHOVEN

Jansen, Maarten Arnoldus Hubertus Maria

Atom Interferometry with Cold Metastable Helium / by

Maarten Arnoldus Hubertus Maria Jansen. -

Eindhoven : Technische Universiteit Eindhoven, 2007. - Proefschrift. -

ISBN 978-90-386-2212-5

NUR 926

Trefw.: atomaire bundels / laserkoeling / interferometrie /
quantum mechanica / atomen; wisselwerkingen

Subject Headings: atomic beams / laser cooling / gravity / atom optics /
particle interferometry / wave mechanics / atom-photon collisions

Contents

1	Introduction	1
1.1	Interference & Interferometry	1
1.2	Atom Interferometry	3
1.3	Applications	5
1.4	This Thesis	5
2	Atom Beam Design	9
2.1	Introduction	9
2.1.1	Requirements	9
2.2	Laser Cooling	11
2.2.1	Velocity Dependent Radiation Force	12
2.2.2	Radiation Force with Magnetic Field Gradients	13
2.2.3	Cooling Limits	16
2.3	Atomic Beam Setup	16
2.3.1	Overview	16
2.3.2	Metastable Atom Source	16
2.3.3	Atom Beam Collimation	18
2.3.4	Atom Beam Slowing	19
2.3.5	Atom Beam Compression	23
2.4	Conclusion	26
3	Atomic Beam Diagnostics	29
3.1	Introduction	29
3.2	Detectors	29
3.2.1	Atom Beam Intensity Calibration	30
3.3	Collimator	32
3.4	Time-of-Flight measurements	33
3.4.1	Supersonic Source Velocity Distribution	33
3.4.2	Zeeman Slower	36
3.5	Atom Beam Compression	38
3.5.1	Focussing	39
3.5.2	Compression	39
3.5.3	Directional Control	42
3.6	Conclusions	44

4	Lasers	47
4.1	Introduction	47
4.2	Passive Isolation	48
4.3	Control Theory	48
4.4	Frequency Lock on Atomic Transition	50
4.5	Frequency Offset Lock	51
	4.5.1 Phase Locked Loops	51
	4.5.2 Implementation	54
4.6	Conclusions	54
5	Atomic Bragg Scattering	57
5.1	Introduction	57
5.2	Mathematical Description	58
5.3	Eigenvector Approach	61
5.4	Acceptance Angle	63
5.5	Demkov Model	64
5.6	Measurements	68
5.7	Optimal waist	70
5.8	Conclusion	72
6	Interferometer Theory	75
6.1	Introduction	75
6.2	Free Propagation	76
	6.2.1 WKB approximation	76
	6.2.2 Classical Trajectories	78
6.3	Laser Interaction	79
6.4	Total Phase Calculation	81
	6.4.1 Approximations	81
	6.4.2 Calculations Outline	84
	6.4.3 Results	85
6.5	Design Considerations	87
6.6	Conclusion	92
7	Laser Pulse Length Effects in Time-Based Atom Interferometers	95
7.1	Introduction	95
7.2	Experiment	96
7.3	External Hamiltonian	97
7.4	Laser Interaction	100
7.5	Atom Interferometry	102
7.6	Phase Calculations	104
	7.6.1 Parameters	105
	7.6.2 Full Wavefunction Integral	106
	7.6.3 Results	108
	7.6.4 Semiclassical Approximation	110
7.7	Conclusions	113

Appendix	114
A.1 Mathematical Tools	114
A.2 Elimination of the external Hamiltonian	115
A.3 Coordinate Transformations	118
A.4 Laser Interaction	119
A.5 Atom Interferometer	120
A.5.1 Short Pulse Limit	122
A.6 Eigenfunctions	122
8 Concluding Remarks	127
Summary	131
Samenvatting	133
Dankwoord	135
Curriculum Vitae	137

Chapter 1

Introduction

1.1 Interference & Interferometry

Interference is the superposition of waves and oscillations resulting in a new wave pattern. This effect is ubiquitous and universal for all waves whether they are e.g. water waves, sound or light. All these waves are locally described by an amplitude and a phase. Depending on the phase difference the interference of two waves can result in an increase to an amplitude that equals the sum of those two waves or the decrease to the amplitude difference. In every day life, however, often a wave pattern is the combination of many different waves with a large range of frequency and wavelength. The phases of the wave components thus vary rapidly, both in space and time, such that the interferences tend to cancel and an overall structural interference pattern is hard to recognize.

An interferometer is a device that is specifically designed to make a clear and simple interference pattern and utilize this to perform measurements. Many different types of interferometers exist, but they are all based on the principle that one wave is split in two and that these two partial waves are recombined again. Examples are the double slit interferometer (Fig. 1.1) and the Mach-Zehnder interferometer (Fig. 1.2). The double slit interferometer gives a spatial interference pattern on the screen. The Mach-Zehnder interferometer (when perfectly aligned) does not give a spatial profile, but the interference is revealed in the relative intensity on the detector. Interferometers are used to translate the phase difference between the two paths to an intensity signal on a detector. Because the phase of a wave often is much more sensitive to small perturbations than the amplitude, an interferometer can be used as a very precise measuring instrument for these perturbing effects.

The phase resolution of an interferometer is the minimum phase change that can be detected. This is equal to the phase change at which the detector intensity has changed by more than the detection noise. It is obvious that lower noise and larger overall signal increase the phase resolution. The resolution, however, also depends on the sensitivity which is the change in intensity, scaled to the total signal at the input, per unit change of the phase. In Fig. 1.3 the phase sensitivity is given by the slope of the lines. For an ideal 2-path interferometer the maximum sensitivity is 1. A real setup, however, has imperfections that introduce phase noise which decreases the sensitivity. Fast fluctuations

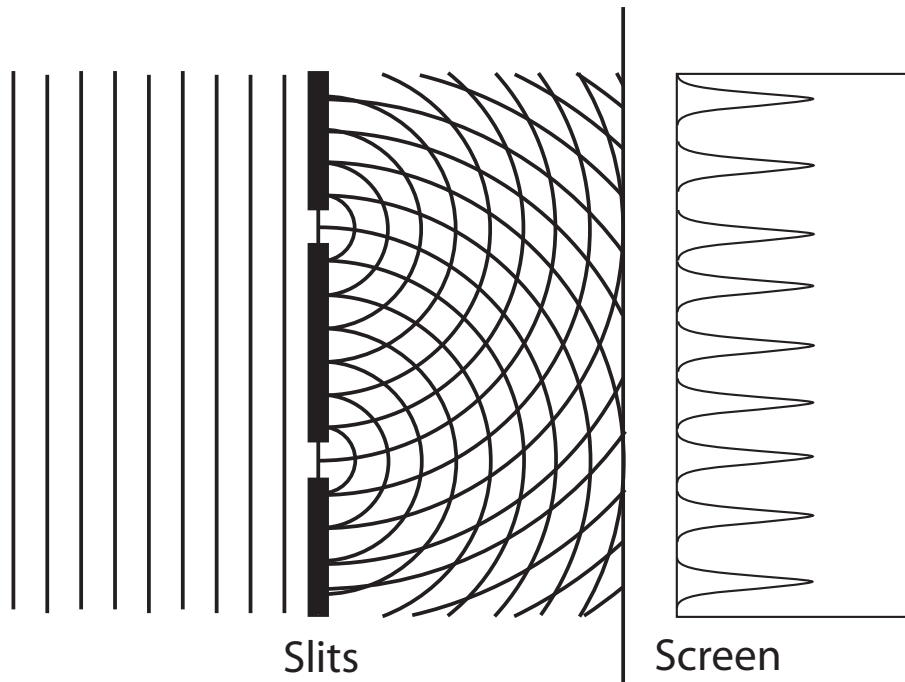


Figure 1.1: Double slit interferometer. One plane wave enters from the left and is transmitted through two slits. These slits then act as two coherent sources that emit spherical waves. The interference of the two waves from the two slits form a spatial interference signal on the screen.

in the phase, for example, average out to a signal that oscillates with reduced amplitude. An example of the resulting signal is given in Fig. 1.3 by the dashed line where the sum is taken over signals that have a Gaussian distribution in the relative phase with an RMS width of approximately 1 rad. In that case the detector signal changes much less with the phase and a large fraction of the signal is lost to a constant offset. Sometimes the quality of the interference signal is expressed in terms of the contrast which is the ratio between the amplitude of the interference signal and the offset. It is clear that for a good interferometer one strives for a low phase noise and a high contrast.

As mentioned, interference occurs for all oscillations, with perhaps the earliest observation in water waves. The first interferometers were developed in the 19th century and used light as the interfering wave. From the beginning, these optical interferometers had a large impact on physics and they are still being improved for more precise measurements. In applied physics these interferometers are used for a large variety of measurements of e.g. material properties like refractive indices and surface properties, and for high accuracy length measurements. In fundamental physics, optical interferometers have played a large role in answering fundamental questions, as exemplified by the Michelson-Morley experiment which ruled out the ether theory.

With the advent of quantum theory in the 20th century and the discovery of the matter-wave duality of particles, the concept of interferometry was extended to matter waves, first to electrons [1] and later to neutrons [2]. The first atom interferometers were developed in the early 1990's. This development has been motivated by two important factors. First,

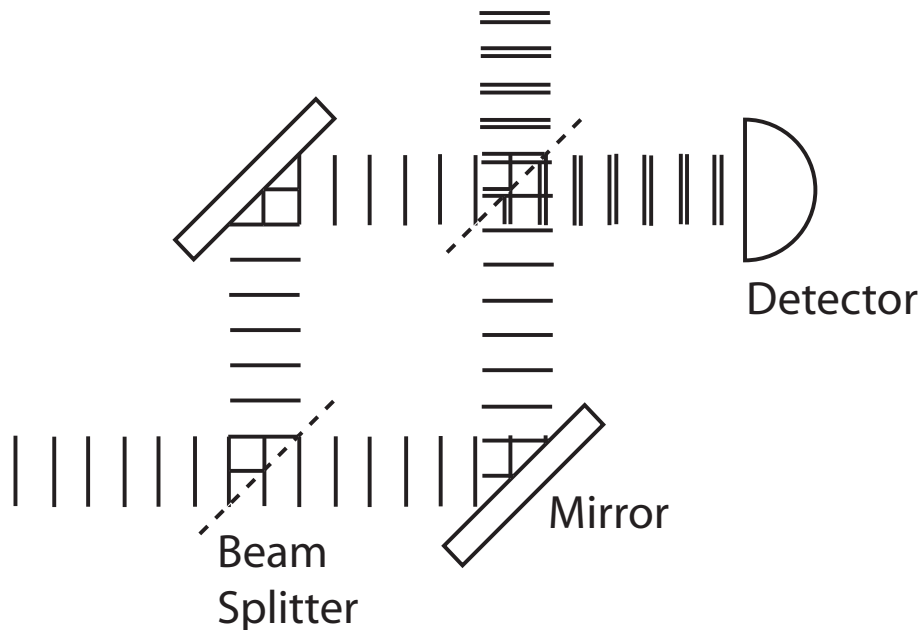


Figure 1.2: Mach-Zehnder interferometer. One wave that enters from the left is split by the first beamsplitter and recombined on a second. When the interferometer is perfectly aligned there is no spatial interference signal. In that case a phase difference between the two paths sets how the intensity is divided between the two output ports.

massive particles have the possibility for much shorter wavelengths and might thus allow for much more sensitive measurements than light. Second, these particles have an ever richer internal structure which allows for completely new kinds of interferometers.

1.2 Atom Interferometry

There is a vast range of configurations for optical interferometers, like the two that were mentioned in the previous section. Atom interferometers, however, come in even more varieties. Many atom interferometers have a direct analogue of optical interferometer in which the atom wave is split in two spatially separated parts. It is however also possible to split the atomic wavefunction over the internal states, e.g. by partial excitation by laser pulses. In that case the “paths” of the interferometer are the different histories between two parts of the wavefunction. The basic principle of operation, however, is the same for all interferometers. The atoms are coherently split and an interference pattern is observed when the split parts of the wavefunction are brought back together on the same position and in the same internal state.

The many different kinds of atom interferometers each have their own advantages and disadvantages and are all optimized to measure different quantities (for an overview see Refs [3] and [4]). Roughly they can be divided into two categories: beam or spatial interferometers and pulsed or time-based interferometers. In a time-based interferometer a small number of atoms is exposed to a sequence of fields and laser pulses that are turned

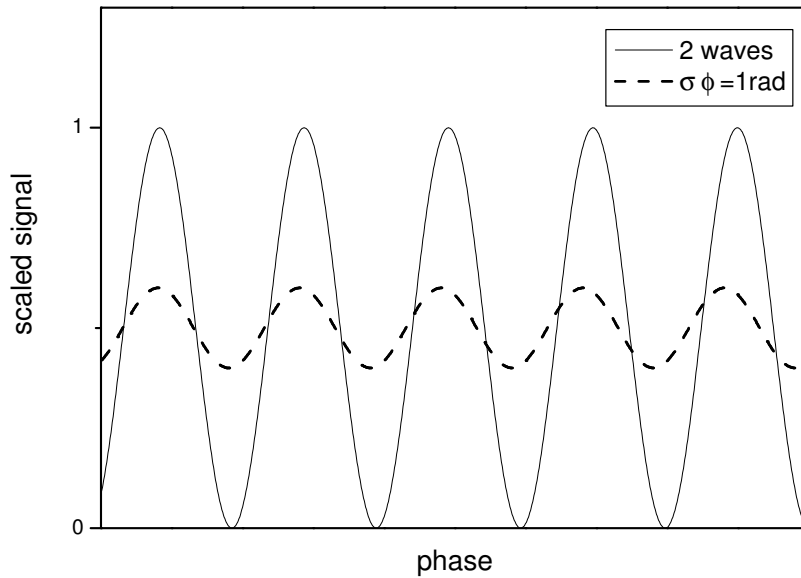


Figure 1.3: Examples of interference patterns where the detector signal is scaled to the total intensity at the input. The thin line is the signal for an ideal 2 path interferometer. The dashed line is the averaged signal of a whole range of waves with a Gaussian spread of 1 rad in phase.

on and off. Separation and detection of the atoms is done with laser pulses that act on all atoms at the same time. Because the interference signal depends on the timing of the fields and laser pulses which can easily be performed with high accuracy, this type is often used for precision measurements. The disadvantage is that the atoms are hardly accessible for objects and fields that are to be studied. In a spatial interferometer the atoms enter the setup at one end, move through beamsplitters, mirrors and interaction sections and are detected at the other end of the setup. In this type of interferometer it is relatively easy to add fields and objects and effects requiring an actual spatial separation can be studied. The interferometer that is described in this thesis is of this kind.

The largest disadvantage of a spatial interferometer is that the phase difference induced by the objects and fields usually is proportional with the transit time. The quality of the interference signal and the accuracy with which the phase can be determined are thus related to the velocity spread of the atoms. This typically limits the precision of these measurements. This thesis describes a detailed study of this effect and concludes with some design criteria that allow for any required level of precision.

There are numerous examples for the beamsplitters and mirrors that are needed to split, bring back and recombine the atoms. Here, I will limit myself to a few examples. For splitting the atoms in two internal states, an RF field [5] or laser pulses [6] can be applied. The latter option can simultaneously spatially separate the paths through the absorbed momentum. Periodic structures, either mechanical gratings [7] or standing light waves [8], can be used to spatially split the beam through diffraction. In this category, standing light

waves offer more flexibility and allow optimization for single order diffraction by using the atomic analogue of Bragg scattering. It is this last option that is extensively studied in this thesis (Chapter 5).

1.3 Applications

Although atom interferometry is a relatively new area of research, it already has found many applications [3,4]. The most famous use to date is precision spectroscopy and its use in atom clocks [9]. Other uses lie among others in its high sensitivity to accelerations [10] and rotation [11], the possibility to study atom-atom interactions [12] and precision measurements of polarizabilities [13]. Contributions to fundamental themes are the direct observation of the quantization of the electromagnetic field [14], high accuracy measurement of the fine-structure constant [15] and insight in the duality of quantum mechanics through which-way experiments [16]. This summation is certainly not exhaustive and many more applications will be developed in the future.

The interferometer that is described in this thesis has been designed primarily for measurements on the quantum properties of the electromagnetic field in high-finesse cavities. In the simplest example of such an experiment, the cavity is inserted in one arm of the interferometer. If there is light in the cavity, the atom will experience an energy shift in the cavity that leads to a change in the phase. This phase change is detected by the interferometer. By using a high finesse cavity it is possible to get a detectable phase shift for even a single photon [17]. In that case this interferometer opens a new window for studying the dynamics of the quantized electromagnetic field.

1.4 This Thesis

The interferometer is presently ready for the first tests. This thesis describes crucial elements of the design, extensive tests of the performance of these elements, and a theoretical study of the many possible sources of errors in the signal of the interferometer.

The interferometer needs two main ingredients: an atom beam and coherent beamsplitters. The beamsplitters are created by off-resonant standing light fields on which the atom beam is diffracted by Bragg scattering. Then three rather stringent demands on the atom beam follow from some simple argumentation. First, the atom beam has to be collimated to a transverse velocity spread that is smaller than one photon recoil to avoid scattering to multiple orders. Second, the atoms have to be slowed to a longitudinal velocity of approximately 250 m/s to obtain a spatial separation of several mm between the two paths. And third, the spread in longitudinal velocity has to be as small as possible to get an optimal interference signal. These three criteria can most easily be met with a beam of metastable helium in the metastable $\{1s2s\}^3S_1$ state. Helium has a large photon recoil velocity which allows for large splitting angles and it can be laser cooled with commercially available laser diodes ($\lambda = 1083$ nm).

In Chapters 2 and 3 the design of this atom beam is explained and diagnostics are developed that verify the operation of the atom beam. Indeed, the beam meets all the

requirements and we obtain a longitudinal velocity spread of only 1% and a flux of some hundreds per second. The preparation of this beam uses four laser cooling sections that cool, slow and compress the atom beam. The setups of the lasers that are used in these sections and the setup of the laser that is used in the interferometer are described in Chapter 4.

The atom beam is split by Bragg scattering on a standing light field. This process allows clean scattering, i.e. the atoms are split in only two beams. However, the process is selective to the transverse velocity. In Chapter 5 the acceptance range is optimized where a delicate balance was sought between a maximum number of atoms that can be scattered, while keeping the diffraction to other orders to a minimum.

A full design of the interferometer can not be made without knowing the sensitivity of the phase to all parameters of the setup. Therefore, an analysis was made in Chapter 6 that takes into account all alignment errors, position and velocity spread of the atom beam and any possible potentials and rotation. The largest contributions to the interferometer phase are calculated and translated into concrete design criteria.

The last chapter of this thesis (Chap. 7) is the result of a collaboration with the group of Prof. M. Kasevich at Stanford University. They are preparing an interferometer that will measure differences in gravity to a new level of precision. In this chapter the effect of the length of laser pulses on the interferometer phase is investigated. This effect is usually ignored, but the results show that the pulse length does play a role at these high levels of precision and can greatly complicate the interpretation of the interference fringes.

References

- [1] L. Marton, J. Arol Simpson, and J.A. Suddeth, *Phys. Rev.* **90**, 490 (1953).
- [2] H. Maier-Leibnitz and T. Springer, *Z.Phys.* **167**, 368 (1962).
- [3] *Atom Interferometry*, edited by Paul R. Berman (Academic Press, New York, 1997).
- [4] J. Baudon, R. Mathevet, and J. Robert, *J. Phys. B* **32**, R173 (1999).
- [5] Norman F. Ramsey, *Phys. Rev.* **78**, 695 (1950).
- [6] Ch. J. Bordé, *Phys. Lett. A* **140**, 10 (1989).
- [7] David W. Keith, Christoffer R. Ekstrom, Quentin A. Turchette, and David E. Pritchard, *Phys. Rev. Lett.* **66**, 2693 (1991).
- [8] Philip E. Moskowitz, Philip L. Gould, and David E. Pritchard, *J. Opt. Soc. Am. B* **2**, 1784 (1985).
- [9] G. Wilpers, T. Binnewies, C. Degenhardt, U. Sterr, J. Helmcke, and F. Riehle, *Phys. Rev. Lett* **89**, 230801 (2002).
- [10] A. Peters, K.Y. Chung, and S. Chu, *Metrologia* **38**, 25 (2001).

-
- [11] T.L. Gustavson, P. Bouyer, and M.A. Kasevich, Phys. Rev. Lett. **78**, 2046 (1997).
 - [12] Arthur Widera, Olaf Mandel, Markus Greiner, Susanne Kreim, Theodor W. Hänsch, and Immanuel Bloch, Phys. Rev. Lett. **92**, 160406 (2004).
 - [13] Christopher R. Ekstrom, Jörg Schmiedmayer, Michael S. Chapman, Troy D. Hammond, and David E. Pritchard, Phys. Rev. A **51**, 3883 (1995).
 - [14] G. Nogues, A. RauschenBeutel, S. Osnaghi, M. Brune, and S. Haroche, Nature **400**, 239 (1999).
 - [15] Andreas Wicht, Joel M. Hensley, Edina Sarajlic and Steven Chu, Phys. Scr. **T102**, 82 (2002).
 - [16] S. Dürr, T. Nonn, and G. Rempe, Phys. Rev. Lett. **81**, 5705 (1998).
 - [17] G.T. Jansen, *Bragg Diffraction of He* by a Standing Light Wave*, internal report, Eindhoven University of Technology (2001)

Chapter 2

Atom Beam Design

2.1 Introduction

This chapter describes the preparation of the atom beam that is necessary before the atoms can be used in the interferometer. As we will see, we need a beam with well defined direction and velocity, much better than is achieved with conventional atom beam sources. Fortunately, with the advent of laser cooling it has become possible to manipulate beams of neutral atoms and greatly reduce the temperature, divergence and velocity of the atoms. This technique allows us to reach the stringent demands that are set by the atom interferometer.

Still, the preparation of the atoms is no easy task. As we will see, it takes a setup of 9 m long that includes 4 laser cooling sections and above that an extra selection stage with two small apertures. This setup has been designed [1] and implemented [2] in the past, and this chapter will give an overview along with some new insights that were developed since then.

2.1.1 Requirements

To build an atom interferometer that has a macroscopic spatial separation (≈ 1 cm) between the two paths, there are some strict requirements on the atom beam that have to be met.

The first requirement follows from the limitations of the beam splitters and the mirrors that coherently split and recombine the two paths of the interferometer. The separation between the two arms is determined by the difference in transverse velocity, the longitudinal velocity of the atoms and the length of the interferometer. The atom beam is generally separated by the interaction of the beam with light. By stimulated absorption and emission cycles, momentum is transferred from the light to the atom. An example of such a scheme is Bragg Scattering which will be used in our setup, as described in Chapter 5. The maximum amount of coherently transferred momentum is limited in all of these beam splitting schemes. With Bragg Scattering, a transfer of 16 photon recoils has been demonstrated by Koolen [2, 3] and it seems reasonable that this can be extended to 20 recoils. The maximum separation between the arms will be halfway, at 1 m for a 2 m

long interferometer. To get a macroscopic separation of 7 mm the longitudinal velocity of the atoms then can be no higher than 250 m/s. The beams that are produced in the supersonic expansion (Sec. 2.3.2) are considerably faster than this. This means that the atoms will have to be slowed down.

The second criterion is that the interference fringes have to be visible. An atom experiences a phase shift between the two paths of the interferometer if these two paths have an energy difference ΔE . This energy shift could be caused by a number of effects, such as the Zeeman effect or inertial effects (for details see Chapter 6) and an interferometer is designed to measure at least one of these. Two distinct atoms can experience a different phase shift when they cross the interferometer in a (slightly) different way, for example because they have a different velocity. The spread in interference phase for a beam with longitudinal velocity spread σ_v is given by

$$\sigma_\phi = \frac{\Delta E T \sigma_v}{\hbar v}, \quad (2.1)$$

where T is the total transit time. If this spread in phase is larger than π the fringes will be averaged out and the interferometer phase can not be determined. It is clear from this formula that a narrow velocity distribution allows the detection of larger energy differences between the two arms at the end of the interferometer. From another point of view, one sees that in the case of a narrow velocity distribution the constraints on stray fields can be relaxed.

A third consideration is on the transverse velocity distribution of the atom beam. First of all, such a distribution will give a variation in the atoms phase shift and therefore a blurring of the interference signal, in a similar way as the longitudinal velocity. Above that, the beam splitting process by single order Bragg scattering only works on atoms within a very small transverse velocity interval, with a width of typically one photon recoil (see Chapter 5). To get a well defined splitting ratio of the atom beam, the transverse velocity spread of the atoms must not be larger than this. For metastable Helium this sets the maximum transverse velocity spread to 0.05 m/s.

Finally, the flux of atoms has to be high enough to do experiments within a reasonable time span. This requires a count rate on the final detector that is well above 1 atom/s.

In conclusion, we need an atom beam that has a low longitudinal velocity, a low divergence and sufficient flux. It is not at all easy to meet all these requirements. It takes a setup that comprises four laser cooling sections and additional transverse velocity selection by two collimating apertures [1, 2]. In this chapter all sections of the setup will be described, giving the basic theory of their operation. We will start by an explanation of the principle of laser cooling in Section 2.2, including three specific configurations that are used in the setup. The optical molasses configuration (Subsection 2.2.1) is used to collimate the atom beam as it emerges from the source. Subsequently, the atoms are slowed down in the Zeeman slower with the compensation technique and finally compressed in a 2D MOT (Subsec. 2.2.2). In Section 2.3 the implementation of these devices in the actual setup is described.

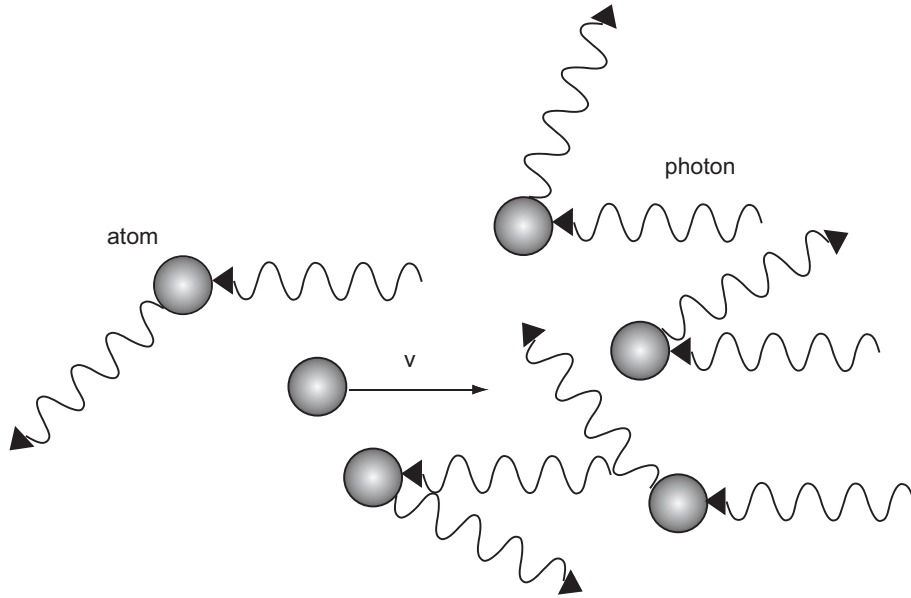


Figure 2.1: Working principle of the spontaneous radiation force. The absorbed photon has a well defined direction, while the direction of emitted photon is randomly distributed in space

2.2 Laser Cooling

The “working horse” of the atom beam preparation setup is the spontaneous radiation force (first proposed in 1975 [4, 5] and observed in 1985 [6]). In different configurations of lasers and magnetic fields, this force is able to slow, cool, and compress the atoms (see [7] and [8] for an overview). All of these techniques are used in the preparation setup. Insight in the operation principles of the cooling section therefore relies on an understanding of the spontaneous radiation force.

The origin of the spontaneous radiation force can be understood from Fig. 2.1 in which an ensemble of atoms is irradiated by a laser beam coming from the right. The atoms absorb light from a well defined direction, but emit this light in a random direction. Averaged over many absorption-spontaneous emission cycles, the atom thus acquires a net momentum change in the direction of the laser beam. For cooling, one needs a velocity selective force. For the spontaneous radiation force, this selectivity arises from the Doppler shift in combination with the finite width of the absorption profile [9].

The number of photons that is scattered per unit of time per atom is given by $n_e \Gamma$, with n_e the fraction of atoms in the excited state and Γ the decay rate. The excitation fraction has a Lorentzian profile as a function of the laser frequency, with a maximum that is given by $n_{e,max} = s/(2(s+1))$. The saturation parameter s is given by $s = I/I_{sat}$, with I_{sat} the saturation intensity that depends on the atomic transition that is used. For large laser intensity, the excitation at resonance reaches a maximum of 1/2, saturating the absorption rate. Each cycle will increase the atoms momentum by the photon momentum¹ $\hbar \mathbf{k}$, where \mathbf{k} is the wavevector of the laser. Taking into account the absorption profile, the radiation

¹boldfaced symbols denote vectors

force of a single running laser wave takes the form:

$$\mathbf{F} = \frac{\hbar \mathbf{k} \Gamma s}{2(1 + s + (2\Delta_{eff}/\Gamma)^2)}. \quad (2.2)$$

Here, Δ_{eff} is the effective detuning between the atomic resonance frequency and the laser frequency. The maximum force is at resonance ($\Delta_{eff} = 0$) and high saturation parameter and is equal to $\mathbf{F}_{max} = \hbar \mathbf{k} \Gamma / 2$. For metastable helium this force gives a maximum acceleration of $4.7 \times 10^5 \text{ ms}^{-2}$.

There are several effects that contribute to the effective detuning. First of all there is the laser detuning, which is the difference between the laser frequency ω_l and the unperturbed atomic transition frequency ω_0 , $\Delta_l = \omega_l - \omega_0$. Second, as the atoms are moving along the laser beam, the effective laser frequency that is experienced by the atoms is shifted by the Doppler shift $\Delta_D = -\mathbf{k} \cdot \mathbf{v}$. This is the origin of the velocity dependence of the radiation pressure and the basis for any cooling based on the spontaneous emission force. The last contribution to the effective detuning originates from any energy shift that the atoms experience. The most relevant for typical laser cooling configurations is the Zeeman shift in a magnetic field \mathbf{B} . In a magnetic field the energy of each atomic level is changed by an amount $\Delta E_Z = -\boldsymbol{\mu} \cdot \mathbf{B} = \mu_B B g_i m_i$, where $\boldsymbol{\mu}$ is the magnetic moment, g_i the Landé factor and m_i is the magnetic quantum number relative to the magnetic field, B is the strength of the magnetic field and μ_B is the Bohr magneton. The two atomic states that are involved with the optical transition generally feel a different energy shift, causing the resonance frequency to change. The resonance frequency then changes with the magnetic field. By using an inhomogeneous magnetic field, the radiation force can be made position dependent.

2.2.1 Velocity Dependent Radiation Force

Optical Molasses

Consider the situation where an atom moves along two antiparallel laser beams with the same frequency, slightly below the atomic transition frequency [9]. In Figure 2.2, the effective laser frequency ($\omega_l + \Delta_D$) of both lasers is plotted versus the velocity of the atom. Resonance is reached when this effective frequency is equal to the transition frequency (ω_0). The graph shows that for the two beams this happens for opposite velocity of the atom. In effect, as the atom moves towards one laser, the associated Doppler shift brings the atom closer to resonance with the approached laser, while it moves the atom away from resonance with the other laser (see Fig. 2.2). The atom will absorb more atoms from this counter-propagating laser and thus feel a force opposite to its own velocity, i.e, a decelerating force.

For low intensity ($s \ll 1$), i.e, ignoring stimulated emission, the total force by the lasers can be approximated by the vector sum of the radiation force from each laser:

$$\mathbf{F} = \mathbf{F}_{laser1} + \mathbf{F}_{laser2}. \quad (2.3)$$

The laser detuning has the same sign for both lasers, but the Doppler shift is opposite as the atom moves away from one laser and towards the other. The resulting force is depicted

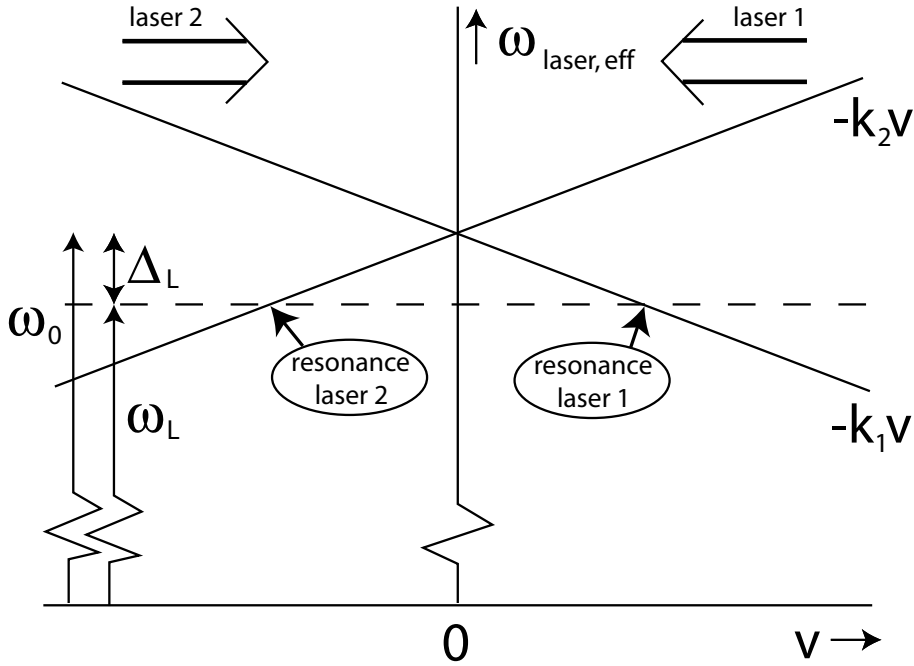


Figure 2.2: Frequency diagram for an optical molasses setup. Because the two laser are anti parallel, the associated Doppler shift is opposite. For a red detuned laser a moving atom will always be closer to resonance with the laser beam that propagates in the opposite direction

in Fig. 2.3 as a function of the atoms velocity for the $2s^3S_1 \rightarrow 2p^3P_2$ transition in helium, with $\Delta_l = -\Gamma/2$ and $s=2$. For atoms that move slower than the so-called capture velocity $v_c = -\Delta_l/k$, this force can be approximated to be linear with the velocity, thus acting as a pure friction force:

$$\mathbf{F} \approx \frac{8\hbar s(\Delta_l/\Gamma)}{(1 + s + (2\Delta_l/\Gamma)^2)^2} \mathbf{k}(\mathbf{k} \cdot \mathbf{v}) \equiv -\vec{\beta}\mathbf{v}. \quad (2.4)$$

This principle can be extended to 2 and 3 dimensions by adding orthogonal pairs of counter-running laser beams, thus providing the possibility of cooling in all directions.

2.2.2 Radiation Force with Magnetic Field Gradients

Magnetic Field as Compensation

The optical molasses scheme only damps the velocity of the atom. There is no dependence of the force on the position of the atoms and therefore trapping or focussing is not possible. This changes when an inhomogeneous magnetic field is applied. As mentioned, each atomic level will be shifted in energy by this field and thus the effective detuning will contain a position dependent contribution $\Delta_B = -\mu_B B(\mathbf{r})(g_e m_e - g_g m_g)/\hbar$. This position

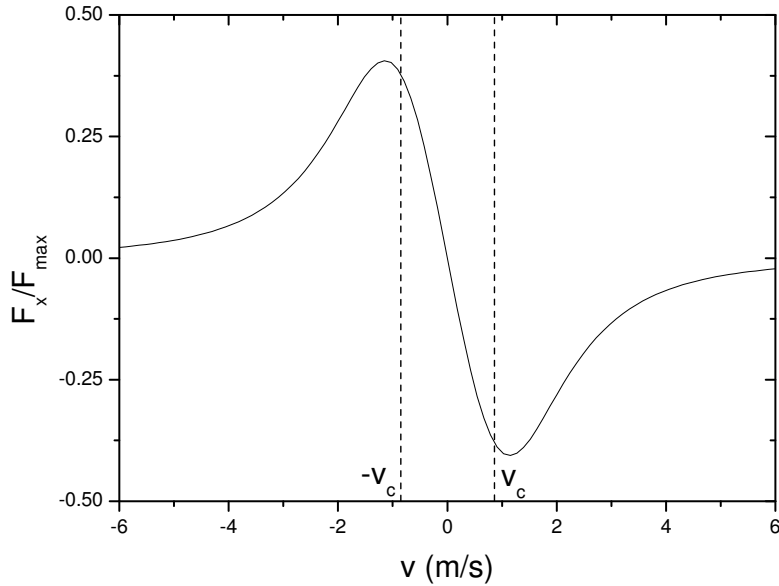


Figure 2.3: Velocity dependence of the decelerating force in Doppler cooling. Numerical values are used of the helium $2s^3S_1 \rightarrow 2p^3P_2$ transition, with $\Delta_l = -\Gamma/2$ and $s=2$

dependence can, for example, be used to compensate for the changing Doppler shift as an atom is decelerated by a laser. Without the magnetic field, the atom would quickly lose resonance. With the compensation resonance is retained much longer, making it possible to decelerate the atom over much larger velocity ranges. This is the operating principle of the Zeeman slower (Sec. 2.3.4).

Magneto-Optical Trap

To use the radiation force to focus or trap the atoms, this force has to be in opposite direction for atoms that are on opposite sides of the lens or trap. To achieve this, the contribution of the (position dependent) Zeeman shift to the effective detuning has to be opposite for the two counter-propagating lasers. For this two lasers with opposite, circular polarization (σ^+/σ^-) are used and a magnetic field that is zero in the center and increases linearly with the position along the laser beams [10].

The polarization of the laser determines which magnetic substate the atoms are excited to. For a $J = 0 \rightarrow J = 1$ transition with circularly polarized light, there are only two possibilities: $m_J = \pm 1$. In Fig. 2.4, the energies of all involved sublevels are drawn versus the position x . As in Fig. 2.2, resonance is reached when the laser frequency matches the energy difference between ground and excited state. In a magnetic field, the Zeeman shift for the two accessible excited states is opposite. As each laser can only address one of the two excited states, this Zeeman shift can be used to bring the atom closer to resonance with either one of the two laser beams. In a Magneto-Optical Trap (MOT), with a linearly

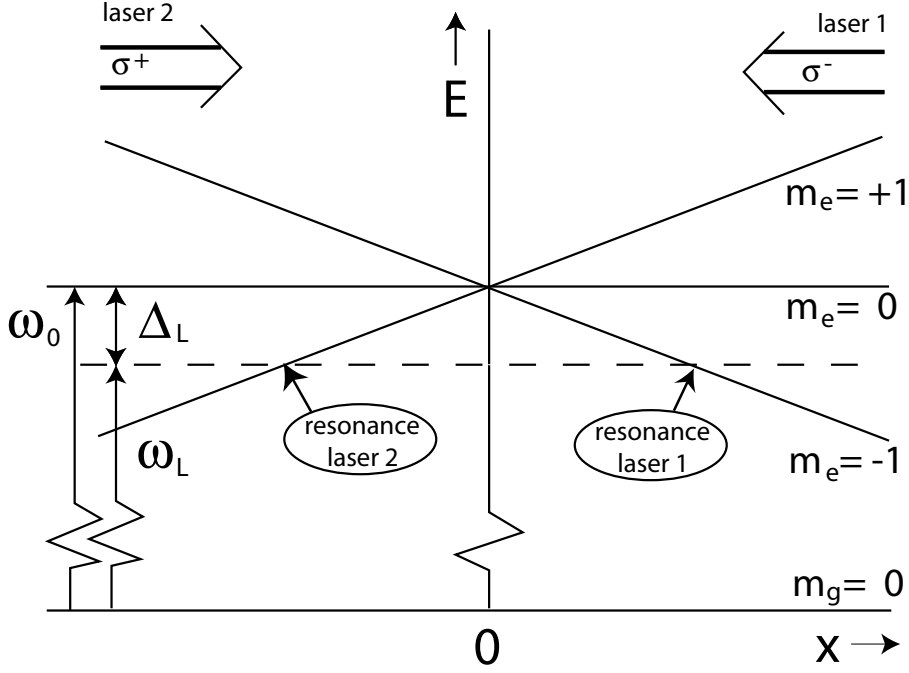


Figure 2.4: Energy diagram for a MOT setup and an atom at rest. The position dependence of the magnetic field brings the atoms closer to resonance with the laser that pushes them back to the center of the trap

increasing magnetic field and $B = 0$ in the center of the trap, atoms at rest will be closer to resonance with the laser that pushes them back to the center and the atoms will thus feel an effective trapping force.

With the position dependence of the Zeeman shift, the optical force is now a function of both position and velocity. The total force of the two laser beams can be calculated in the same way as in Section 2.2.1. By expanding the force around $\mathbf{k} \cdot \mathbf{v} + \mu_B \nabla B \cdot \mathbf{x} / \hbar = 0$ we get:

$$\mathbf{F} \approx -\vec{\beta} \mathbf{v} - \vec{\kappa} \mathbf{x}. \quad (2.5)$$

This describes the damped oscillation of the atom in a MOT with a damping coefficient $|\vec{\beta}|$, given by Eq. 2.4 and a spring constant $|\vec{\kappa}|$ equal to

$$\vec{\kappa} \mathbf{x} \equiv \frac{-8s(\Delta_l/\Gamma)\mu'}{(1+s+(2\Delta_l/\Gamma)^2)^2} \mathbf{k} (\nabla B \cdot \mathbf{x}), \quad (2.6)$$

$$\mu' = (g_e m_e - g_g m_g) \mu_B. \quad (2.7)$$

The transition in metastable helium that is used for laser cooling has $J = 1 \rightarrow J = 2$. This makes the process more complicated than in the $J = 0 \rightarrow J = 1$ case, as there are now more magnetic sublevels. Extra optical pumping processes redistribute the atoms over these sublevels and have to be taken into account when calculating the total cooling force.

The principle of operation, however, remains the same. As long as the atom is far from equilibrium optical pumping is limited and Eq. 2.6 with a fixed μ' is a good approximation.

This scheme is easily extended to more dimensions. Three orthogonal pairs of counter-running σ^+/σ^- beams and a magnetic quadrupole field cool and compress the atoms in three dimensions, forming a magneto-optical atom trap (MOT). We will use two pairs of laser beams in a two dimensional quadrupole field such that the atoms are focussed and compressed in the direction perpendicular to the beam axis.

2.2.3 Cooling Limits

The analysis of the previous sections would suggest that there is no limit on the cooling process and the atoms come to a full stop, resulting in a temperature $T=0$. In reality, there is also heating by the lasers that limits the lowest temperature that can be achieved. It arises from the discrete momentum steps that the atoms undergo with each absorption and emission [9]. For a 1-dimensional model of optical molasses, the temperature at which the cooling and heating processes reach equilibrium is called the Doppler temperature, which is given by $T_D = \hbar\Gamma/(2k_B)$. For metastable helium cooled on the $2s^3S_1 \rightarrow 2p^3P_2$ transition this amounts to $T_D = 39 \mu\text{K}$, with a corresponding Doppler velocity $v_D = \sqrt{\langle v^2 \rangle} = \sqrt{k_B T_D / m} = 0.28 \text{ m/s}$.

2.3 Atomic Beam Setup

2.3.1 Overview

This section describes the design of the setup that is used to create an atomic beam that meets the requirements as set in Sec. 2.1. The restrictions on the transverse and longitudinal velocity distribution could in principle be met by a beam preparation setup that only comprises a Zeeman slower and a pair of collimating apertures. Simulations [1,11], however, showed that this would result in a count rate that is approximately 1 atom per hour. This is of course completely unacceptable and therefore three extra transverse cooling and compression stages were added to increase the on-axis beam brightness. A schematic of the total resulting setup is given in Fig. 2.5. The total length of the setup from source to 2D-detector is more than 9 m. The pressure in the setup is kept at the 10^{-8} mbar level by 7 turbo pumps, backed with 2 scroll pumps [11].

2.3.2 Metastable Atom Source

The beam of metastable helium atoms is produced by a discharge-excited supersonic expansion. Electron impact is the only way to excite the atoms because of the high excitation energy of the atoms (19.8 eV), which is much larger than the photon energy of available lasers. Therefore, a DC discharge partially excites the atoms to the metastable $2s^3S_1$ state with an efficiency of approximately 10^{-5} [12]. Because a collision of a metastable atom with an other atom will likely cause the metastable atom to decay back to the ground state, the atoms will have to be excited just before they enter the vacuum. This is achieved by

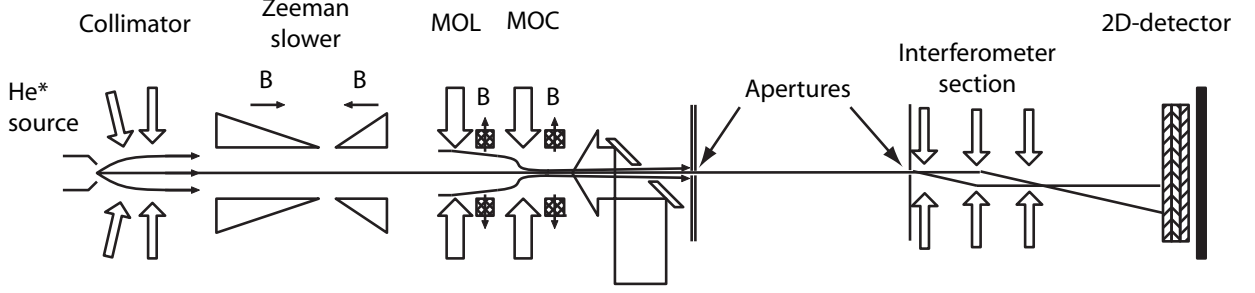


Figure 2.5: Schematic representation of the total atom beam setup.

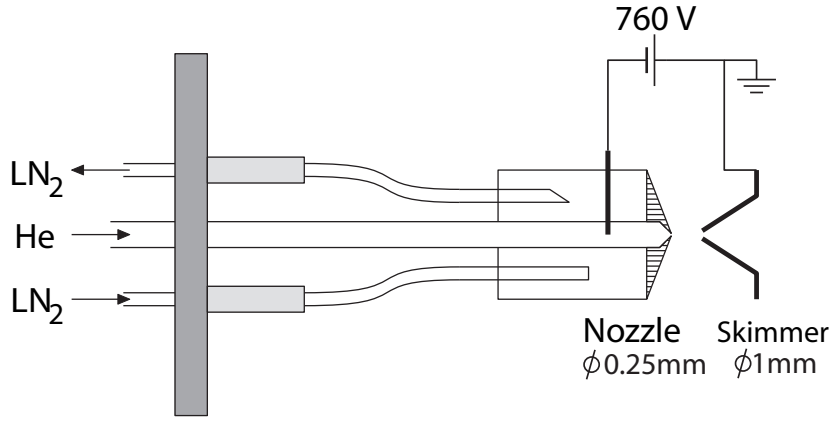


Figure 2.6: Cross-section of the liquid nitrogen cooled metastable helium source.

running the discharge from an electrode through the nozzle to the grounded skimmer (see Fig. 2.6).

The parameters of the expansion of the gas through the nozzle into the vacuum are chosen such that the flow is supersonic. This has the advantage that the longitudinal velocity distribution is much narrower than an ordinary thermal expansion. The velocity distribution is described by

$$P(v)dv \propto \left(\frac{v}{u}\right)^3 \exp\left[-\left(\frac{v-u}{u}\right)^2 S^2\right] dv. \quad (2.8)$$

The speed ratio S is defined as the ratio of the flow velocity u over the characteristic velocity, which determines the velocity spread. The value of this ratio is set by parameters of the source, like the temperature T_{source} and the pressure p_{source} , summarized in the source parameter Ξ [13]:

$$\Xi = 4.47 \times 10^4 \left[\frac{\text{K}^{4/3} \text{m}^2}{\text{J}} \right] p_{source} d_{n,eff} T_{source}^{-4/3}. \quad (2.9)$$

The effective nozzle diameter $d_{n,eff}$ is smaller than the geometric diameter because of

boundary layers in the flow profile. The speedratio for helium then can be calculated from:

$$S = 19.3 \left(\frac{\Xi}{100} \right)^{0.495}. \quad (2.10)$$

The source parameter also has an influence on the flow velocity:

$$u = \frac{u_\infty}{\sqrt{1 + \frac{3}{2S^2}}}, \quad (2.11)$$

$$u_\infty = \sqrt{\frac{5kT_{source}}{m}}. \quad (2.12)$$

If the speed ratio is high enough ($S \gg 1$), the flow velocity is only set by the temperature of the gas in the reservoir, T_{source} . By cooling the reservoir with liquid nitrogen, this temperature is reduced from approximately 400 K to 200 K, giving an average velocity of 1200 m/s.

In a supersonic flow the total flux of atoms in the expansion is given by:

$$\dot{N} = 0.513 n_0 \beta_0 \pi \frac{d_{n,eff}^2}{4}, \quad (2.13)$$

where $n_0 = p_{source}/k_B T_{source}$ is the density in the reservoir and $\beta_0 = (2k_B T_{source}/m)^{1/2}$ the thermal velocity. It follows from this equation that a higher source pressure increases the flux of atoms. It should be noted, however, that increasing the source pressure increases both the number of atoms that return from the skimmer and the average density of the background gas in the vacuum chamber. Both of these effects increase the chance that a metastable atom collides with another atom and subsequently is de-excited. This limits the total gain of metastable atoms, giving an optimal source pressure. Typical beam intensities that can be achieved are $\approx 10^{14} \text{ s}^{-1} \text{ sr}^{-1}$ [14].

2.3.3 Atom Beam Collimation

The atom beam as it emerges from the nozzle has a cubed cosine intensity profile as a function of the angle with the beam axis, resulting in an RMS divergence of approximately 0.5 rad. This means that the atom beam expands rapidly, reducing the beam intensity. To increase the downstream intensity, a pair of optical molasses in both transverse directions to the beam axis is placed directly after the skimmer. The transverse motion of the atoms is cooled and the divergence of the beam is reduced.

The collimator works on the principle of optical molasses as described in Sec. 2.2.1, using two orthogonal pairs of counterpropagating laser beams that are created by circulating and retroreflecting one single laser beam. As mentioned in that paragraph, the cooling force and therefore the time it takes to cool the atoms depends on the laser detuning. Too large a detuning will result in a small cooling force and a remaining divergence of the atom beam at the end of the interaction region. On the other hand, a small laser detuning will decrease the number of atoms that are cooled, because of a resulting decrease of the capture velocity $v_c = -\Delta_l/k$. Atoms that have a transverse velocity much larger than this capture velocity

will experience no cooling force and are not collimated. Because the transverse velocity distribution from the source is very broad (≈ 700 m/s) a lot can be gained by increasing the capture velocity.

A technique to combine a large capture efficiency with a low final divergence is the curved wavefront technique (see Fig. 2.7, [15,16]). By giving the laser beams a small angle α along the propagation direction of the atoms, an effective Doppler shift $\Delta_{eff} = \Delta_l - kv\alpha$ is introduced. Because all (retro-reflected) beams have the same angle with the beam axis, this Doppler shift is identical for each beam. This Doppler shift then acts as an effective overall laser detuning which depends on the angle α . When the laser beam is slightly focussed the angle α changes with the transverse position in the laser beam, giving a curved wavefront. With the curved wavefront technique, this angle is large at the beginning of the interaction. This gives a large effective detuning, allowing for a large capture velocity and thus a large number of atoms that is captured. Along the propagation axis, the angle becomes smaller, optimizing the actual cooling process. In effect, we have created an atomic funnel in velocity space.

The maximum capture velocity that can be achieved this way is limited by the maximum radiation force and the interaction time and can be estimated by

$$v_{cap,max} = \frac{\hbar k \Gamma L}{2Mv_{\parallel}}. \quad (2.14)$$

We use an interaction length L of 0.17 m. Combined with the longitudinal velocity from the source of 1200 m/s this estimate of the maximum capture velocity for metastable helium amounts to 65 m/s or an angle of 54 mrad. Simulations [2] show that the actual capture velocity is a factor 2 smaller, with a capture angle of 25 mrad.

The purpose of the collimator is to increase the flux of atoms at the end of the total beam setup. Because the Zeeman slower gives a large divergence to the atom beam the settings for an optimal final flux may not correspond to a minimum divergence after the collimator. The optimal settings will rather correspond to a situation where a maximum number of atoms is collimated just enough to be captured by the 2D compression stage (Sec. 2.3.5). Because the total final flux is the result of a complicated interplay between the different sections, it is difficult to predict the optimal settings for the collimator exactly and they will have to be optimized experimentally.

2.3.4 Atom Beam Slowing

After the collimator, the atoms still have an average longitudinal velocity of 1200 m/s and have to be slowed down. This is achieved by a so called Zeeman-Slower in which the atoms are decelerated by the radiation force of a counter propagating laser beam [17]. When they slow down, however, they experience a change in Doppler shift and quickly lose resonance with the laser. Without any compensation, the maximum change in velocity is $\approx \Gamma/k = 1.7$ m/s. Obviously, the changing Doppler shift has to be compensated for. This is achieved with the Zeeman shift by an inhomogeneous magnetic field.

The laser beam is circularly polarized (σ^+) and in the beginning of the slower, the atoms are pumped to the $|m_g = +1\rangle \leftrightarrow |m_e = +2\rangle$ sublevel system. The Zeeman shift

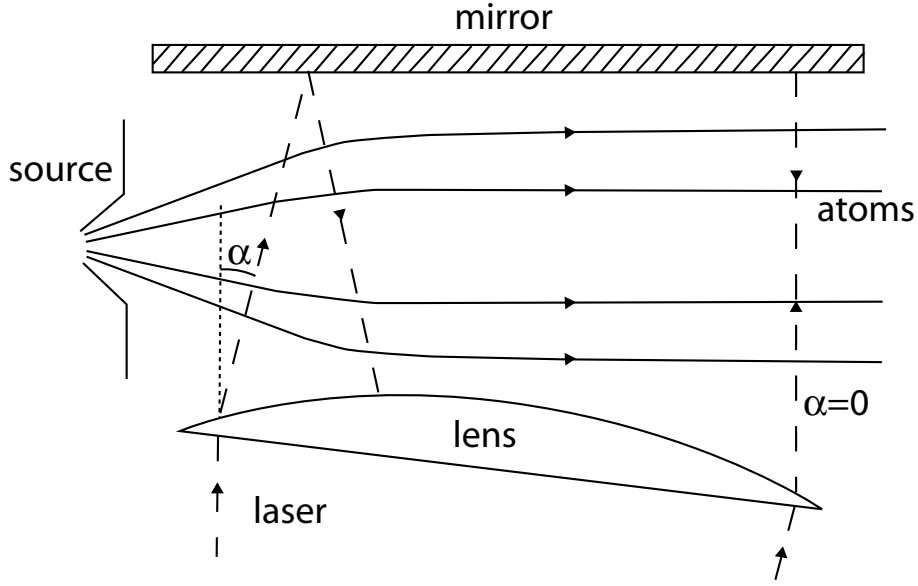


Figure 2.7: Principle of collimation with a curved wavefront technique. A slightly focussed laser beam is directed with a small angle along the atom beam, producing an effective laser frequency chirp.

of this subsystem is equal to $\mu_B B(z)/\hbar$. The magnetic field is position dependent and is designed such that the atoms are in resonance with the laser continuously.

$$\Delta_{eff} = \Delta_l - \frac{\mu_B}{\hbar} B(z) + kv_{\parallel} = 0. \quad (2.15)$$

A constant deceleration a of the atoms over time gives a position dependent velocity

$$v(z) = v_0 \sqrt{1 - \frac{z}{z_0}}, \quad (2.16)$$

where v_0 is the initial velocity and $z_0 = v_0^2/2a$ is the position where the atoms would come to a standstill if the deceleration would continue. For helium at the maximum radiation force, with $v_0 = 1200$ m/s this would give $z_0 = 1.5$ m. To allow for a margin on the actual deceleration of the atoms, however, the total length of the Zeeman slower was made twice as long. Matching the magnetic field to the velocity profile gives the optimal field

$$B(z) = \frac{\hbar}{\mu_B} \left(\Delta_l + k \sqrt{v_0^2 - (v_0^2 - v_f^2) \frac{z}{L}} \right). \quad (2.17)$$

The field is created by two separate solenoids, producing fields in opposite direction. This allows us to independently set the fields at the entrance and at the exit of the slower.

In more detail, the slowing process can be understood from Fig. 2.8. In this graph the magnetic field profile is schematically drawn (right axis). Given the magnetic field strength and the fixed laser detuning, there is a specific velocity at which the atoms are in resonance with the laser (Eq. 2.15). We will call this velocity the resonance velocity. It has the same profile as the magnetic field, with values that are indicated on the left axis. Also drawn

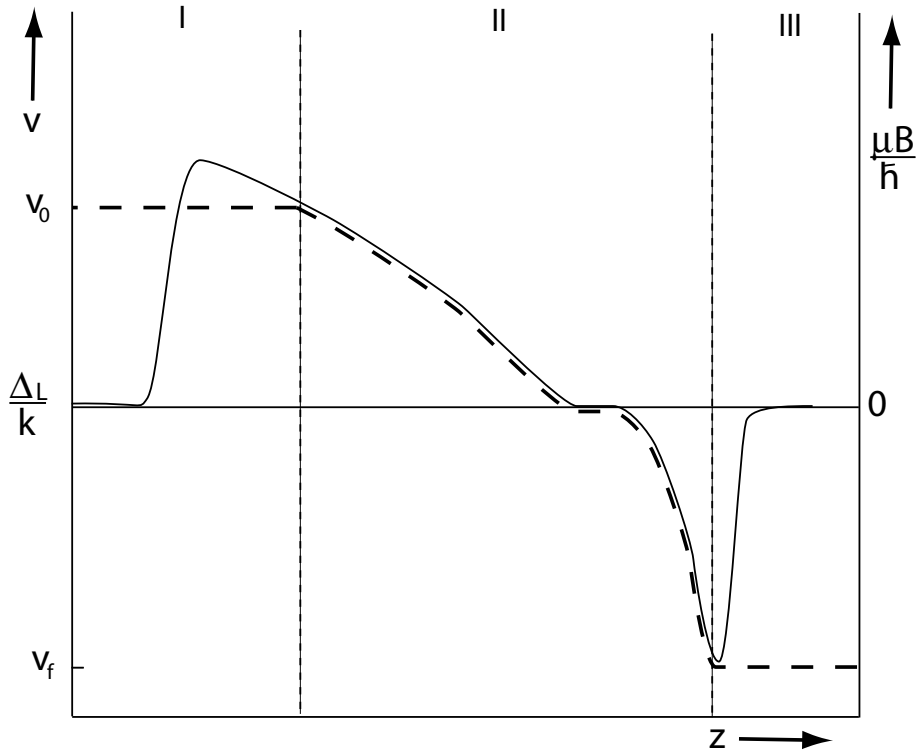


Figure 2.8: Working principle of the slowing process in the Zeeman slower. The magnetic field profile is drawn (solid line, right axis) together with the associated resonance velocity (left axis). The dashed line indicates the velocity of an atom that enters with a velocity smaller than the maximum capture velocity.

in Fig. 2.8 is the velocity of an atom that enters the slower with a velocity that is smaller than the maximum resonance velocity.

The slowing process can then be divided in three phases. In phase I, the atom enters the magnetic field. The atom experiences a swiftly increasing magnetic field. To stay in resonance with the associated resonance velocity, it would have to be accelerated which is impossible in this configuration. The effective interaction time with the laser is only very short and there will hardly be any change in the atoms velocity. Further downstream, the magnetic field decreases again and at the point where the local resonance velocity is equal to the velocity of the atom, the atom again feels the decelerating force. This time the change in resonance velocity corresponds to a deceleration. During phase II, the atom stays in resonance and is slowed down continuously. At the end of the slower the atom will reach the point with a minimum magnetic field. After this point, the resonance velocity increases again, and the atom can no longer follow. The atom loses resonance with the laser and remains at the velocity it had at the point of minimum field (phase III). In this idealized view, the maximum capture velocity is thus determined by the laser detuning and the magnetic field maximum at the entrance of the slower. The exit velocity is set by the field strength at the end.

Magnetic Field Imperfections

Now let's take a look at the actual deceleration of the atom. If the atom is to stay on resonance, the required acceleration can be calculated from the position dependence of the resonance velocity (Eq. 2.15)

$$a_{res} = \frac{dv_{res}}{dt} = \frac{dv_{res}}{dz} \frac{dz}{dt} = \frac{dv_{res}}{dz} v_{res} = \frac{\mu_B}{\hbar k} \frac{dB}{dz} v_{res}. \quad (2.18)$$

The required acceleration is thus proportional to the local magnetic field gradient. If at some point the local field gradient makes the required acceleration higher than the maximum acceleration of the radiation force, the atom can not follow the resonance velocity profile. The atom then will exit the slower at a higher velocity than intended. The margin of error on the acceleration is a factor of 2, so a doubling of the local field gradient would cause severe problems. The resonance condition has a finite width Γ , allowing some averaging of the field gradient. This averaging length can be estimated by:

$$L_{av} = \frac{\Delta v_{tol}}{dv_{res}/dz} \approx \frac{\Gamma L_{slower}}{k(v_0 - v_f)} = 5 \text{ mm}. \quad (2.19)$$

Clearly, the tolerance is not large, and the B fields have to be designed very carefully.

Transverse expansion

The Zeeman slower slows and cools the longitudinal velocity of the atom beam, but this comes at the expense of the atom beam divergence. As the spontaneous emission recoils are omnidirectional, while the slowing action acts only along the beam axis the scattered photons induce diffusion in both transverse directions. The induced spread in transverse velocity can be estimated from an evaluation of the random walk of the atom in velocity space, giving:

$$\sigma_{v\perp} = \frac{2}{3} \sqrt{N} v_{rec}, \quad (2.20)$$

where v_{rec} is the photon recoil velocity and N is the number of scattered photons $N = (v_0 - v_f)/v_{rec}$. If we slow the atoms from 1200 m/s to 250 m/s, this amounts to $\sigma_{v\perp} = 6$ m/s or a divergence of the atom beam of 24 mrad. Clearly, the transverse motion of the atoms has to be cooled again.

A second concern is the diameter of the atom beam at the end of the slower. This can be calculated by considering the final position of each atom. The final position of the atom is the vector sum of each momentum kick times the time between scattering and the atom reaching the end of the Zeeman slower. The average length of this position vector then gives the RMS width of the atom beam:

$$\sigma_x = \frac{2}{3} \sqrt{\sum_{i=0}^N x_i^2} = \frac{2}{3} v_{rec} \Delta t \sqrt{\sum_{i=0}^N (N - i)^2} \approx \frac{2}{3} v_{rec} \Delta t \sqrt{\frac{1}{3} N^3}. \quad (2.21)$$

Here, Δt is the average time between emission of the photons $\Delta t = T_{slower}/N = 2L_{slower}/N(v_0 + v_f)$. If we slow the atoms from 1200 m/s to 250 m/s the width amounts to $\sigma_x = 15$ mm. Cooling the atoms thus is not enough, we will have to compress the atom beam as well.

2.3.5 Atom Beam Compression

Compression and cooling of the atom beam is done with the Magneto-Optical Trap technique as described in Section 2.2.2. Instead of taking one long interaction section, the compressor is divided in two sections, reducing the required total amount of laser power. The first section, called the Magneto-Optical Lens (MOL), is designed to focus the broad atom beam into a relatively small beam [18]. The second stage, the Magneto-Optical Compressor (MOC), is positioned at the focus of the lens and compresses and cools the atoms into a narrow and collimated beam [19].

I will describe the processes again for a $J = 0 \rightarrow J = 1$ transition, keeping in mind that the processes for helium are in reality more complicated due to the presence of magnetic sublevels. Also, the described theory is 1-dimensional, while the actual setup has a two-dimensional configuration. The principle of operation, however, remains the same.

With the Magneto-Optical force given by Equation 2.5 it is straightforward to derive the equation of motion

$$m \frac{d^2 x(t)}{dt^2} - \beta \frac{dx(t)}{dt} - \kappa \cos(\theta) x(t) = \kappa \sin(\theta) v_z t. \quad (2.22)$$

Here we have introduced an angle θ between the laser and the magnetic field gradient to investigate its effect on the atom beam. This way we get some insight in the tolerances of the alignment and we see in what way we can use the MOL and the MOC to steer the atom beam.

Equation 2.22 describes a driven and damped oscillation. The exact form of the trajectory depends on the relative size of β and κ . In the MOC these parameters are chosen such that oscillation is roughly critically damped with a damping time that is much less than the interaction time. In the MOL the magnetic field gradient is much weaker and the oscillation is overdamped. Not all transverse motion is stopped and the MOL is therefore slightly more difficult to describe. We will therefore start with a description of the MOC, although in the setup this is located after the MOL.

Magneto-Optical Compressor

The compressor is designed to “guide” the atoms to the axis of the atom beam setup and to cool them so that they remain on this axis. For optimal operation, the magnetic field gradient is large (up to 0.8 T/m), giving maximum damping to the transverse motion. In Figure 2.9 the solutions to Eq. 2.22 are drawn for a number of atoms that enter the MOC at different position and velocity. The magnetic field gradient is assumed constant and the zero-axis of the field (the line on which $B = 0$) is drawn in the graph, at an angle θ with the optical axis for reference. The laser intensity is constant in the interaction region (between $z = 0$ and $z = 0.1$ m). After the interaction region, the trajectories are extrapolated using the final velocity.

The oscillation at the end of the interaction region is completely damped. The atoms position and velocity at the end of the interaction region (at $t = T = L_{MOC}/v_z$) can then be approximated by:

$$x(T) \approx v_{os} T + x_{os} \quad (2.23)$$

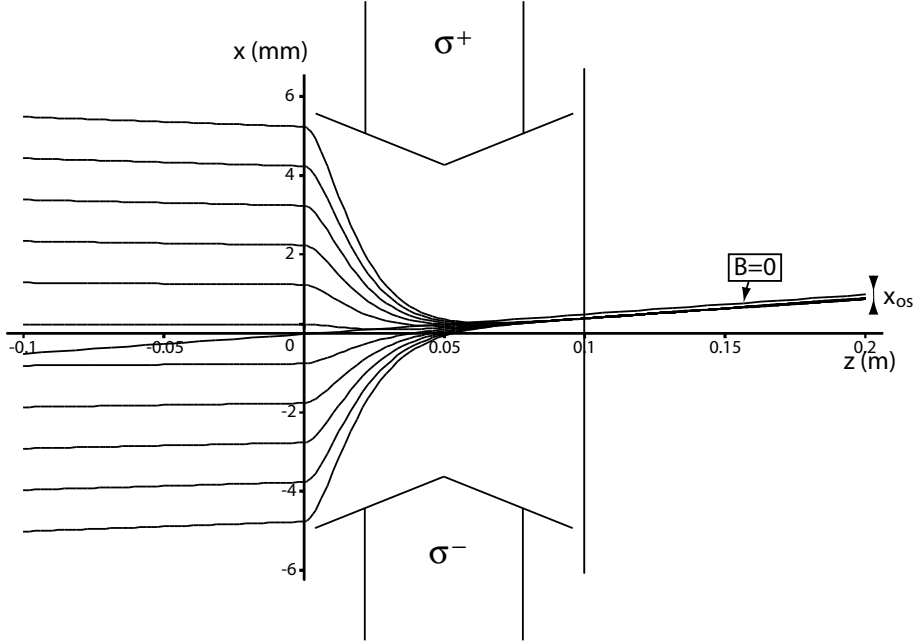


Figure 2.9: Atomic trajectories in the MOC as calculated by the damped oscillator model. The interaction with the light takes place between the two vertical lines. Also drawn is the $B=0$ axis which acts as the reference axis to which the atoms are cooled.

$$v_x(T) \approx v_{os} \quad (2.24)$$

$$x_{os} = \frac{-\beta v_z \tan(\theta)}{\kappa \cos(\theta)} = \frac{-k v_z \tan(\theta)}{\mu \nabla B \cos(\theta)} \quad (2.25)$$

$$v_{os} = v_z \tan(\theta). \quad (2.26)$$

Both the final position and velocity are independent of their initial values and so all atoms leave the compressor moving in the same direction

$$x(t) = v_{os}t + x_{os} \quad t > T. \quad (2.27)$$

For $\theta = 0$ the atoms are thus perfectly compressed to the magnetic field axis ($x=0$) and cooled to $v_x = 0$. When there is an angle between the laser and the magnetic field gradient, the atoms are directed along the direction of the zero-axis of the magnetic field, with an angle θ . The atoms will then not be compressed to exactly the zero-axis, but the beam will have an offset of x_{os} . This offset can be understood as the position where the Zeeman shift compensates the Doppler shift that is induced from the relative movement between the magnetic axis and the optical axis (from the atoms point of view).

There are two remarks that have to be made about this simple harmonic oscillator model. First, this highly simplified model suggest that the atoms are perfectly compressed and cooled to a beam with no width and no divergence. In reality, the final divergence and beam width have some finite value. Second, the linear approximation of the cooling force is only valid for $|\mathbf{k} \cdot \mathbf{v} + \mu_B \nabla B \cdot \mathbf{x}/\hbar| < \Delta_l$. If the effective detuning is much larger than the laser detuning, the atoms will not be compressed. We need a high gradient for

optimal compression, but this means that even for small deviations of the atom from the optical axis, the effective detuning will become too large. For a gradient of 0.8 T/m and $v_x = 0$, the so-called capture diameter is only 0.6 mm. Although it is possible to increase the capture radius by matching the transverse velocity of the atom to its position, the margins of error are very small.

To increase the effective capture radius of the compressor two measures were taken. Firstly, the magnetic field gradient dB/dx is smaller at the beginning of the interaction region (≈ 0.1 T/m). This allows for a larger capture radius, while at the end of the interaction region, the gradient is large for optimal compression. For a further increase of the effective capture range of the compressor, a second compression stage was added to the setup: the Magneto-Optical Lens.

Magneto-Optical Lens

In the MOL the magnetic field gradient is chosen such that the motion is overdamped. There are two characteristic damping times of which one is (much) longer than the interaction time and one is shorter. The resulting trajectories are drawn in Fig. 2.10. Unlike the MOC, the trajectories in the MOL are not completely damped, but still depend on the initial velocity and position of the atom. The position and the transverse velocity of the atom at the end of the interaction region, at $t = T = L_{MOL}/v_z$ can be approximated by

$$x(T) \approx v_{os}T + \frac{m(v_{x0} - v_{os})}{\beta} + x_0 \quad (2.28)$$

$$v(T) \approx v_{os} + \frac{\kappa \cos(\theta)}{\beta} \left(\frac{m(v_{x0} - v_{os})}{\beta} + x_0 - x_{os} \right), \quad (2.29)$$

where x_{os} and v_{os} are given by Equations 2.25 and 2.26. It turns out that when the atomic trajectories are extrapolated after the interaction region, all trajectories will cross at the same position. In other words, the atom beam is focussed. The position of this focus can be calculated from the focus time T_{focus} at which the transverse position $x(T) - v(T)T_{focus}$ is independent of the initial position and velocity:

$$z_{focus} = v_z T_{focus} = \frac{\beta v_z}{\kappa \cos(\theta)} = \frac{\hbar k v_z}{\mu \nabla B \cos(\theta)}. \quad (2.30)$$

The transverse position of this focus is

$$x_{focus} = x_{os}. \quad (2.31)$$

Contrary to the MOC the atoms now do not follow the line where the magnetic field is zero. Instead it is now the angle of the lasers and the zeropoint of the magnetic field inside the interaction region that determine the position of the focus of the atom beam.

By placing the MOC at the focal point of the MOL, the effective capture radius of the compressor is increased. Because the magnetic field gradient in the MOL is much smaller than in the MOC, the capture diameter is much larger, approximately 40 mm. This way, the combination of MOL and MOC compresses almost all atoms that emerge from the Zeeman slower into a cold and narrow beam.

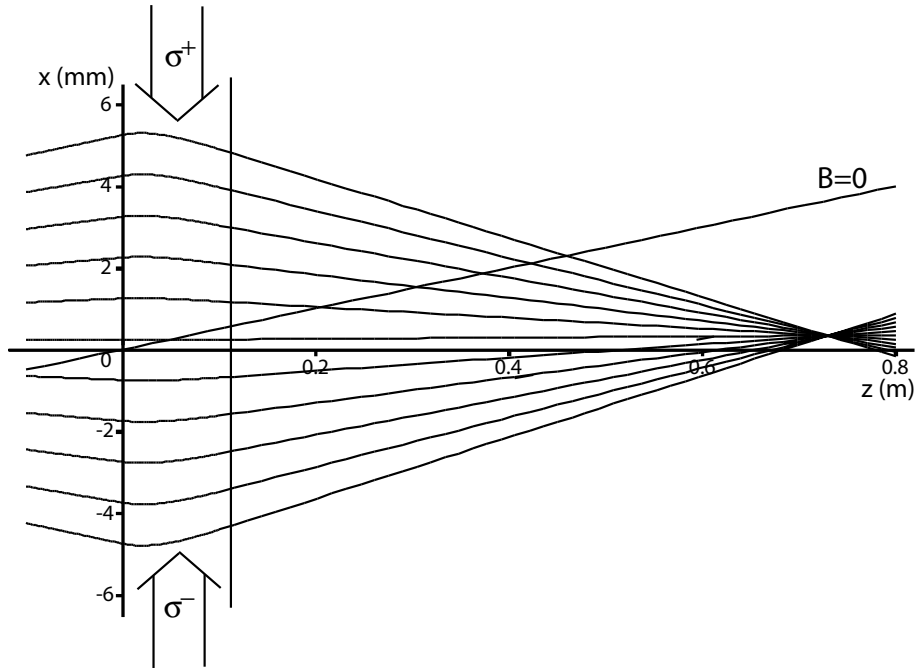


Figure 2.10: Atomic trajectories in the MOL as calculated by the damped oscillator model. Although the magnetic $B=0$ axis is under a (large) angle, the focal point remains on the optical axis.

Simulations [1] show that even in an ideal setup, the divergence of the atoms after the MOC is still $\sigma_{v_{\perp}} = 1.1$ m/s. This is still much larger than the recoil velocity. Therefore two extra collimating apertures of 60 and 25 μm separated by 2 m were added which select an atom beam with a transverse velocity spread of $v_{rec}/10 = 9$ mm/s.

2.4 Conclusion

The atom beam that is to be used in the interferometer has to meet stringent requirements. These arise from the demand that there has to be a macroscopic separation between the two arms and that the interference signal is not “washed out” by the velocity distribution. The current setup meets all of these requirements. Atoms that emerge from the supersonic source are first collimated by optical molasses. Then, the atoms longitudinal motion is slowed and cooled in the Zeeman slower, giving $v_z = 250$ m/s. After the slower the atoms are focussed by the Magneto-Optical Lens and then further compressed and cooled by the Magneto-Optical Compressor. Finally, after two collimating apertures, we are left with an atom beam that has a maximum transverse velocity of 0.1 photon recoil. Typical count rate at the end of the setup is approximately 50 atoms/s.

This is a very complex setup, with many parts that have to work together. Obviously, the chances of achieving this are minimal without good diagnostics on each section. These diagnostics will be described in the next chapter.

References

- [1] R.M.S. Knops, *Quantum optics with a cold helium beam*, Ph.D. thesis, Eindhoven University of Technology (1998).
- [2] A.E.A. Koolen, *Dissipative Atom Optics with Cold Metastable Helium Atoms*, Ph.D. thesis, Eindhoven University of Technology (2000).
- [3] A.E.A. Koolen, G.T. Jansen, K.E.F.M. Domen, H.C.W. Beijerinck, and K.A.H. van Leeuwen, *Phys. Rev. A* **65**, 041601 (2002).
- [4] D.J. Wineland and H. Dehmelt, *Bull. Am. Phys. Soc.* **20**, 637 (1975).
- [5] T.W. Hänsch and A.L. Schawlow, *Opt. Comm.* **13**, 68 (1975).
- [6] S. Chu, L. Hollberg, J.E. Bjorkholm, A. Cable, and A. Ashkin, *Phys. Rev. Lett.* **55**, 48 (1985).
- [7] Special issue on laser cooling and trapping of atoms in *J.Opt.Soc.Am B* **6** (1989).
- [8] H.J. Metcalf and P. van der Straten, *Laser cooling and trapping* (Springer, New York, 1999)
- [9] P.D. Lett, W.D. Phillips, S.L. Rolston, C.E. Tanner, R.N. Watts, and C.I. Westbrook, *J. Opt. Soc. Am. B* **6**, 2084 (1989).
- [10] E. Raab, M. Prentiss, A. Cable, S. Chu, and D.E. Pritchard, *Phys. Rev. Lett.* **59**, 2631 (1987).
- [11] R.M.S. Knops, A.E.A. Koolen, H.C.W. Beijerinck, and K.A.H. van Leeuwen, *Laser Physics* **9**, 286 (1999).
- [12] M.J. Verheijen, H.C.W. Beijerinck, L.H.A.M. van Moll, J. Driessen, and N.F. Verster, *J. Phys. E: Sci. Instrum.* **17**, 904 (1984)
- [13] H.C.W. Beijerinck and N.F. Verster, *Physica* **111C**, 327 (1981).
- [14] K. Ohno, T. Takami, K. Mitsuke and T. Ishida, *J. Chem. Phys.* **94**, 2675 (1991).
- [15] J. Nellessen, J.H. Müller, K. Sengstock, and W. Ertmer, *J. Opt. Soc. Am. B* **6**, 2149 (1989).
- [16] W. Rooijackers, W. Hoogervorst, W. Vassen, *Opt. Comm.* **123**, 321 (1996).
- [17] J.V. Prodan, W.D. Phillips, and H. Metcalf, *Phys. Rev. Lett.* **49**, 1149 (1982).
- [18] M.D. Hoogerland, J.P.J. Driessen, E.J.D. Vredenburg, H.J.L. Megens, M.P. Schuwer, H.C.W. Beijerinck, and K.A.H. van Leeuwen, *Appl. Phys. B* **62**, 323 (1996).
- [19] J. Nellessen, J. Werner, W. Ertmer, *Opt. Comm.* **78**, 300 (1990).

Chapter 3

Atomic Beam Diagnostics

3.1 Introduction

The total preparation stage of the atom beam consists of 6 sections: source, collimator, slower, lens, compressor and velocity selection (Chap 2). To get an atom beam that meets all criteria, all these sections have to work simultaneously. The optimal settings of each section, however, may depend strongly on the settings of all previous sections. Because of the large number of adjustable parameters in the setup, it is impossible to optimize the beam (or in fact to even get any beam running at all) by just measuring the beam intensity at the end of the setup. Additional diagnostics are essential to optimize and verify the operation of each stage separately.

3.2 Detectors

The detection efficiency of commercially available CCD cameras is very low at 1083 nm. This makes any diagnostics based on fluorescence very difficult, except possibly the detection of the final compressed beam directly after the compressor. So, instead, all diagnostics use the internal energy of the metastable atoms. This energy (20 eV) is much higher than the typical workfunction of a metal (5 eV, [1]) and therefore the impact of a metastable helium atom on a metal surface allows for the emission of an electron. The number of emitted electrons per second (current) is then a direct measure of the total atom flux on the surface. For helium in both the metastable $2s^3S_1$ and $1s^1S_0$ states, the electron emission efficiency on impact on stainless steel ranges between 0.5 and 0.95 [1, 2], depending on the quality of the surface. There are two severe disadvantages to this detection method. The measurement is destructive, i.e, an atom that hits the detector decays to the ground state and can no longer be used in the experiments. Furthermore, the detection requires a metal surface to be placed in the beam, limiting access for a longitudinal laser beam, as used in the Zeeman slower.

The preparation setup is schematically drawn in Fig. 3.1. At the end of the setup there is a 2 dimensional position sensitive detector (referred to as the 2D detector) [3] consisting of a triple z-stack of multi-channel plates (MCPs) and a resistive anode. The collimating apertures, however, block the view on the preparation section, so that only

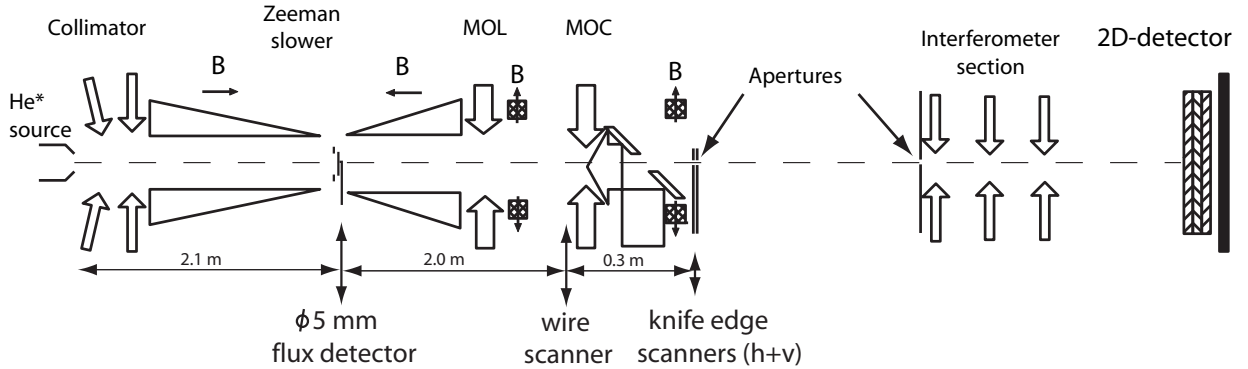


Figure 3.1: Schematic representation of the total setup including the permanent detectors.

little information about the operation of this section can be gathered from the signal on the 2D-detector. Its main use for diagnostics on the preparation stage will be the possibility to do time-of-flight measurements for fast atoms that have not been slowed down by the Zeeman Slower (Sec. 3.4.1).

Three other detectors are placed further upstream. They include a large area stainless steel flux detector (5 mm diameter), 0.1 mm diameter stainless steel crosswires mounted on a translator (wiresscanner) and a pair of perpendicularly movable conductive (ITO) plates with sharp edges (knife edge scanners). All these detectors are connected to electrometers that measure the total current of emitted electrons.

The knife-edge scanners are placed behind the mirror that couples the Zeeman slower laser beam into the vacuum. A small hole (1.2 mm diameter) in this mirror allows the passage of the final compressed atom beam with a relatively small distortion on the slower laser profile. When the first knife edge scanner is fully inserted, it is used as a total flux detector of the atoms that pass this hole in the slower mirror.

The two knife edge scanners have a 60 μm slit. The combination of the two knife scanners with a vertical and a horizontal slit, placed directly after each other forms the first collimating aperture.

3.2.1 Atom Beam Intensity Calibration

To directly determine the center-line atom beam intensity as it emerges from the source, a detector was built with a well defined detector area (see Fig. 3.2). The main component of the detector is a stainless steel disk, with a diameter of 5 mm. When placed 2 m behind the source, the atom flux on the large area still produces a current of a few 100 pA, which can readily be measured.

To make sure that an electron that is emitted by the impact of an atom does not return to the detector surface and hence does contribute to the current, a conducting ring was placed in front of the disk. When a positive bias voltage is applied to this ring, an accelerating electric field is formed which pulls the electrons away from the surface. This ring also prevents any electrons from the discharge source that are propagating along the atom beam from hitting the detector surface, thereby reducing the current. Experimentally it was found that the detector current increases with the bias voltage, leveling off at 60 V.

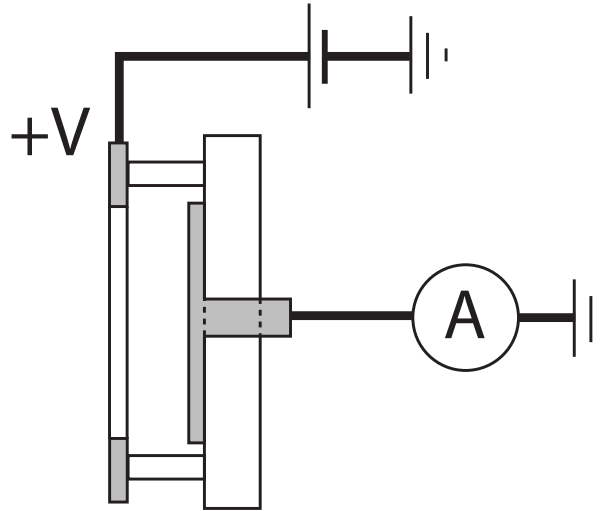


Figure 3.2: Schematic representation of the large area flux detector. A bias voltage can be applied to draw electrons away from the detector.

Apparently, at this voltage all electrons are removed from the beam and the surface. The influence of the bias voltage on the detector current is enormous; at 60 V the current is almost 20 times higher than without a bias voltage.

Maximum atom beam intensity of metastable atoms is reached when the total source gas flow of helium atoms is set to approximately $4 \times 10^{18} \text{ s}^{-1}$, giving an intensity of $3.8 \times 10^{14} \text{ s}^{-1} \text{ sr}^{-1}$ of metastable atoms on this detector. This corresponds to an excitation efficiency of 1×10^{-4} . Changing the discharge current between 4 and 10 mA does not have a significant effect on the measured beam flux.

Taking this intensity as a reference, we can calibrate the other two total flux detectors, i.e, the knife edge scanners and the 2D detector at the end of the setup. The knife edge scanners do not have a guard ring, so the only possibility to apply a bias field is to place a negative voltage on the detectors themselves. To avoid that this applied voltage induces a current larger than the atom beam signal, the detector circuit has to be well insulated from the rest of the setup ($> 10^{13} \Omega$). This is achieved by applying the bias voltage using batteries. At a bias voltage of 30 V we measured an intensity of $3 \times 10^{14} \text{ s}^{-1} \text{ sr}^{-1}$, which is consistent with the reference value.

The flux that reaches the final 2D detector is set by the size of the final collimating aperture ($\varnothing 25 \mu\text{m}$). The countrate on this detector without any laser cooling is typically 200/s. This intensity has to be corrected for the effective detection area of 60% that is formed by the open area of the channels of the MCP and for the loss in signal that is caused by the electronic threshold. If we make a very rough estimate of this threshold to 50% this measured countrate indicates an intensity of $5 \times 10^{13} \text{ s}^{-1} \text{ sr}^{-1}$. This is a factor 8 less than the reference value and the difference is much more than can be explained by the uncertainty on the electron emission efficiency.

The 2D detector counts the number of electronic pulses that are excited in the MCPs. Both electrons and metastable atoms can excite such a pulse and an electron would thus add

to the countrate instead of decreasing it. Two possible explanations for the low intensity are either that the intensity is indeed somehow reduced on the way from the knife edge scanner to the 2D detector or that the detection efficiency of the MCP is severely reduced.

At this point it is impossible to determine what the exact cause for the lower countrate is and we will have to keep in mind that there might be a relatively large margin of error on the flux on this detector. For all planned experiments, however, we do not need to know the absolute intensity of the atom beam, making this uncertainty acceptable.

3.3 Collimator

The effect of the collimator on the atom beam can be measured in two ways. One way is to measure the beam profile with a wirescanner. A metal wire is moved through the beam and at each position the current is measured that is excited by atom impact over the entire length of the wire. The beam profile is thus integrated over one dimension and information on the profile along the wire is lost. A true 2D image of the beam profile can not be made with this method, and only by assuming a specific profile it becomes possible to extract beam parameters.

We use crosswires that are rotated at a 45 degree angle with the translation axis and thus make two simultaneous scans in two perpendicular directions. The two scans always look very similar and therefor the results of only one wire is presented. Figure 3.3 shows two examples of a wirescan profile for laser detunings of -2Γ and -4Γ together with a reference scan where the collimator laser was turned off. It is clear from these scans that the collimator drastically reduces the beam divergence.

The profile at $\Delta_l = -2\Gamma$ has a FWHM of 9 mm. If we assume a spherically symmetric profile, this translates into a transverse velocity spread of $\sigma_{v\perp} = 1.2$ m/s, which is more than 4 times larger than the Doppler velocity. The theoretical limit on the velocity spread at this detuning is $1.5v_D = 0.42$ m/s [4] and we are still well above this. The most probable explanation for this relatively high divergence can be found in imperfections in the laser beam profile. The atom beam profile at $\Delta_l = -4\Gamma$ is clearly broader than the profile at -2Γ , as expected from the reduced cooling force.

The height of the peak I_{max} is 25 pA. In combination with the width and the assumption of a 2D Gaussian profile, we can calculate the total number of captured atoms:

$$\dot{N} = \sqrt{2\pi}\sigma_x \frac{I_{max}}{d_{wire}} = 1 \times 10^{10} \text{ s}^{-1} \quad (3.1)$$

and the maximum intensity

$$I_{max} = \frac{I_{max}}{\sqrt{2\pi}\sigma_x d_{wire}} = 2 \times 10^{14} \text{ m}^{-2}\text{s}^{-1}. \quad (3.2)$$

The second source of information on the operation of the collimator, and the most direct way to measure the center line beam intensity, is the total flux through the hole in the Zeeman mirror as measured on the knife-edge scanner. This way, we measure an intensity of $3 \times 10^{14} \text{ m}^{-2}\text{s}^{-1}$, in good agreement with the wirescan measurement. Typically, the collimator increases the flux on the knife-edge scanner by at least a factor of 100.

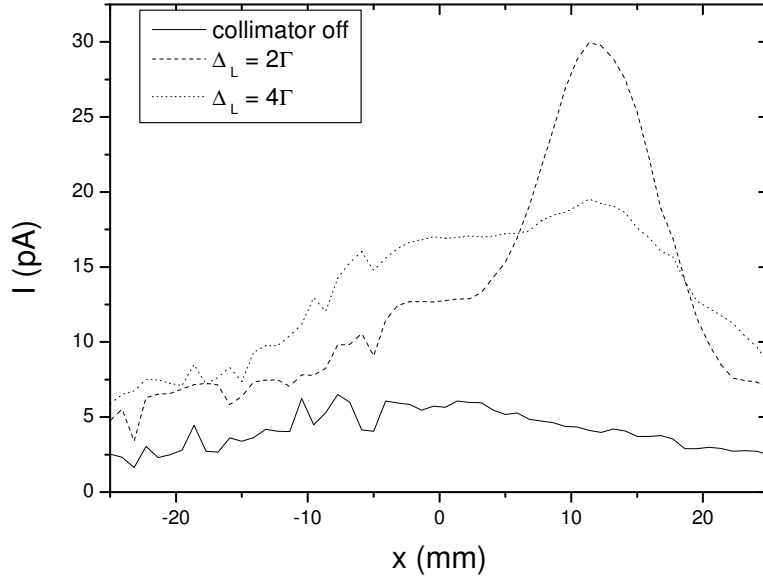


Figure 3.3: Wirescanner profiles for detuning of -2Γ and -4Γ of the collimator laser and a reference scan with the collimator laser turned off.

3.4 Time-of-Flight measurements

The large increase in beam intensity by the collimator can be used to effectively turn the beam on and off. By chopping the collimator laser, we can chop the atom beam with a contrast of 1/100. The response time is approximately equal to the interaction time of the atoms with the light field $\tau \approx L/v = 0.1$ ms. By measuring the intensity on a detector sufficiently far downstream as a function of the time after such a pulse, one can determine the velocity distribution of the atoms. This technique was used to optimize the setting of the source and to verify that in the Zeeman slower all atoms are slowed down to the target velocity.

3.4.1 Supersonic Source Velocity Distribution

For the measurement of the velocity distribution of the atoms that leave the source, we used the entire length of the setup to maximize the time resolution. The collimator laser was chopped with a mechanical chopper to give light pulses of 1.2 ms long at a repetition rate of 30 Hz. The detector electronics of the 2D detector at the end of the setup records the arrival time of each pulse it receives. By synchronizing this time with the chopper and discarding all position information of the atoms we obtained the time-of-flight distribution.

There are several parameters of the source that influence the velocity distribution. One of these is the total electrical power that is dissipated in the discharge. The current through the discharge is set to a fixed value of a few mA. The voltage over the discharge,

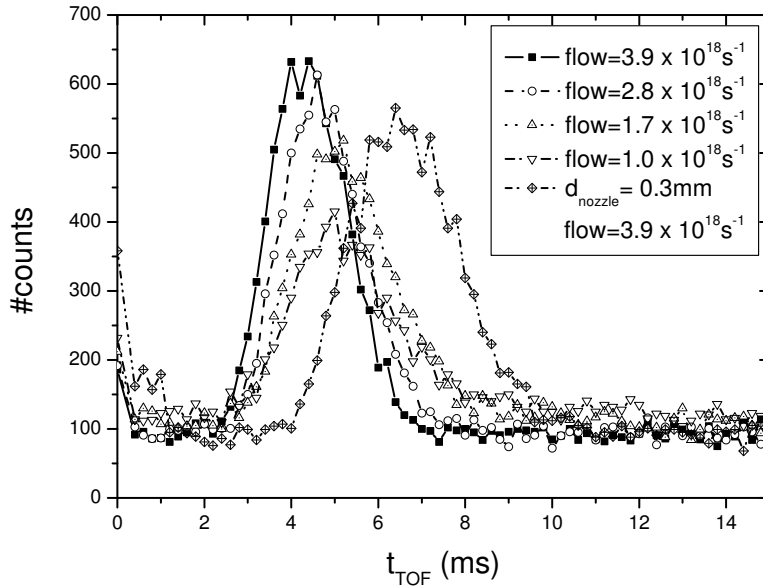


Figure 3.4: Some examples of the TOF signal on the 2D detector when the collimator laser is chopped. Shown are the signals for a nozzle with 0.11 mm diameter and increasing gas flow and one signal with a larger nozzle diameter, $d_{nozzle}=0.3$ mm.

however, depends not only on the current, but also on parameters such as the gas pressure, temperature and source geometry. Therefore, both the discharge current and voltage were measured. Under normal conditions, the discharge dissipates approximately 4 W.

In this setup we control the gas flow through the source by setting an inlet pressure upstream of a capillary. The source pressure can in principle be calculated from the gas flow, but this requires detailed knowledge of the source parameters such as the temperature. We tried to measure the source pressure directly with a pressure gauge downstream of the capillary, but under normal operating conditions this pressure is less than 1 mbar, making it difficult to get an accurate value.

The electrical power and the gas flow can readily be changed, but there are more parameters that influence the velocity distribution. Examples of these are the source temperature and the details of the nozzle geometry. To explore the effect of these parameters, we performed TOF measurements for various settings of the source parameters. A few examples of these TOF distributions are given in Fig. 3.4. Measurements were made with two different nozzle diameters (0.3 and 0.11 mm). It is clear from the longer travel time that the larger nozzle diameter results in a much lower average velocity. The graph also shows that the longitudinal velocity of the atoms depends on the gas flow. This effect, however is much smaller than the effect of the nozzle diameter.

To get a good measure of the velocity, the TOF graphs were fitted with the distribution that is associated with a supersonic flow (derived from Eq. 2.8). Results of the fitting

d_{nozzle} (mm)	cooling	\dot{N} (10^{18}s^{-1})	P (W)	u (m/s)	S	T_{source} (K)
0.11	LN_2	3.9	4.1	1390 ± 18	3.29 ± 0.15	212 ± 6
	LN_2	2.8	4.2	1350 ± 17	3.13 ± 0.13	203 ± 6
	LN_2	1.7	4.2	1184 ± 17	2.66 ± 0.11	164 ± 5
	LN_2	1.0	4.2	1174 ± 26	2.54 ± 0.15	164 ± 8
	none	3.8	4.2	1563 ± 42	3.00 ± 0.26	275 ± 16
0.3	LN_2	7.0	3.3	1101 ± 15	3.98 ± 0.23	128 ± 4
	LN_2	3.9	4.5	997 ± 13	3.15 ± 0.14	111 ± 3
	none	7.0	2.2	1525 ± 76	2.32 ± 0.29	287 ± 33

Table 3.1: Results of the fitting routine through the Time of Flight distribution for various settings of the source parameters. Given are the flow velocity u , the speedratio S and the effective source temperature that is calculated from these.

routine are given in Table 3.1. The table gives the flow velocity u and the speed ratio S that are the result of the fitting routine along with the effective source temperature that is calculated from these values using Equation 2.11.

First of all, we can check the validity of the fitting routine by looking at the calculated velocity when the source is not cooled. The table shows that for both nozzle diameters the effective source temperature that is derived from the TOF measurement is indeed close to room temperature. The associated velocity is 1550 m/s, which is much higher than the capture velocity of the Zeeman slower (≈ 1300 m/s), so cooling with liquid nitrogen is indeed essential. The velocity is lowered by cooling of the source, but there is a large variation, ranging from 1000 m/s to 1390 m/s. At the boiling point of Nitrogen (77 K), one would expect from Eq. 2.11 a flow velocity of approximately 900 m/s, however, even the lowest measured velocity is significantly higher than this. This indicates that there is some kind of process going on that either heats the gas or prevents an effective heat exchange with the liquid nitrogen.

The first candidate for such a mechanism is the discharge power dissipation. Inspection of the table, however, shows that for the small nozzle, the discharge power is constant, while there is still a large variation in temperature. For the large nozzle diameter, the effect is even reversed; a higher power gives a lower temperature. Considering the dissipated energy per atom also does not give an explanation, as with constant power the velocity increases with the number of atoms (flow rate).

The table clearly shows that the effective temperature strongly depends on the flow rate. For both nozzle diameters, the velocity decreases with decreasing atom flux. Possibly, the pressure inside the source is the critical parameter. This pressure can be estimated from the gasflow, the nozzle diameter and the source temperature (Equation 2.13). Although this estimate of the source pressure always gave a much higher value than was measured, it can still be used to check a relative effect. In Fig. 3.5 the final flow velocity is plotted versus this calculated source pressure. The graph clearly suggests that the source pressure is indeed the relevant parameter as the graph seems to be a smooth curve, even with the step in the nozzle diameter around $p_{source} = 5$ mbar.

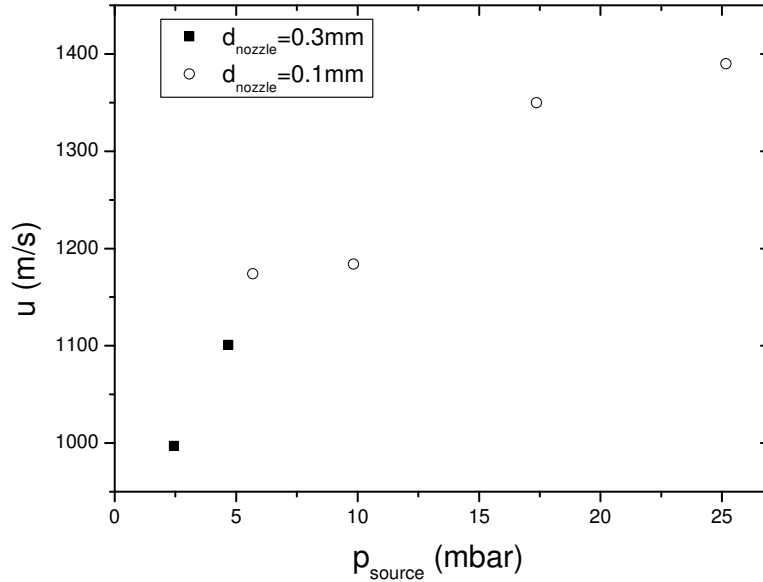


Figure 3.5: The flow velocity plotted versus the source pressure that is estimated from the gas flow and the nozzle diameter.

We tried to counter the heating by making a new nozzle plate. The new nozzle was more like a long channel (8 mm) than an aperture in a thin disk, which greatly increases the surface area around the nozzle and thus decreases the thermal resistance through the nozzle plate to the liquid nitrogen. This way the dissipated electrical power is more easily guided to the liquid nitrogen and the temperature of the gas should be lowered. All efforts, however, to get the discharge running with this new nozzle plate failed, leaving this hypothesis still unchecked.

In conclusion, although the physical processes are not completely understood, the time-of-flight measurements clearly show that the larger nozzle gives the lowest longitudinal velocity. Therefore, this nozzle is used in all further measurements. The TOF measurements also show that low source pressure leads to low effective temperature. Low pressure, however, means low flux. Thus the optimal pressure is a compromise between temperature and flux which has to be determined during operation of the total beam setup.

3.4.2 Zeeman Slower

Having verified that the source temperature is low enough, we can now continue with the Zeeman slower. The operation of the slower was analyzed using a similar TOF technique as was used on the source. The large divergence of the atom beam after the slower, however, quickly decreases the beam intensity to an undetectable level. To increase the signal, the knife edge scanner was used which is closer to the slower than the 2D detector. However, even on this detector the flux of slow atoms is still too low to measure. To solve

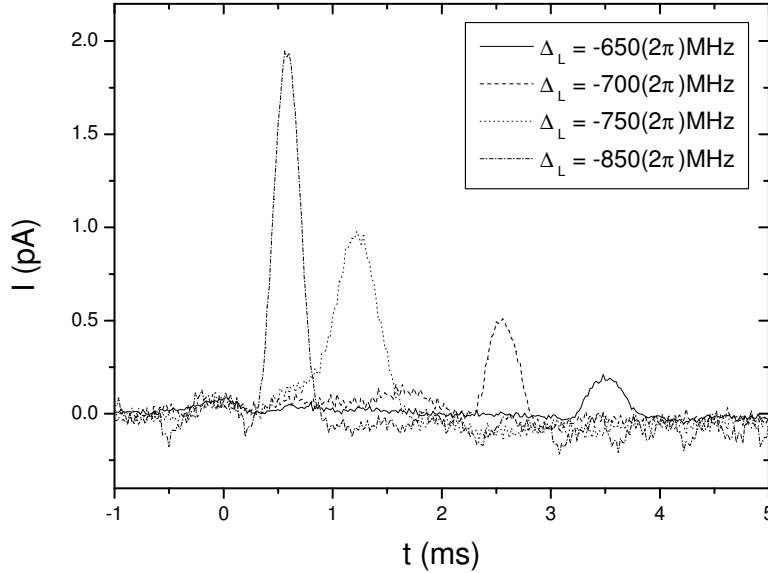


Figure 3.6: Some examples of the TOF signal on the knife edge scanner when the MOL is chopped. Images are given for $\Delta_L = -650, -700, -750,$ and $-850(2\pi)$ MHz.

this problem, we used the magneto-optical lens (MOL) to focus the slowed atoms on the detector. By chopping the MOL laser beam we obtained clear TOF signals.

An extra advantage of using the MOL is that it enables chopping the atom beam *after* the slower. The transit time through the slower is a complicated function of the initial velocity and this effect would blur the TOF signal if the beam is chopped before it enters the slower. By chopping after the slower, the TOF signal is independent of the details of the slowing process, enabling a direct measurement of the final velocity.

A few examples of the resulting time-of-flight signals are shown in Fig. 3.6. A complication when using the MOL is that the gain in detector signal by the MOL depends on the longitudinal velocity of the atoms (Eq. 2.30). It is impossible to determine the gain by the MOL and its velocity dependence a priori. Therefore, we used only the peak arrival time to get an estimate of the average velocity.

The first measurements showed that the atoms were not slowed all the way down to the final velocity (250 m/s), but instead ended up with a velocity of approximately 400 m/s. This suggested that the slowing process was stopped somewhere in the second half of the slower, possibly caused by a local glitch in the magnetic field gradient (Eq. 2.18). To decrease this glitch, the current through the second coil was slightly reduced (10%). The resulting change in capture and final velocity was compensated for with the current in the first coil and the laser detuning (Eq. 2.15). This small change proved to be sufficient, restoring the full slowing capability.

In Figure 3.7, the final velocity of the atoms that corresponds to the maximum of the

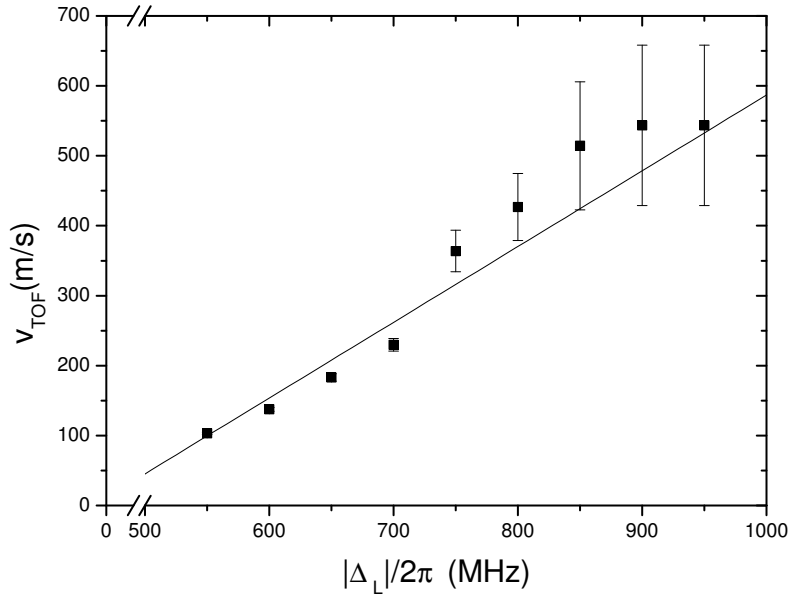


Figure 3.7: Final velocity (points) of the Zeeman slower versus the laser detuning. The line indicates the set velocity as determined by the laser detuning and the magnetic field strength at the end of the slower.

TOF plot is plotted versus the laser detuning. The current through the second coil was kept constant, but the current in the first coil was increased to compensate for the lowering of the capture velocity as the laser detuning was changed. The line in the plot indicates the expected velocity, obtained from the laser detuning and the magnetic field at the end of the slower. We can conclude that the Zeeman Slower now works as it should, with a tuning range on the final velocity of at least 500 m/s. Looking at the total TOF spectrum (Fig. 3.6), one can see that there is no sign of residual fast atoms, indicating that indeed almost all atoms are completely slowed down to the final velocity.

3.5 Atom Beam Compression

Now the Zeeman slower works correctly, it becomes possible to compress the slowed atom beam. The compressor consists of two stages: a lens (MOL) that focusses the atoms to the optical axis and a final compressor (MOC) which cools and compresses the atoms to a narrow and well collimated beam. Designing good diagnostics for both of these sections, but especially for the compressor, proved to be as essential as difficult.

The main problem is the necessity to have the slower laser beam running through the setup. This rules out most possibilities for placement of a detector upstream of the mirror that directs this slower laser in the vacuum. Behind this mirror, the information that can be gathered about the atom beam profile is limited because of the spatial filtering by the

small hole (1.2 mm diameter) in the mirror. In the end, a series of tests were performed which each gave a view on a different stage of the compression process and finally helped to fully compress the beam.

3.5.1 Focussing

The first stage of the compression process is the focussing of the atom beam by the MOL. The effect of this stage was measured in two different ways. The most important measurement is the total flux through the hole in the Zeeman mirror. The main purpose of the lens is to increase the number of atoms inside the capture radius of the MOC, which is situated at some distance before this mirror. An increase in flux on the knife edge scanner is a good indication that the center line beam intensity at the entrance of the MOC is also increased. Typically, the MOL (without the MOC) increases the flux through the mirror by a factor of 2.

A second diagnostic is provided by the wire scanner, located at the entrance of the MOC, which is thin enough not to disturb the slower laser beam. Two scans with and without the MOL are shown in Fig. 3.8. The scans clearly show an increase in the peak intensity by the MOL indicating that the atom beam is indeed focussed. The width (FWHM) of the peak is 7.8 mm. This is slightly larger than the expected capture diameter of the MOC (≈ 6 mm), but most of the atoms should still be compressed. If we estimate the total number of atoms from the height and the width of the profile, we find $\dot{N} = 9 \times 10^9/\text{s}$. This is very close to the total number of atoms that is captured by the collimator. All atoms that leave the Zeeman slower are thus focussed by the MOL.

3.5.2 Compression

The second stage of the compression process is performed by the MOC. Here, atoms inside a relatively small capture volume are compressed into a narrow and cold beam. Ideally, one would like to monitor the entire compression process with a camera, monitoring the 1083 nm fluorescence of the excited atoms. However, the low detection efficiency of commercially available cameras at the used laser wavelength make this virtually impossible. As mentioned, placing a detector inside the beam is also impossible, because that would block the slower laser. The only option that remains is to monitor the flux of the atoms through the hole in the Zeeman mirror. With well designed experiments, however, even this very limited view on the beam can provide a lot of information. A big problem is that the small atom beam has to be directed through a small hole. Since one can only see atoms that pass through this hole, a first signal has to be obtained by blind trial and error.

The main handle on the position of the atom beam is provided by the magnets. The atoms are cooled to the central axis where the magnetic field is zero (Sec. 2.3.5). The quadrupole magnetic field is formed by 4 individual permanent magnets that are mounted on a single stage that can both be translated and rotated in two dimensions. By moving the magnets, one can move the zero field axis and thereby the position of the atoms. The atom beam can then be aligned with the hole in the Zeeman mirror by maximizing the signal on the total flux detector. This increase in flux, however, does not mean that the atom beam is fully compressed. Focussing of the beam at a position close to the hole would

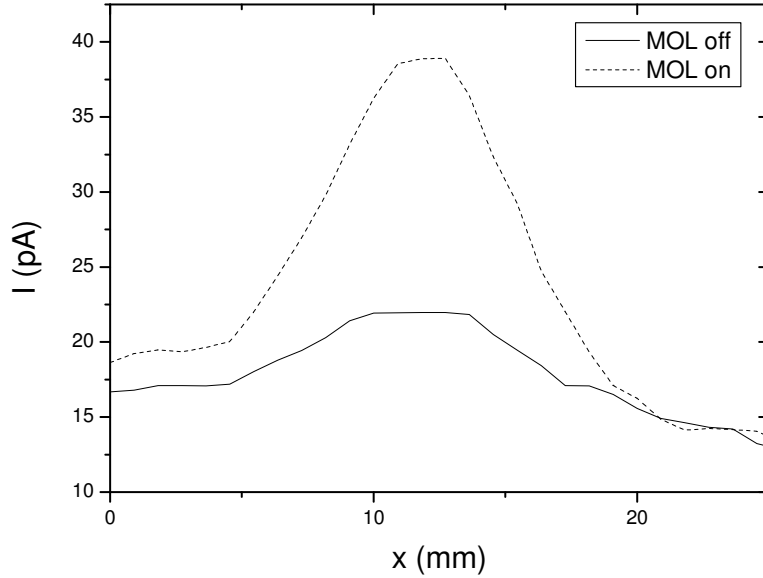


Figure 3.8: Focused beam profile just before the MOC, measured with the wire scanner.

also give an increase in flux, but would make the atom beam highly divergent.

To verify the completion of the compression process, the flux through the hole in the Zeeman mirror (3 cm behind the MOC) was measured as a function of the interaction length in the MOC. To achieve this, the laser beam entering the MOC was partially blocked with a different cut-off position for each measurement.

During the interaction with the laser, the transverse velocity and position of the atoms change (see Fig. 2.9). The atoms first acquire a velocity towards the axis of the setup and only when the atoms approach this axis, the transverse velocity is stopped. If the cooling process is stopped before the atom beam is fully compressed, the atom beam is effectively focussed at some point that depends on the interaction time. This is sketched in Figure 3.9. At first, as the interaction length is increased, the atoms get a larger velocity towards the axis of the magnetic fields. By extrapolation of the trajectories we see that the beam is focussed at a point that lies closer to the end of the MOC. After the inflection point of the full trajectory, the transverse velocity decreases again and the focus point gets further away from the MOC, until the beam is fully compressed and the focal point lies at infinity. The beam radius at the position of the mirror hole changes with the position of the focal point and thus on the interaction length. The flux through the hole in the mirror is maximal when the focus lies exactly on the mirror (trajectory 3 in Fig. 3.9) or when the beam is fully compressed and directed through this hole (trajectory 6).

The experimental results are given in Figure 3.10 where we indeed see the two characteristic points of increased flux. At the first maximum, around $L=0.01$ m, the atoms are focussed on the mirror. For longer interaction lengths the flux decreases because of the

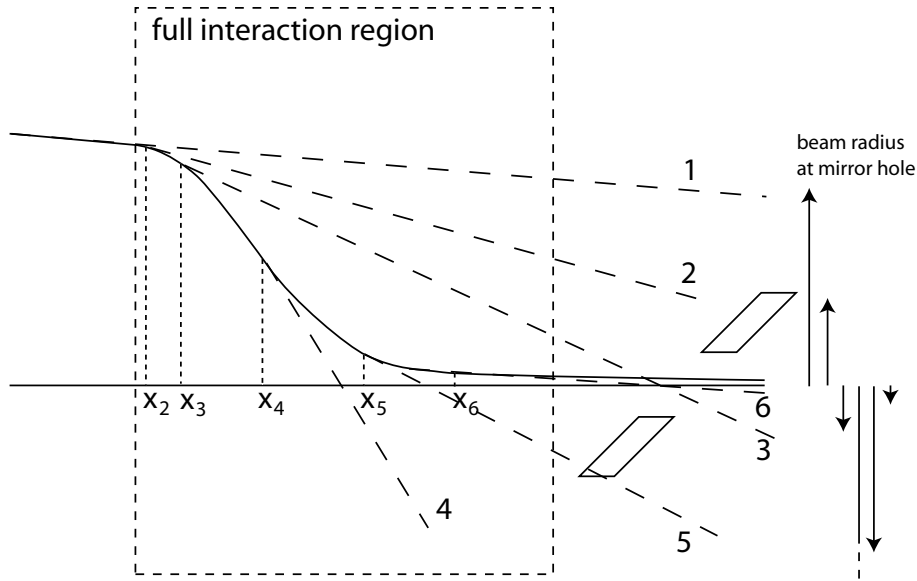


Figure 3.9: Effect of decreasing the interaction length in the MOC. The full line gives the trajectory when the MOC laser is not blocked. The dashed lines indicate the trajectories for increasing cut-off position of the laser x_i . The arrows at the right give the beam size at the mirror hole. At a specific interaction length (3), the atom beam is focussed at this hole, giving an increase in the transmitted atom flux.

focus length becomes shorter than the distance to the hole in the mirror. For $L > 0.04$ m the flux increases again, because the atoms have reached the inflection point of the trajectory. After $L = 0.11$ m the flux levels and the beam is fully compressed. We can thus recognize the entire compression process and the fact that the flux levels indicates that the interaction time is long enough for a full compression of the atom beam.

However, this measurement does not give all necessary information on the MOC. To check the final beam diameter and divergence, scans were made with the magnets and the knife edge scanners (Fig. 3.11). As mentioned, the position of the atom beam is set by the position of the magnets. By translating the magnets, one can move the atom beam over the hole in the mirror, using the hole as a probe for the local beam intensity. Assuming that this translation does not affect the quality of the compression process, this scan gives the beam profile at the position of the mirror hole. This profile looks very much like a square profile with a width of 1.2 mm, which is equal to the size of the hole in the mirror. We can thus conclude from this measurement that the diameter of the atom beam at the position of the mirror (3 cm behind the MOC) is significantly smaller than 1.2 mm.

The profile of the atom beam was also measured with the knife edge scanner. This scanner measures the total number of atoms impinging upon its surface. The signal as a function of the knife edge position thus represents the integral of the beam intensity and has to be differentiated to give the beam profile. We see in Fig. 3.11 that the scan gives a linearly increasing signal over the entire scanning range. The signal does not reach a maximum, which means that the beam diameter at the position of the knife edge scanner (14 cm behind the MOC) is larger than the scanning range. Combining this result with

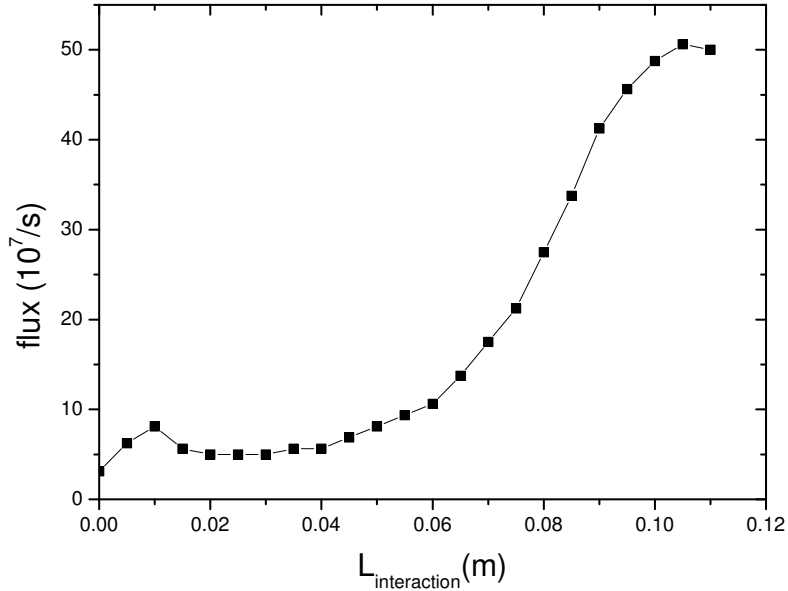


Figure 3.10: Atom flux through the hole in the Slower laser mirror as a function of the interaction length in the MOC.

the diameter at the mirror, we can estimate a beam divergence, giving $\sigma_\theta = 7$ mrad. This corresponds to a transverse velocity spread of 1.8 m/s which is equal to 6 times the Doppler velocity. In an ideal situation, one would expect to reach the Doppler temperature, a result that would be in agreement with 1D computer simulations [3]. The scans show, however, that the divergence of the atom beam is much larger. The most likely cause for this are imperfections in the light field. The light field is produced by circulating one single laser beam, with in total eight reflections on mirrors inside the vacuum. This design is efficient in laser power, but it leads to accumulated errors in the laser polarization and a possible dark spot in the center of the laser beam. A decrease of the beam divergence might thus be achieved by redesigning the optics.

3.5.3 Directional Control

Now that we have verified that we have a compressed atom beam, it has to be directed through the two collimating apertures. In order to do this, it is imperative to have a good control of the angle and position of the atom beam. Except for the total flux on the 2D detector, there is no information available to help with the alignment. Directing the beam through the two apertures then remains a blind trial and error process. Obviously, a good understanding of the effect of all parameters on the beams direction and position is necessary to have a chance for success. Measurements in the previous paragraph showed the control of the beam position with the position of the MOC magnets. To test the direction of the atom beam, a temporary extra detector was added at 0.7 m behind the

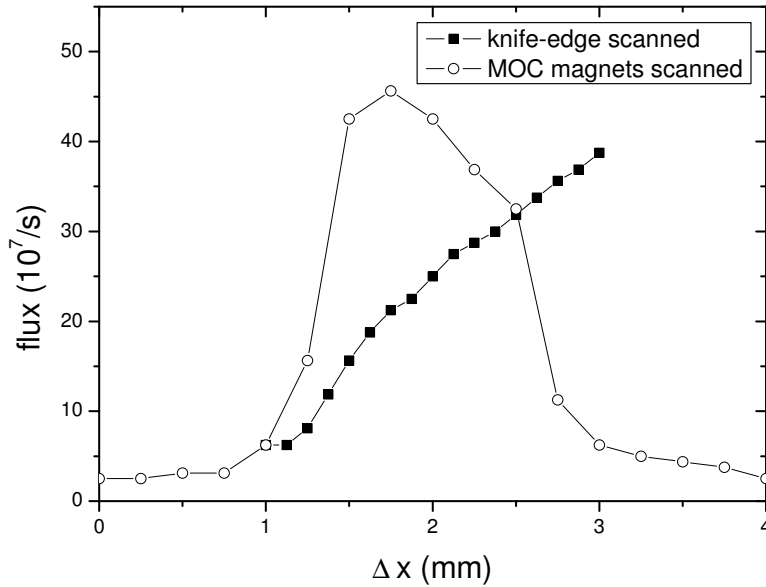


Figure 3.11: Two profiles of the atom beam after the compressor. One profile was obtained by moving the atom beam and using the hole in the Slower mirror (30 mm after MOC) as a probe. The other scan was made with the knife edge scanner (0.14 m behind MOC). This gives the integrated flux over the detector surface. The beam profile is the derivative of this curve.

Zeeman mirror.

The detector consisted of a multichannel plate (MCP) with a phosphor screen placed behind it (as in [5]). The impact of an atom induces a very localized current in the MCP and the impact of this current on the phosphor screen results in a flash. Integrated over many atoms, an image results that represents the atom beam profile. This image is recorded by a CCD camera and stored on a computer with a framegrabber card. An example of the resulting image is shown in Fig. 3.12 with a cross section. The intensity in these pictures is a measure of the atom beam intensity.

As a reference, another picture was taken with only the collimator turned on. The atom beam then is not slowed down and expanded by the Zeeman slower and there is only one peak with high intensity. The position of this peak is indicated by the cross in Graph 3.12 and the dashed line in the cross section. When the Zeeman slower is turned on, the height of this peak decreases, showing only the small fraction of atoms that are not captured by the Zeeman slower. The slow atoms remain invisible because of their high divergence. Only when the compressor is turned on, the cold atoms appear on the screen.

Graph 3.12 has two interesting features. First, there is the presence of the cold atoms, forming the broader spot in the image. The peak of the slow atoms is lower, but if the intensity is integrated over the entire 2D profile, we find that there are 10 times more slow

than fast atoms. The width of the spot of slow atoms is 4.9 mm, which corresponds to a divergence of the cold atoms of $\sigma_\theta = 4$ mrad. The transverse velocity spread is $\sigma_{v_\perp} = 1$ m/s which is consistent with the measurement by Koolen [6]. This method provides a more accurate measurement of the beam divergence than the method described in the previous section. Although this measurement gives a lower divergence than the estimated 7 mrad based on the knife edge measurement, the results confirm that the divergence is much larger than the Doppler velocity.

It turned out that the size of the spot is independent of the compressor laser detuning. Setting the laser closer to resonance decreases the damping time of the atomic transverse motion. The fact that the spot size is independent of the detuning thus again indicates that the interaction time of the atoms with the light is long enough to reach the cooling limit. The intensity does depend on the laser detuning, because the detuning also influences the capture radius and thus the number of atoms that are compressed.

The second interesting feature of the graph is the position of the peaks. Without the Zeeman Slower and the compressor, the atoms move in a straight line from the collimator through the hole in the Zeeman mirror to the detector. Because of the high velocity of these atoms, the position where they hit the detector is equal to the position of the main axis of the setup. When the compressor is turned on, the peaks of both the slow and the remaining fast atoms change in position. Despite the short interaction time, the effect of the MOC on the fast atoms is thus still large enough to deflect the fast atoms. The manner of deflection, however, is very different from that of the cold atoms. The interaction time is too short to direct the atoms along the magnetic field axis, and the deflection is probably caused by a slight off-axis focussing effect (like in the MOL).

The slow atoms are completely compressed and are thus expected to follow the magnetic field axis, as predicted by the simple theory described earlier (Sec. 2.3.5). When the angle between the magnetic field and the optical axis was changed, however, the position of the spot on the detector did not change. Instead, the largest effect on the atom beam direction is achieved by slightly changing the laser beam alignment. This surprising fact explains earlier problems in aligning the setup based on strategies derived from theory.

The final direction of the atom beam is thus set by the imperfections in the light field, which dominate over the guiding effect of the magnetic field axis. The steering possibilities with an intentional laser misalignment are limited, however, because at some point the imbalance becomes so large that the atom beam is no longer compressed. Therefore, the entire MOC vacuum chamber, including the fixed mirrors inside it, was slightly rotated relative to the rest of the setup by using bellows while compensating the change in the light field with optics outside the vacuum. Although this is a cumbersome procedure it allowed the position of the slow beam at the same position as the reference beam, thereby aligning it with the main beam axis.

3.6 Conclusions

In this chapter, a series of diagnostic tools were developed that helped in making the full beam line operational. The most crucial of these were the time-of-flight measurements and the imaging system with the temporary 2D detector. The TOF measurements showed that

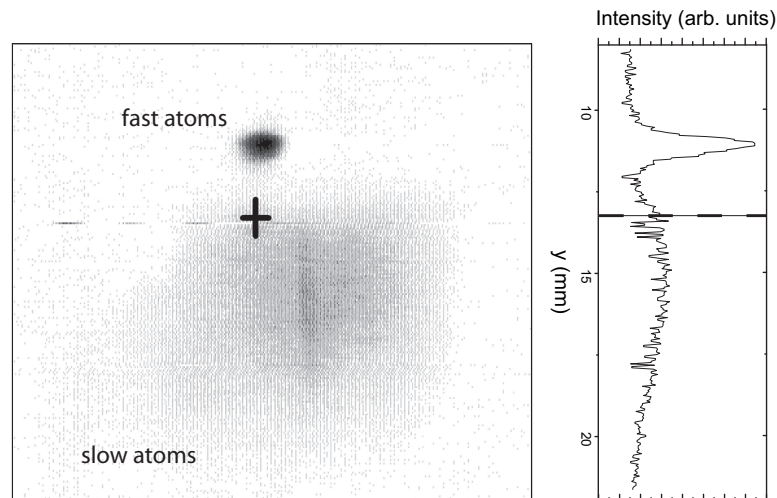


Figure 3.12: Image of the beam profile on the extra MCP detector with a cross section. The broader spot is formed by slowed atoms, the smaller and brighter peak consists of residual fast atoms. The reference position (the position where the fast atoms impinge the detector without the MOL/MOC) is given by a cross in the full image and by a dashed line in the cross section.

the nozzle geometry plays an essential role in the velocity distribution of the atoms that emerge from the source. Only by taking a relatively large nozzle diameter (0.3 mm), the effective source temperature could be sufficiently reduced to allow most atoms to be slowed to the target velocity by the Zeeman slower.

The TOF measurements also helped a great deal in making the Zeeman Slower fully operational. The TOF spectrum showed that the atoms were initially only partially slowed down. Choosing a slightly lower magnetic field gradient in the second half of the slower solved the problem, giving a beam of atoms that are now almost all slowed to 250 m/s.

The pictures taken with the temporary 2D detector gave crucial insight in parameters that affect the final direction of the compressed atom beam. The atoms do not follow the simple behavior that was sketched in Chapter 2.3.5. Imperfections in the light field apparently are too large and dominate the steering process. Knowing this, however, we were able to align the atom beam by rotating the entire MOC vacuum chamber.

Finally, after guiding the atoms through the two collimating apertures, we produced an atom beam with a flux of approximately 100 atoms per second that have a longitudinal velocity of 250 m/s and a FWHM divergence of 40 μ rad.

References

- [1] H. Hotop, *Atomic, molecular and optical physics: atoms and molecules* **29B**, p. 191, eds. F.B. Dunning and R.G. Hulet, (Academic Press, New York, 1996).

- [2] F.B. Dunning, R.D. Rundel and R.F. Stebbings, *Rev.Sci.Instrum.* **46**, 697 (1975).
- [3] R.M.S. Knops, *Quantum optics with a cold helium beam*, Ph.D. thesis, Eindhoven University of Technology (1998).
- [4] H.J. Metcalf and P. van der Straten, *Laser cooling and trapping* (Springer, New York, 1999).
- [5] W. Rooijakkers, W. Hoogervorst, W. Vassen, *Opt. Comm.* **123**, 321 (1996).
- [6] A.E.A. Koolen, *Dissipative Atom Optics with Cold Metastable Helium Atoms*, Ph.D. thesis, Eindhoven University of Technology (2000).

Chapter 4

Lasers

4.1 Introduction

The atom beam setup includes five sections that require laser light. All of these sections have different requirements on laser power and frequency. An estimate of the requirements on these parameters is summarized in Table 4.1. The table shows that the four laser cooling sections need only moderate laser power so that we can use laser diodes for these sections. For the atom interferometer we need considerably more power. Hence, we use a fiber amplifier (Keopsys, KPS-BT2-YFA-20-FA) to amplify the laser power of one of the diodes to a maximum of 2 W.

We use two different types of laser diode system. One is a Distributed Bragg Reflector laser diode (Spectra Diode Labs, SDL-6702H1, [1]) with an internal grating structure. The temperature of these diodes is controlled by a home-made controller that uses the NTC sensor and Peltier element that are integrated in the laser package. The diode current is supplied by a home-made current source. The other type of laser system is a complete commercial laser system (Toptica, DL-100), which is a laser diode with an extended external cavity formed by the optical feedback from a grating. In this system, the temperature of the entire external cavity is controlled. Because the MOL and the MOC were expected to use the same laser detuning, the Toptica laser provides the power for both of these sections. All other sections are supplied by separate SDL diodes.

In the experiments we always use the $2s^3S_1 \rightarrow 2p^3P_2$ transition of metastable Helium which has a wavelength of 1083.034 nm and a linewidth of 1.6 MHz. The required detunings relative to this transition are indicated in Table 4.1 and can easily be obtained by tuning the laser diode temperature. For the stability of the laser frequency, the laser cooling sections require that the laser frequency does not fluctuate by more than the transition linewidth. If we compare this with the free running linewidth of the SDL diodes (3 MHz), it becomes clear that this requirement is not easy to meet. The lasers are therefore carefully isolated from all sources of noise (see Section 4.2). Additionally, all lasers are actively stabilized to obtain the required stability. The collimator and the compressor lasers are both directly locked to the atomic transition frequency in a reference gas cell (see Section 4.4). The other two lasers (slower and interferometer) are operated at a detuning that is too large to reach with a gas cell. Therefore, these lasers are referenced to the other two by using a frequency-offset phase locking technique (Section 4.5).

section	power(mW)	detuning(MHz)	stability(MHz)	laser system
collimator	20	-3	<1	SDL
slower	20	-630	<1	SDL
lens	20	-3	<1	}Toptica
compressor	10	-3	<1	
interferometer	1000	± 1000	$\ll 10^3$	SDL + amplifier

Table 4.1: Requirements on laser power, frequency and frequency stability for the five different sections of the setup

4.2 Passive Isolation

As Table 4.1 indicates, there is only a small margin of error for the laser frequency. The laser frequency is very sensitive to noise and careful isolation, both mechanical and electronic, is required before the noise is reduced to a level that is low enough.

The frequency stability of the laser was tested with a low finesse etalon. The length of the etalon was tuned close to resonance with the laser frequency. Using the known transmission curve of the etalon, fluctuations in the transmitted laser power are then translated into fluctuations of the laser frequency. Using this diagnostic tool, it was found that there are two main sources of noise that disturb the laser frequency stability.

The first source is optical feedback [2] from other optical components in the setup. Most of this optical feedback could be eliminated by using two optical isolators per laser in series (in total 60 dB isolation). However, there is some feedback from the isolators itself. This feedback is already strong enough to influence the laser frequency. A change in distance between the laser and the isolator then shifts the laser frequency. Therefore, both the isolator and the laser have to be firmly attached to the optical table and as close to the table surface as possible (± 4 cm) to remove any relative vibrations.

The second source of noise is electrical. This was eliminated by a careful layout of the electronics and good grounding [3]. The optics and the electronics are placed such that the length of all cables is as short as possible and the area of any ground loop is minimized. To make sure that induced currents in the remaining loops have no effect on the electrical signals (and the laser frequency) all ground connections to cases and mantles of coaxial cables are carefully short-circuited to a resistance below 0.1Ω .

4.3 Control Theory

Not all changes in laser frequency can be eliminated by passive isolation. Especially low frequency noise and drift are very difficult to remove by passive means. Therefore, control loops were added that actively lock the laser frequency to a reference value. In order to get an optimal design of the control systems, we need a basic understanding of the dynamics of a control loop. The following is, therefore, a short introduction to the basics of control theory [4].

The behavior of a linear time invariant control loop is most easily described in Laplace space where the dynamical output of a system is simply the product of the input with the

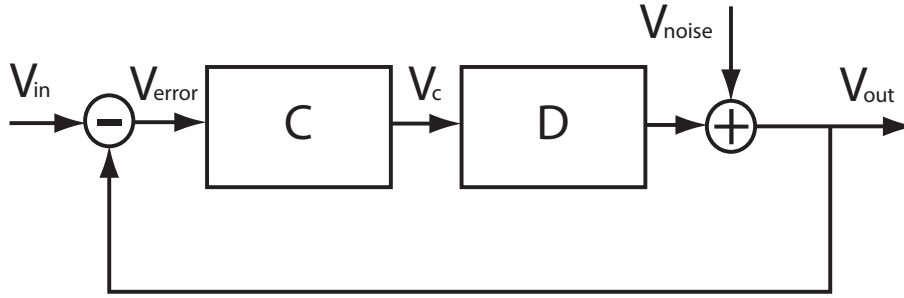


Figure 4.1: Schematic representation of a feedback loop with a device D that is to be stabilized with the controller C

transfer function $\tilde{G}(s)$:

$$\tilde{V}_{out}(s) = \tilde{G}(s)\tilde{V}_{in}(s). \quad (4.1)$$

The impulse response in time (the output after a short pulse is applied to the input) is given by the inverse Laplace transform of $\tilde{G}(s)$. Then the output as a function of time for an arbitrary input is the convolution of this input with the impulse response. A simple example of a first order transfer function and the associated impulse response is:

$$\tilde{G}(s) = \frac{1}{s - s_0} \Leftrightarrow G(t) = \mathcal{L}^{-1}(\tilde{G}(s)) = e^{s_0 t}, \quad (4.2)$$

which corresponds to an RC filter if $s_0 = -1/RC$.

This result can be generalized to higher order polynomials in the denominator with the result that all poles of the transfer function (zeros of the denominator of $\tilde{G}(s)$) give an exponential factor in the time response. Clearly, if any of these poles have a positive real part, the output grows exponentially in time and the system is unstable. Thus, for a well designed system the real parts of all poles of the transfer function have to be negative.

In a feedback loop, one continuously monitors the output and compares this with a reference. Based on the difference between these two, the input is changed such that the output gets to the desired value. Such a feedback loop is drawn schematically in Fig. 4.1, where D is the device whose output has to be stabilized to the value V_{in} and C is a controller that reshapes and amplifies the error signal for good stability and performance. It can readily be shown that the output is given by

$$\tilde{V}_{out}(s) = \frac{\tilde{V}_{noise}(s)}{1 + \tilde{G}_D(s)\tilde{G}_C(s)} + \frac{\tilde{G}_D(s)\tilde{G}_C(s)\tilde{V}_{in}(s)}{1 + \tilde{G}_D(s)\tilde{G}_C(s)}. \quad (4.3)$$

Obviously, one wants to make the gain of the controller $\tilde{G}_C(s)$ as large as possible, because then the noise is maximally suppressed and the output exactly follows the input. For stability, however, the real parts of the poles (the zeros of $1 + \tilde{G}_D\tilde{G}_C$) still have to be negative. Noise that originates in the detector (measurement noise) has a much larger effect on the output if the gain of the controller is large. Therefore, if this is the predominant source of noise a low gain controller could be more beneficial.

The Nyquist criterium states that a feedback loop is stable if the open loop gain $\tilde{G}_D(i\omega)\tilde{G}_C(i\omega)$ as a function of the real frequency ω plotted in the complex plane does

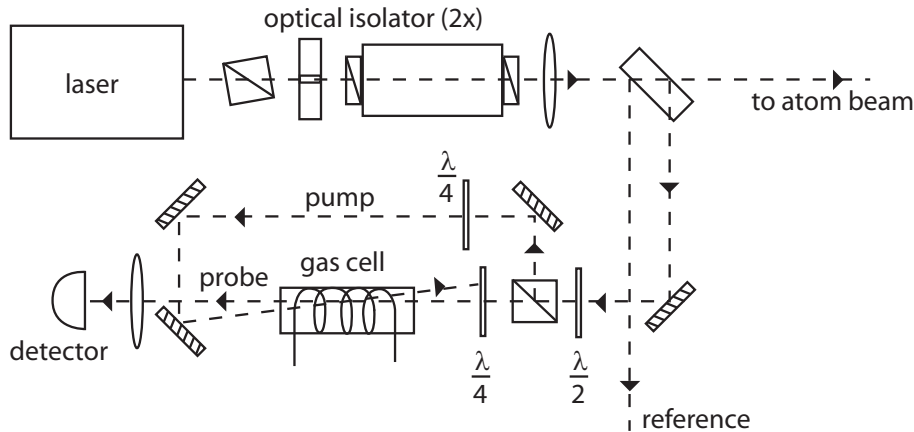


Figure 4.2: Schematic representation of the optical part of the laser stabilization setup that uses saturated absorption spectroscopy

not encircle -1 in a clockwise direction. Translated into practical design criteria this means that when for increasing frequency the total phase delay becomes 180 degrees, the total open loop gain $|\tilde{G}_C \tilde{G}_D|$ has to be less than unity. In a fast system the total gain can be large over a long frequency range and noise suppression can be strong over a large bandwidth.

4.4 Frequency Lock on Atomic Transition

As mentioned, there are two lasers that have to be locked close to resonance. The SDL laser diode can be tuned with the diode current and the temperature. However, because the temperature response is slow, the temperature is only used for the approximate setting of the laser frequency. The diode current is used in the frequency lock. The Toptica laser has an extended cavity that is formed with optical feedback from a grating. By changing the length of this external cavity with a piezo element we have an additional way to tune the laser frequency. The response of the piezo element is slower (up to 1 kHz modulation frequency) than the response to the diode current, but it has a larger tuning range. Therefore we use the piezo to compensate the slow drift and feedback on the diode current to compensate fast fluctuations in the laser frequency.

The reference for both of these lasers is provided by gas cells [5] in which the atoms are partially excited to the metastable state by an RF discharge. We probe the required transition with Doppler-free saturated absorption spectroscopy [6]. Both the pump and the probe beam are σ^+ polarized so that the atoms are pumped to the $|m_g = +1\rangle$ state and optical transitions are limited to a two level system. At resonance the probe beam experiences diminished absorption because the excited state of the atoms is saturated by the pump beam. The width of this absorption dip (Lamb dip) is approximately 10 MHz and the control loop fixes the laser frequency to the center of this dip. The exact frequency of this dip can be shifted via the Zeeman shift in a DC magnetic field up to approximately 100 MHz. A small angle between the probe and the pump beam is introduced to avoid optical feedback to the laser diode. This gives a slight offset to the resonance frequency which is compensated for with the magnetic field.

To transform the saturated absorption peak into a dispersive error signal we use two methods. In one setup (collimator, SDL diode) we modulate the magnetic field in the reference gas cell at a frequency of 10 kHz and demodulate the detector signal with a lock-in amplifier. The resulting error signal is integrated and added to the diode current. The bandwidth of the control loop is limited by the low modulation frequency and only fluctuations with a frequency up to 100 Hz are effectively removed. We measured the frequency stability with an etalon and found $\Delta f_{RMS}=0.4$ MHz over a measuring time of 0.5 s, well within the tolerance.

The other laser (MOL/MOC, Toptica) uses a Pound-Drever-Hall modulation scheme [7]. Here, the laser frequency is modulated instead of the reference cell, by modulating the diode current at a frequency of 20 MHz. The error signal that is formed by demodulation of the detector signal is fed back to the laser system in two ways. First, the error signal is integrated and added to the piezo voltage to correct the length of the extended cavity. The bandwidth of this loop is approximately 1 kHz. Faster fluctuations in the laser frequency are compensated for by a parallel proportional feedback loop acting on the diode current. This loop compensates fluctuations with a frequency up to 100 kHz. In the end this laser has a stability of 0.5 MHz.

Even though the feedback loop on this laser is much faster, the final frequency stability is approximately the same as the stability of the collimator laser. The reason for this is that the spectrum of the (remaining) frequency noise has a bandwidth that is much larger than 100 kHz. The largest part of this spectrum is not affected by any of the feedback loops. Both setups adequately remove the long term drift and slow fluctuations, but the remaining frequency fluctuations (laser linewidth) remain the same. The stability is however good enough for the experiments.

4.5 Frequency Offset Lock

The laser for the Zeeman slower and the atom interferometer operate at a large detuning that can not be reached with the reference gas cell. These two lasers are therefore locked to the collimator and the MOL/MOC laser with a frequency offset lock based on a phase locking technique [8,9]. The beat frequency with a stabilized laser is measured and this beat frequency is locked to a stable reference oscillator by the phase locked loop.

4.5.1 Phase Locked Loops

Principle of Operation

Although the final setup uses two references (the stabilized laser and the reference generator), we will first explain the principles of a phase locked loop (PLL) with only one reference, as in Figure 4.3. In this PLL, the oscillator is locked to the zero crossing of the output of the mixer. This mixer produces the product of two oscillating input signals:

$$V_{product} = \sin(\phi_1(t)) \sin(\phi_2(t)) \propto \sin(\phi_1(t) - \phi_2(t)) + \sin(\phi_1(t) + \phi_2(t)). \quad (4.4)$$

After filtering any DC and the high frequency component (sum of the phases) this multiplication results in a signal that oscillates with the frequency difference. Because the loop

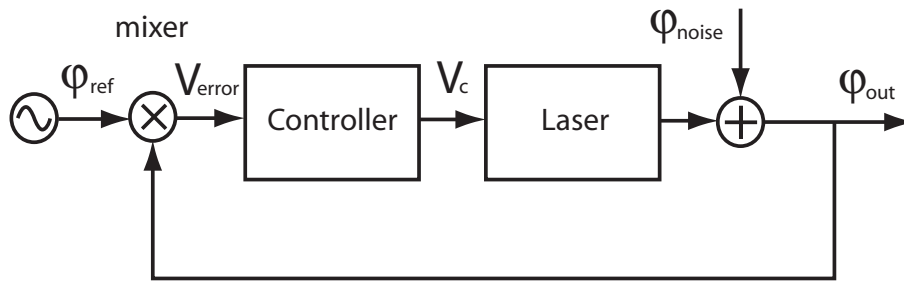


Figure 4.3: Schematic diagram of a phase locked loop

locks to a zero crossing of this oscillation, the phase (and thereby the frequency) of the oscillator is locked to the phase of the reference.

Capture

The difference between a phase locked loop and a regular stabilization loop is that the error signal does not increase linearly with the phase difference, but oscillates. With large frequency differences or when viewed over long a time scale the sign of the error signal thus alternates as well. This is the case if the control loop has just been turned on and the frequency of the laser is not yet equal to the reference. In that case the frequency of the oscillator will at some times be shifted in the wrong direction, away from the reference frequency. If the loop is designed well, however, the oscillator can still be locked. It is very difficult to describe the behavior of the loop analytically, but qualitatively the following happens in a first order PLL.

When the error signal is “on the right slope” the loop brings the frequencies closer together. On the other slope, the frequencies will get further apart. However, because the phase difference grows slower when the frequency difference is small, the loop will stay “on the right slope” longer. Averaged over a full oscillation, there remains an effective push on the laser frequency towards the reference. Then after a number of cycles, the frequencies have become the same and the error signal no longer oscillates.

The frequency of the error signal is equal to the frequency difference between the laser and the reference. If this frequency is larger than the bandwidth of the control loop, the loop does not react to the error signal anymore and the laser frequency can not be locked. The maximum frequency difference that can be “captured” by the loop is thus approximately equal to the bandwidth of the loop. It is very difficult to manually set the laser frequency with an accuracy better than 1 MHz and thus the bandwidth of the control loop has to be at least as high.

Stability

To test the stability of the loop, we need to know the total open loop gain. As mentioned, the phase detector (mixer) is a highly non-linear device. However, when the frequency is locked the phase excursions will be small and the output of the mixer (V_{error}) can be approximated as linear with the phase difference. The response of the laser to an input

signal is a change in frequency. The laser phase is the laser frequency integrated over time, which adds a factor $1/s$: $\tilde{\phi}_{laser}(s) = \tilde{\omega}_{laser}(s)/s$. (Note: the dimension of $\tilde{\phi}_{laser}(s)$ is s and $\tilde{\omega}_{laser}(s)$ is dimensionless.) In an ideal loop where we use a simple amplifier as the controller and all components are fast enough, the total open-loop gain is then a perfect integrator, a first order PLL

$$\tilde{G}_{tot}(s) = \frac{1}{s\tau_{loop}}, \quad (4.5)$$

where the time constant τ_{loop} is set by the total amplification by the mixer, the controller and the laser.

Suppose that without feedback the laser phase fluctuates in time with a spectrum $\tilde{\phi}_{laser}(s)$. This noise is reduced by the feedback and with a closed loop the spectrum of the residual phase fluctuations is

$$\tilde{\phi}_{closedloop}(s) = \frac{\tilde{\phi}_{laser}(s)}{1 + \tilde{G}_{tot}(s)} = \frac{\tilde{\omega}_{laser}(s)}{s(1 + \tilde{G}_{tot}(s))} = \frac{\tilde{\omega}_{laser}(s)\tau_{loop}}{1 + s\tau_{loop}}. \quad (4.6)$$

For the loop to stay in lock, the residual phase fluctuations must be smaller than π . The RMS value of the remaining phase fluctuations is given by:

$$\sigma_{\phi}^2 = \int S_{\omega}(f) \left| \frac{\tau_{loop}}{1 + if\tau_{loop}} \right|^2 df, \quad (4.7)$$

where $S_{\omega}(f)$ is the free running power spectral density of the laser frequency fluctuations. In the case that this power spectrum is independent of f (white noise, $S_{\omega}(f) = S_{\omega,0}$), the probability of measuring a specific laser frequency is given by a Lorentzian with FWHM $\Delta f_{FWHM} = \pi S_{\omega,0}$ [10]. This probability density is easily measured with e.g, an etalon and has a width of approximately 3 MHz for the lasers that we use. The requirements on the residual phase stability then translate into

$$\sigma_{\phi}^2 = \frac{\tau_{loop}^2 \Delta f_{FWHM}}{\pi} \int \frac{1}{1 + (f\tau_{loop})^2} df = \tau_{loop} \Delta f_{FWHM}. \quad (4.8)$$

For the loop to stay in lock, the bandwidth of the control loop ($1/\tau_{loop}$) thus has to be larger than the free running frequency fluctuations of the laser Δf_{FWHM} . Of course, the regular stability (Nyquist, Sec. 4.3) criterium still applies. Therefore, to make the phase locked loop work, all components of the loop including the frequency response of the laser have to be much faster than the free running laser frequency fluctuations.

There are two ways to alleviate the strict demands on bandwidth. One is to use a more complicated controller (PID controller for example) that artificially increases the control bandwidth of the laser and thereby the effective feedback bandwidth. The other possibility is to use a frequency divider which has three main advantages. First, the working frequency is reduced, which greatly simplifies the electronics design. Second, it has a digital output and thus amplifies the signals to a fixed amplitude, so that any unwanted filtering effects (by cables and amplifiers for example) are compensated. Third, the error signal fluctuates slower so that the laser can more easily follow and lock. This way the capture range of the loop is increased and the required phase lock is more easily obtained. If at the same time the total loop gain is kept constant, for example by increasing the amplification by the controller, the stability of the laser frequency is not affected.

4.5.2 Implementation

The actual stabilization setup is slightly more complicated than the idealized picture of the previous section. Instead of locking the laser directly to one reference oscillator, we first take the beat signal of the laser with a stabilized reference laser. This beat frequency is then locked by the PLL to a reference generator. This way the laser frequency is locked to the laser frequency of the reference laser plus (or minus) the frequency of the generator.

Both lasers use the setup that is given in Fig. 4.4. The slowest component in the loop is the mixer (MiniCircuits ZRPD-1 phase detector) with a maximum output frequency of 50 MHz and a maximum input frequency of 100 MHz. The laser for the Zeeman slower has a detuning of approximately 700 MHz. To bring the beat frequency within the range of the mixer, it was scaled down by a factor of 16 (Motorola MC12026A prescaler). The atom interferometer laser needs a detuning of 1 GHz and higher so in this case the beat frequency is divided by 64 (NEC UPB1505GR prescaler).

The maximum output voltage of the mixer is insufficient to compensate the drift of the laser frequency during the day. Thus, to increase the feedback range an extra PI controller was added behind the mixer. To stay well below the maximum frequency of the mixer and to avoid any influence of sum frequency signals the bandwidth of the control loop (frequency with unity gain of open loop) was set to 2 MHz by the appropriate choice of the proportional gain of the controller. For stability of the feedback loop, the time constant of the PI-controller has to be longer than this. By setting the time constant of the PI controller to 10^{-5} s, we obtain extra strong feedback on lower frequencies and are able to track the drift for a full day.

We use a frequency counter (Votcraft 7023) to measure the frequency stability of the beat signal. If we use a stable signal generator (Adret 7100A) the beat frequency does not change outside the accuracy of the counter (10 kHz at 10 ms integration time, or 10 Hz over 10 s). Using a somewhat less stable reference oscillator (Peaktech 1450SG) the beat node still has a stability of 2 kHz, equal to the frequency stability of the signal generator. In other words, the phase locked loop works very well and the stability of the beat frequency is in practice only limited by the stability of the reference oscillators. The stability of the reference lasers, however, is much worse (≈ 0.5 MHz) than the stability of the beat frequency. Thus the stability of the laser frequency is completely determined by the stability of these reference lasers.

4.6 Conclusions

We have built four laser setups that meet the requirements on laser frequency, frequency stability and power. Two lasers are locked to an atomic transition using saturated absorption spectroscopy. We obtained a frequency stability of approximately 0.5 MHz, well below the transition linewidth. The other two lasers are phase locked to these lasers with a frequency offset. The stability of the difference frequency was much better than the stability of the reference lasers. We can thus conclude that the phase locked loops work very well and the stability of the actual laser frequency is equal to that of the reference lasers. Three diodes provide enough power for the laser cooling sections. The power for

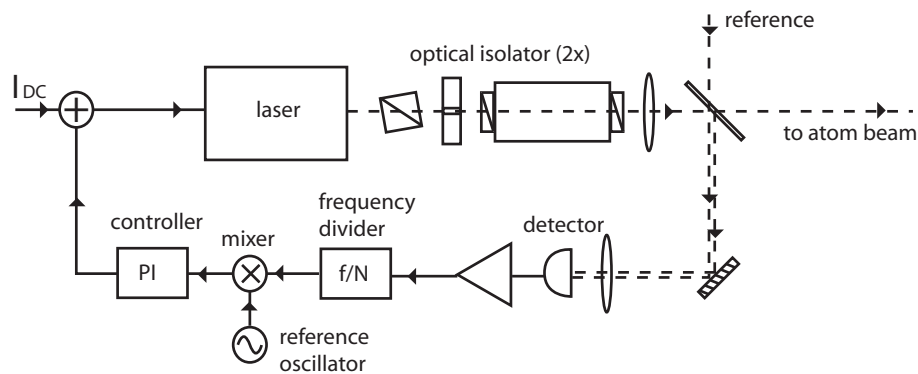


Figure 4.4: Schematic diagram of the phase locked loop setup

the atom interferometer is generated by power amplification of one of the lasers by a fiber amplifier.

References

- [1] J.S. Major and D.F. Welch, *Electr. Lett.* **29**, 2121 (1993)
- [2] R.W. Ktach and A.R. Chraplyvy, *IEEE J. Lightwave Techn.* **4**, 1655 (1986)
- [3] J.J. Goedbloed, *Electromagnetic Compatibility* (Prentice Hall, London, 1992)
- [4] see for example B. Friedland, *Control System Design, an introduction to state-space methods* (McGraw-Hill, London, 1986)
- [5] We gratefully acknowledge the group of Prof.dr. W.Hogervorst at the Vrije Universiteit of Amsterdam for filling the gas cells.
- [6] W. Demtröder, *Laser Spectroscopy: basic concepts and instrumentation*, second enlarged edition (Springer, 1996)
- [7] R.W.P. Drever, J.L. Hall, F.V. Kowalski, J. Hough, G.M. Ford, A.J. Munley, and H. Ward, *Appl. Phys. B* **31**, 97 (1983)
- [8] K. Kuboki and M. Ohtsu. *IEEE J. Quant. Electron.* **23**, 388 (1987)
- [9] F.M. Gardner, *Phaselock Techniques* (Wiley, New York, 1966)
- [10] Fritz Riehle, *Frequency Standards*, (Wiley, 2004)

Chapter 5

Atomic Bragg Scattering

5.1 Introduction

Bragg scattering was first observed in the diffraction pattern of an X-ray beam on a cleaved crystal surface. The beam is specularly reflected by the surface only when it hits the surface under certain specific angles θ_B . The value of these angles can easily be calculated by considering reflection of the X-rays by several stacked lattice planes and the requirement of constructive interference between all of these reflected beams. We find the Bragg condition which sets the angles θ_B at which specular reflection can be seen:

$$2d \sin(\theta_B) = N \lambda_{beam}. \quad (5.1)$$

Here d is the distance between the crystal planes, λ_{beam} is the wavelength of the diffracted (X-ray) beam and N is an arbitrary integer.

This kind of diffraction can also occur for other kinds of waves and even for massive particles. An example of the latter is the diffraction of neutrons on a crystal [1]. In this chapter we will study the diffraction of a cold atom beam on a near-resonant standing light wave (Fig. 5.1). If the laser is tuned off-resonant and spontaneous emission can be neglected, the standing light wave acts as a periodic potential [2] and takes the role of the lattice planes with separation $d = \lambda_{laser}/2$. In this configuration the atoms with a De-Broglie-wavelength $\lambda_{beam} = h/p$ take the role of the X-ray beam and are diffracted on the standing light wave. We speak of Bragg scattering if the parameters are such that we only see scattering if the initial angle between the atomic beam and the laser fulfills the Bragg condition Eq. 5.1 [3–5]). This can be expressed alternatively in terms of the momentum along the standing wave:

$$p_{\parallel, in} = N \hbar k \quad (5.2)$$

$$p_{\parallel, out} = \pm p_{\parallel, in}, \quad (5.3)$$

where k is the laser wavenumber $2\pi/\lambda_{laser}$.

In Figure 5.2 three examples of recorded detector images are given for different angles θ . In the upper image the laser is exactly perpendicular to the atomic beam (zeroth order Bragg scattering). In the other two images the laser beam is slightly rotated such that

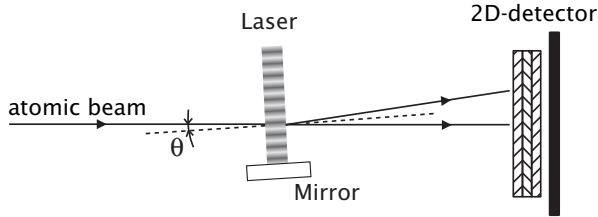


Figure 5.1: Schematic representation of the experimental setup for atomic Bragg scattering

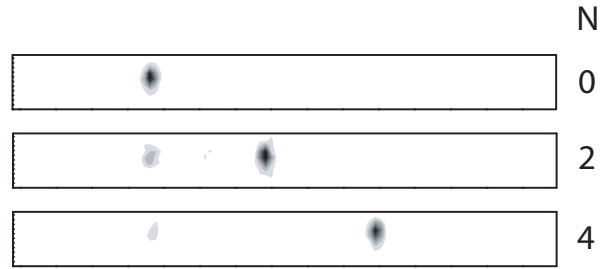


Figure 5.2: Detector images for 0th, 2nd and 4th order Bragg scattering

the initial parallel momentum p_{\parallel} is exactly 2 and 4 times the photon momentum $\hbar k$. We recognize Bragg scattering by the fact that there are only two peaks visible at most. One peak is what remains of the original beam. The other spot is formed by atoms that are diffracted by the light field or, in this case, specularly reflected from the equipotential planes of the light field. The distance between these two peaks corresponds to a velocity difference of exactly $2N$ photon recoils, as prescribed by Eqs. 5.2 and 5.3.

The Bragg condition (Eq. 5.2) only describes an exact resonance condition, but obviously there will still be some scattering when there is a slight mismatch. If this process is used as a beamsplitter in an atom interferometer, one wants to make the maximally allowed mismatch as large as possible to increase the tolerance for experimental fluctuations and for imperfect beam collimation (spread in θ). At some point, however, this acceptance angle becomes so large that the atoms start to diffract in several orders simultaneously, thereby complicating the signal of the interferometer. The optimal settings for this kind of beamsplitter therefore are those at which the full acceptance angle corresponds to a parallel momentum of one photon recoil, the maximum value without overlap between orders. To be able to set the acceptance angle to exactly this value, we formed a model to predict the dependence of this tolerance to experimental parameters such as the diffraction order and the laser intensity (Section 5.5).

5.2 Mathematical Description

In the experiment, we applied a magnetic field along the laser and used σ^+ polarized light in order to select single lower and upper level magnetic substates. In that case we can accurately describe the interaction of the atoms with the standing light wave by the model of a two level atom and a single frequency laser beam [6, 7].

The laser is far detuned ($\Delta_l = 1(2\pi)$ GHz) so that the population of the upper level is very small ($\sim 10^{-4}$) and the chance that an atom spontaneously emits a photon is small. Furthermore, the random recoil of the spontaneously emission generally removes the atom from the bright spots on the detector that represent the coherent diffraction. This allows us to easily filter out the few atoms that have spontaneously emitted by looking at the spatial profile on the detector. We can then simply consider (the remaining) spontaneous

emission as a loss process and describe the interaction with the pseudo-Hamiltonian

$$\begin{aligned} \hat{H} = & \frac{\hat{\mathbf{p}}^2}{2m} + \hbar \left(\omega_0 - i\frac{\Gamma}{2} \right) |e\rangle\langle e| \\ & + \frac{\hbar}{2} \Omega(\hat{z}) \left(e^{i(k\hat{x} - \omega_1 t + \phi_1)} + e^{i(-k\hat{x} - \omega_1 t + \phi_2)} \right) (|e\rangle\langle g| + |g\rangle\langle e|). \end{aligned} \quad (5.4)$$

Here $|e\rangle$ is the atomic excited state which has a decay rate Γ and an energy difference $\hbar\omega_0$ with the ground state $|g\rangle$. The standing light wave consists of two running wave components with frequency ω_l that propagate in opposite direction with reference phases ϕ_1 and ϕ_2 that determine the position of the zeros of the light field. In this case we take two antiparallel plane waves with an envelope that depends only on z : $\Omega(\mathbf{r}) = \Omega(z)e^{\pm ikx}$. This is a good approximation if the Gaussian waist of the laser profile is large (we typically use ~ 1 mm) and the divergence is small.

In the experiments the energy of the atom typically changes by a few (~ 50) photon recoils (see Section 5.3). Because the velocity of the atoms transverse to the laser (the axial velocity, v_z) is orders of magnitude higher than the recoil velocity, this energy difference has a negligible effect on the axial velocity. We can then safely take v_z constant and transform to a coordinate system that moves along the z -axis at this velocity. If we also make the usual rotating wave approximation, we can reduce the Hamiltonian (Equation 5.4) to a 1 dimensional form:

$$\hat{H}_{1D} = \frac{\hat{p}_x^2}{2m} + \hbar\Omega(v_z t) \cos(k\hat{x} + \phi_1 - \phi_2) (|e\rangle\langle g| + |g\rangle\langle e|) + \hbar \left(\Delta_l - i\frac{\Gamma}{2} \right) |e\rangle\langle e|, \quad (5.5)$$

where Δ_l is the laser detuning, $\omega_l - \omega_0$.

The effect of this Hamiltonian can best be understood from the matrix components in momentum representation:

$$\begin{aligned} \langle p_1, g | \hat{H}_{1D} | p_2, g \rangle &= \frac{p_1^2}{2m} \delta(p_1 - p_2) \\ \langle p_1, g | \hat{H}_{1D} | p_2, e \rangle &= \frac{1}{2} \hbar\Omega(v_z t) \left(\delta(p_1 - p_2 + \hbar k) e^{i\phi_2} + \delta(p_1 - p_2 - \hbar k) e^{i\phi_1} \right) \\ \langle p_1, e | \hat{H}_{1D} | p_2, e \rangle &= \left(\frac{p_1^2}{2m} + \hbar\Delta_l - i\frac{\hbar\Gamma}{2} \right) \delta(p_1 - p_2). \end{aligned} \quad (5.6)$$

The delta-functions in the middle expression indicate that the momentum of the atom changes by $\hbar k$ each time it is excited by a photon. De-excitation by stimulated emission of this photon gives a second momentum kick, so that each absorption/emission cycle adds $2, 0$, or $-2\hbar k$. If the initial wavefunction is a plane wave with momentum p_0 we can, without loss of generality, describe the wavefunction as a superposition of an infinite number of plane waves in the ground state that have momentum $p_0 + 2n\hbar k$ plus plane waves in the excited state with momentum $p_0 + (2n + 1)\hbar k$.

A partial energy diagram of the levels that are involved in the diffraction process is given in Figure 5.3 for the case that the original momentum is an odd number times the photon momentum. The thick lines indicate the accessible momentum states of the ground and the excited level. The associated energy of these states is the sum of the internal energy $\hbar\omega_0$

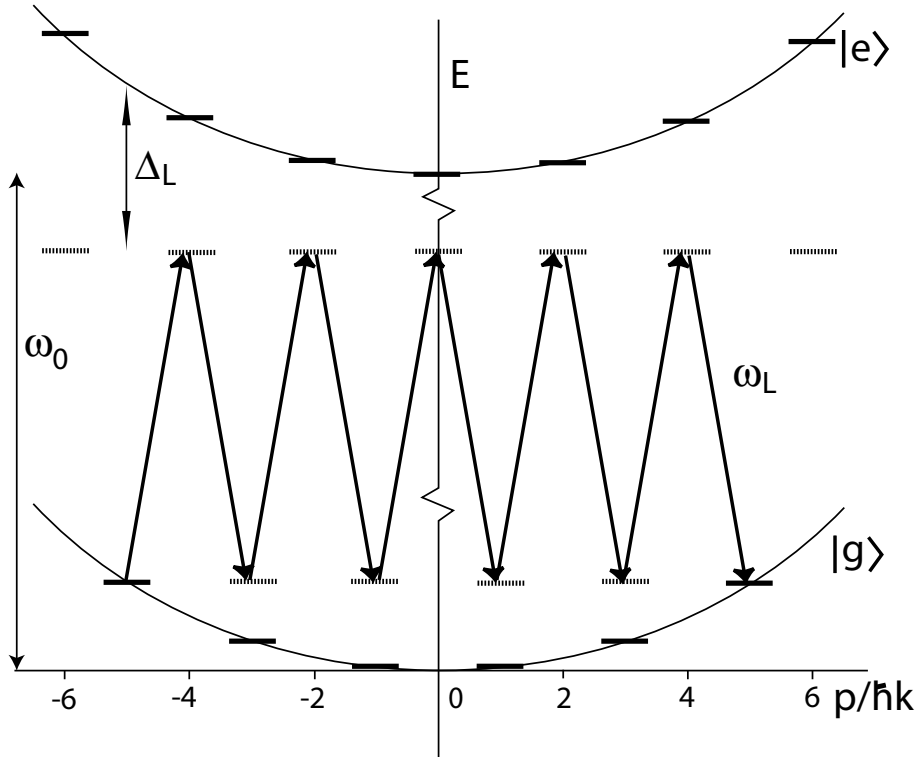


Figure 5.3: Partial energy diagram for the diffraction of a two-level atom on a standing light wave. In the case of Bragg scattering, the two degenerate momentum states are coupled through a number of off-resonant ground and excited level states.

and the kinetic energy $p^2/2m$. As an example, a minimum number of (virtual) transitions are indicated that are needed for fifth order Bragg scattering. This process requires at least 10 single photon transitions to off-resonant states in both the ground and the excited level.

In this reduced basis where the momentum states are separated by discrete steps the Schrödinger equation transforms into an infinite set of coupled differential equations. For numerical calculations we used a basis set of 64 momentum states where we continuously checked that the higher momentum states are not populated during the process. The truncated set of equations is numerically integrated using a NAG routine. In the following we will only refer to the reduced version of the Hamiltonian with the discrete momentum basis.

The Hamiltonian Eq. 5.6 shows that a change in momentum also adds the phase factor of the laser component involved. It is not so difficult to show [8] that the atoms that are diffracted to the N th order have acquired a phase $N(\phi_2 - \phi_1)$. This phase is essential for the full interferometer. However, because in this chapter we are only interested in scattering probabilities, we will ignore this phase for now.

5.3 Eigenvector Approach

The results that are obtained from a full integration of the Schrödinger equation describe the measurements very well [6]. It is however insightful to look at the process in terms of eigenvectors and eigenvalues of the Hamiltonian.

Dynamically, there is no restriction on the allowed momentum (within the discrete momentum basis) that an atom can take during and after the interaction with the laser. We see, however, that in the case of Bragg scattering the atoms only end up with the original momentum, or with the opposite momentum if this is accessible through a $2N$ -photon exchange. It seems that scattering only takes place between two momentum states that have the same (kinetic) energy. Quantum mechanically this is described by the adiabatic following of the instantaneous eigenfunctions.

We calculated the full set of eigenvalues of the Hamiltonian matrix (Eq. 5.6 in the discrete momentum basis) by numerical diagonalization. In Figure 5.4 the lowest few eigenvalues (in terms of the photon recoil energy $\hbar\omega_{rec} = \hbar^2 k^2 / 2m$, $\omega_{rec} = 42(2\pi)$ kHz) are given for the reduced Hamiltonian with $\Gamma = 0$ and $p_0 = 0$. The eigenvalues are plotted as a function of z so that we can recognize the Gaussian profile of the laser with waist w_{laser} .

In the case of fifth order Bragg scattering, the initial wavefunction (at the left of the graph) is a plane wave with momentum $5\hbar k$. This is an eigenfunction of the Hamiltonian without the laser ($\Omega = 0$) and has an energy of $25 \hbar\omega_{rec}$. Because it is an eigenfunction, the atoms momentum would (of course) not change if there were no laser. As the laser intensity increases, however, the momentum states are no longer eigenfunctions and in general the wavefunction evolves into a superposition of all possible momentum states. However, if the laser intensity increases slowly enough, the atoms follow the energy curve (like in Fig. 5.4) and the associated eigenfunction. This process is called adiabatic following.

It can be understood as a continuous series of projections of the wavefunction to the new eigenfunctions. In this process, the new eigenfunctions that are closest in energy receive the largest fraction of atoms. If the intensity increases slowly enough, the wavefunction will each time be projected completely onto a single new eigenfunction and all atoms will end up in the same eigenstate.

At zero laser intensity, momentum states with opposite momentum are energetically degenerate. The interaction with the light field lifts the degeneracy and it can be shown that in the limit of no laser intensity, the eigenfunctions (at resonance of the Bragg condition) are given by the symmetric and the antisymmetric combination of these two momentum states. In the case of fifth order Bragg scattering the two eigenstates that are energetically closest to the original momentum state are:

$$\begin{aligned} \lim_{\Omega \rightarrow 0} |\Psi_5\rangle &= \frac{1}{\sqrt{2}} (|5\rangle + |-5\rangle) \\ \lim_{\Omega \rightarrow 0} |\Psi_6\rangle &= \frac{1}{\sqrt{2}} (|5\rangle - |-5\rangle). \end{aligned} \quad (5.7)$$

The wavefunctions $|\Psi\rangle$ are the instantaneous eigenfunction of the Hamiltonian and its index indicates the ordering of the associated eigenvalues. The number inside the other kets indicates the momentum in terms of $\hbar k$. Thus, exactly on resonance of the Bragg condition (correct angle between laser and atoms) the initial state projects exactly 50-50

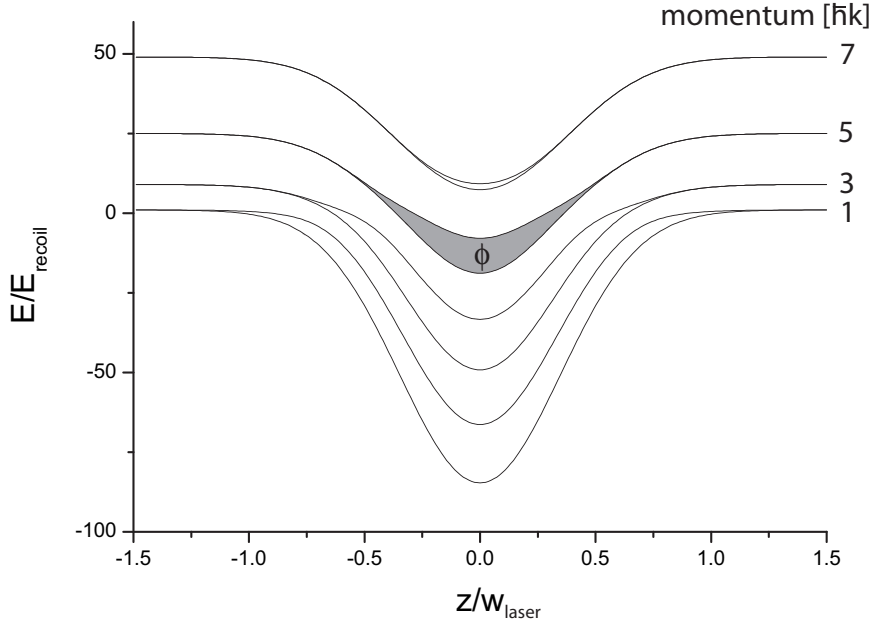


Figure 5.4: Lowest few eigenvalues of the reduced Hamiltonian (at resonance of the Bragg condition) as a function of the position z along the laser profile.

onto the two eigenfunctions $|\Psi_5\rangle$ and $|\Psi_6\rangle$. As the laser intensity increases, the energies of these two eigenfunctions start to diverge and the two eigenfunctions adiabatically evolve into a different form. The distribution of atoms over these two remains unchanged (50/50). At the end, the energies of the two populated eigenfunctions converge and the wavefunction returns to a superposition of the the two plane waves $|5\rangle$ and $|-5\rangle$.

In this simple picture, we have effectively formed a two path interferometer. The incoming atoms are distributed evenly over the two nearest eigenfunctions. As long as they are separated in energy, these two components have a different phase evolution that is given by the energy difference and the travel time: $\phi = \int \Delta E(\tau) d\tau / \hbar$. In Graph 5.4 the phase difference between the two paths is indicated by the shaded area. After the interaction, the detection of the atoms on the detector effectively projects the wavefunction on the $|5\rangle$ and $|-5\rangle$ momentum states. The full process then is described as follows

$$\begin{aligned}
 |5\rangle &\rightarrow \frac{1}{\sqrt{2}}(|\Psi_5\rangle + |\Psi_6\rangle) \\
 &\rightarrow \frac{1}{\sqrt{2}}(|\Psi_5\rangle + e^{i\phi}|\Psi_6\rangle) \\
 &\rightarrow \frac{1}{2}(1 + e^{i\phi})|5\rangle + \frac{1}{2}(1 - e^{i\phi})|-5\rangle.
 \end{aligned} \tag{5.8}$$

We see that the atoms oscillate between the two degenerate momenta as a function of the phase area ϕ . This effect is called the Pendellösung oscillation [7, 9]. For zero laser power, the phase area is zero and the atoms retain the original momentum. As the laser power is increased, the phase area increases and the atoms oscillate to momentum $-5\hbar k$ (at $\phi = \pi$) and back.

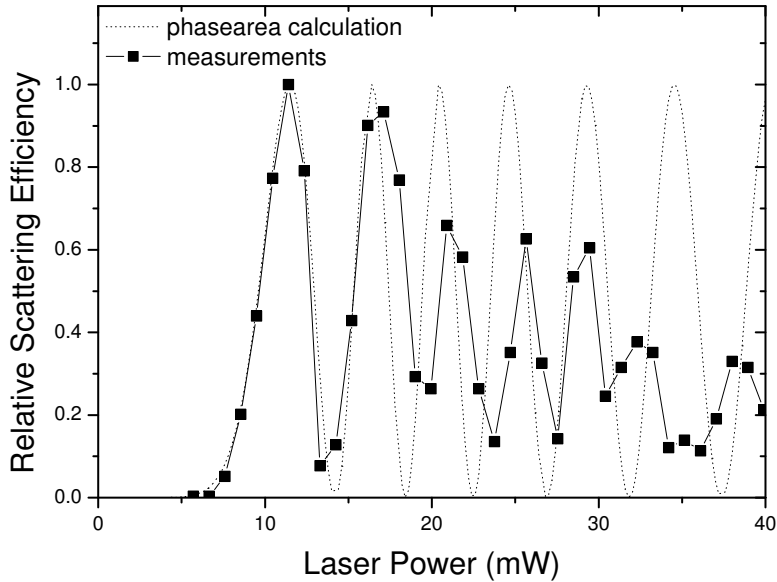


Figure 5.5: Measured Pendellösung oscillations for fifth order Bragg scattering with a comparison with the phase area calculations. $\Delta_l=1(2\pi)$ GHz, $w_{laser}=1.6$ mm, $v_{\perp}=250$ m/s.

Measurements of the Pendellösung effect are plotted in Figure 5.5, where the fraction of atoms with momentum $p = -5\hbar k$ is plotted versus the total single beam laser power, with the overall maximum fraction scaled to 1. The absolute value of the diffraction efficiency for these measurements is quite low ($\sim 40\%$), because we used a relatively large divergence ($\theta_{FWHM} \approx 100 \mu\text{rad}$) of the atom beam (see Section 5.4). The dashed line is the result of a calculation with the above mentioned phase-area method without any free parameter, except for a 5% correction to the measured laser power. The graphs shows five clear oscillations that stay in phase with the phase area calculations. For higher laser power the amplitude of the measured oscillation decreases because of losses by spontaneous emission and scattering to other diffraction orders (see also [10]).

5.4 Acceptance Angle

The phase area method gives an excellent description of the phase of the Pendellösung oscillations, but it assumes that the angle between atom beam and laser is exactly on the Bragg condition and that there are no transitions between adiabatic states during the interaction. For a small misalignment this model predicts that there is no scattering at all, a statement that is obviously wrong. For the design of the interferometer we need to know the scattering probability as a function of a small mismatch in order to choose the optimal divergence for the atomic beam.

For first order Bragg scattering an analytic expression for this scattering profile can be obtained by reducing the model to a two level system with a 2-photon Raman coupling through a far detuned excited level. See [11] for the case of a square pulse and [12] for a hyperbolic secant shape. For higher order Bragg scattering no analytic expression exists yet, because there are always intermediate (momentum) ground level states that are not far detuned (see Fig. 5.3), which makes it more difficult to find an analytic expression.

We performed extensive measurements in order to determine the acceptance angle for Bragg scattering. To this end, the diffraction profile was measured for a large number of laser angles at a number of different laser powers. An example of such a series is given in Fig. 5.6. In this graph 75 one-dimensional detector images (atom beam intensity, integrated over y) as a function of x are given in grayscale with the laser angle as the second coordinate. The grayscale is purposely saturated at high intensity to clarify the narrow and low intensity peaks. For the largest part of the range in angle (vertical axis) hardly any atoms are diffracted and the atoms hit the detector at the position of the original peak around $x=14.7$ mm. Only if the Bragg condition is approximately fulfilled, there appears a significant second peak on the detector. The third order diffraction peak is missing. This is caused by the fact that the scan was performed at a constant value of the laser power, where the Pendellösung oscillation for this particular order happens to be right at a minimum.

The divergence of the atom beam with these measurements was $\sigma_\theta = 21 \mu\text{rad}$. However, the widths of the diffraction peaks in terms of the laser angle in Fig. 5.6 are much larger than this, especially for the lower orders. To get a better view on the acceptance angle, we counted the total number of atoms that ended up in each diffraction order. For this, the atomic positions were binned with bin sizes that were the equivalent of 1 order ($2\hbar k$). As an example of the results, the number of atoms in the fourth order diffraction peak is plotted in Figure 5.7 as a function of the laser angle, expressed in atomic momentum along the laser. There is a clear maximum in the number of atoms around $p_{\parallel} = 4\hbar k$, the fourth order Bragg angle. The tolerance on the Bragg condition (acceptance angle) is given by the width of the peak and is determined by a Gaussian fit.

5.5 Demkov Model

The numerical calculations, described earlier, correctly predict the Bragg tolerance. However, these calculations are in a sense pure “black box” simulations, providing little insight and no handles for convenient parameter optimization. In this section we will therefore develop an analytic model for the direct estimation of the acceptance angle.

Even if the laser angle is not set to the Bragg condition, the atoms are still distributed over only two possible momentum states. It then seems likely that also in this case, the process can be described by a two-level system. We will look for a model in which two (momentum) states with a fixed energy difference experience a peaked interaction that is determined by the Gaussian shape of the laser profile. There is a number of known two state models that have an analytic solution (for an overview see [13, 14]). The most appropriate of these is the Demkov model [15].

The Demkov model describes the non-adiabatic transfer between two states with a

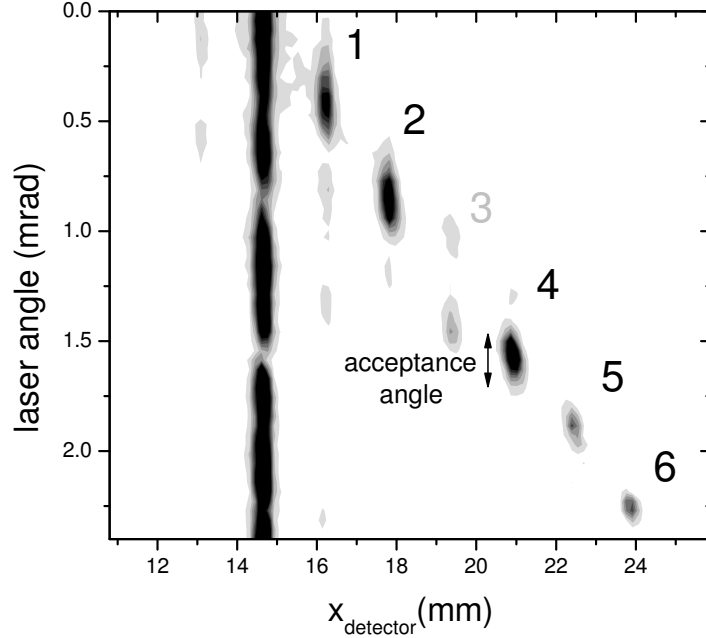


Figure 5.6: 1-D detector intensity (diffraction profile integrated in the y direction) as a function of the laser angle. Dark points indicate high intensity of the atom beam.

fixed energy difference ΔE and a peaked interaction strength $\Omega_{Demkov}(t)$ that changes exponentially in time. In matrix form we can write the Hamiltonian:

$$H_{Demkov} = \begin{pmatrix} \Delta E/2 & \Omega_{Demkov}(t) \\ \Omega_{Demkov}(t) & -\Delta E/2 \end{pmatrix} = \begin{pmatrix} \Delta E/2 & \beta e^{-\gamma|t|} \\ \beta e^{-\gamma|t|} & -\Delta E/2 \end{pmatrix}. \quad (5.9)$$

In the beginning and at the end, the interaction strength is zero, but during the interaction it peaks to a value β that is much larger than the energy difference.

It turns out that the instantaneous eigenstates are adiabatically followed, except around the points in time $\pm t_0$ where the interaction strength is equal to the energy difference, $\Delta E = \beta \exp(-\gamma|t_0|)$. Near these points, the non-adiabatic transitions occur. It can be shown that the total transition probability P_{Demkov} after the entire pulse equals:

$$P_{Demkov} = \operatorname{sech}^2 \left(\frac{\pi \Delta E}{2 \hbar \gamma} \right) \sin^2(\phi_0/2), \quad (5.10)$$

$$\phi_0 = \frac{2}{\hbar} \int_{-\infty}^{\infty} \Omega_{Demkov}(t) dt. \quad (5.11)$$

We see the qualitative agreement of this formula with the measurements: a peaked shape

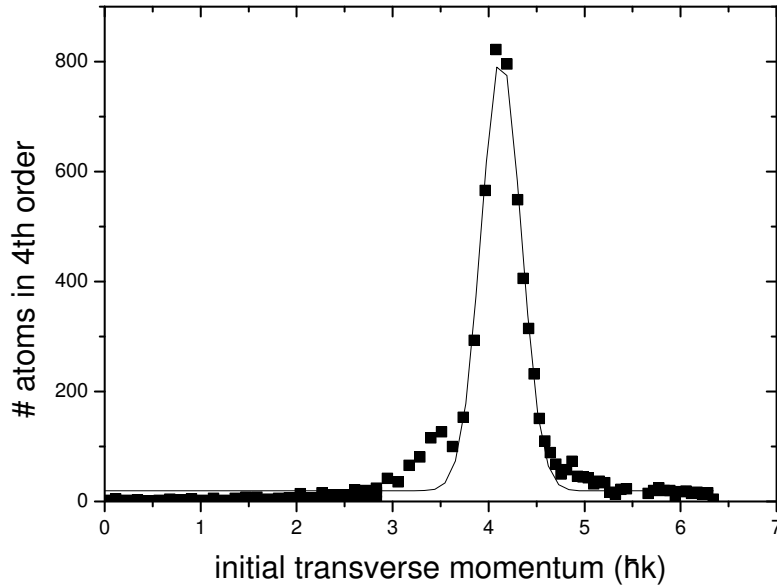


Figure 5.7: Total number of atoms that ended up in the fourth order diffraction peak as a function of the laser angle in terms of the atomic momentum along the laser together with a Gaussian fit.

as a function of the energy difference (laser angle) and an oscillating term as a function of the phase area ϕ_0 (Pendellösung oscillations).

In the Bragg scattering process the two levels of the Demkov model correspond to the incoming plane wave and the plane wave that is closest in (kinetic) energy, the reflected wave. Although these plane waves have adiabatically evolved into a complex superposition at the peak of the laser intensity, the non-adiabatic transitions take place in the tails of the laser profile where these adiabatic eigenfunctions are still approximately equal to the original pure momentum states. The interaction between these states is not in actuality exponential in time: it follows the intensity of the Gaussian laser profile. However, the transitions occur in the tails of the Gaussian, where the effective interaction can be approximated by an exponential. In between the two points $\pm t_0$ we only need to know the relative phase evolution. In Equation 5.10 this phase evolution is written in terms of the off-diagonal terms of the 2-level Hamiltonian. For $\Delta E = 0$, however, this off-diagonal term is equal to half the adiabatic energy difference (difference in eigenvalues). If we make the translation to the full system with all the momentum states, we see that the phase ϕ_0 (Eq. 5.11) is thus described by the phase area method of Section 5.3, where the phase area is always calculated on resonance of the Bragg condition even if the two momentum states have an energy difference.

To calculate the scattering probability we have to match the parameters ΔE and γ to our situation. The energy difference is simply the difference in kinetic energy between the two momentum states. One can readily show that with an offset momentum $\Delta N \hbar k$ from

N th-order resonance the energy difference is

$$\Delta E = 4\hbar\omega_{rec}N \Delta N. \quad (5.12)$$

The parameter γ is more difficult to calculate, but can be obtained from a local approximation around t_0

$$\gamma = \frac{d\Omega_{eff}(t_0)/dt}{\Omega_{eff}(t_0)}, \quad (5.13)$$

where Ω_{eff} is the effective $2N$ photon Rabi frequency between the two levels. This effective Rabi frequency can be obtained by adiabatically eliminating all other momentum states. For low laser intensity this can be approximated by [5, 16]

$$\Omega_{eff}(t) = \frac{\Omega_0^{2N}(t)}{2^{4N-3}((N-1)!)^2 \Delta_l^N \omega_{rec}^{N-1}}, \quad (5.14)$$

where Ω_0 is the single photon Rabi frequency, $\Omega_0(t) = \Gamma\sqrt{I(t)/2I_{sat}}$. This is the generalization of a two-photon Raman transition to a $2N$ -photon transition. The numerator is the product of the interaction strengths for each intermediate transition and the denominator is the product of the detuning of each intermediate level. In this approximation the small shift ΔE is neglected.

For a Gaussian profile of the laser Equations 5.14 and 5.13 result in

$$\gamma = -4Nt_0/\tau^2, \quad (5.15)$$

where $\tau = w_{laser}/v_{\perp}$, with w_{laser} the Gaussian waist radius at $1/e^2$ height of the laser intensity profile. The point t_0 where the interaction takes place is given by the solution of the equation $\hbar\Omega_{eff}(t_0)/2 = \Delta E$, yielding

$$t_0 = \tau \sqrt{\frac{1}{2N} \ln \left(\frac{\Omega_0^{2N}}{(16\Delta_l \omega_{rec})^N ((N-1)!)^2 N \Delta N} \right)}. \quad (5.16)$$

The expression for the effective Rabi frequency (Eq. 5.14) is only valid if the detuning of all intermediate levels (see Fig. 5.3) is much larger than Ω_0 . The laser detuning is much larger than the maximum single photon Rabi frequency ($\Delta_l = 1(2\pi)$ GHz, $\Omega_{0,max} \approx 63(2\pi)$ MHz) and the elimination of these states is a very good approximation. The momentum states of the ground level, however, are only detuned by a few times the photon recoil frequency, which is smaller than Ω_0 . To test the validity of Equation 5.14 we also numerically calculated the effective Rabi frequency by numeric adiabatic elimination of all off-resonant states. We found that Equation 5.14 is valid to within 10% when the 2-photon Rabi frequency satisfies $\Omega_{eff,2photon} = \Omega_0^2/2\omega_{rec}\Delta_l < 10$ which gives $\Omega_0 < 500\omega_{rec} = 21(2\pi)$ MHz. Since typically $t_0 \approx \tau$ we get $\Omega_0(t_0) = 23(2\pi)$ MHz and we find that the laser intensity at the Demkov point t_0 is low enough to use expression 5.14. At the peak of the laser profile, however, the intensity is too high and we will have to compute the phase area numerically.

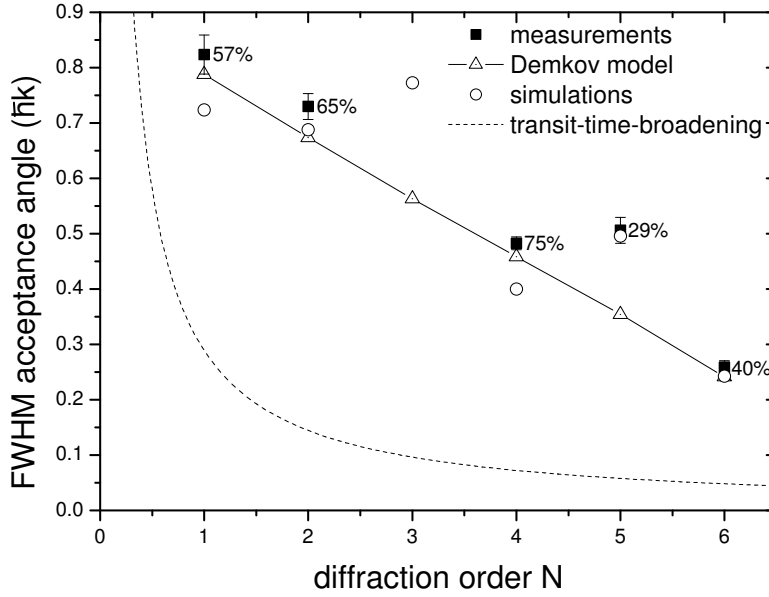


Figure 5.8: FWHM acceptance angle for Bragg scattering as a function of the Bragg order ($w_{laser}=1.6$ mm, $\Delta_l=1(2\pi)$ GHz, $P=21$ mW). The percentages next to the measurements indicate the maximum scattered fraction of atoms.

5.6 Measurements

In Figure 5.8 the FWHM acceptance angle for the scattering probability is plotted as a function of the diffraction order N with constant laser power. The filled squares indicate the result of a Gaussian fit through measurements like in Fig. 5.7. The point for 3rd order scattering is missing because at this particular laser power, the Pendellösung oscillation has reached its minimum so that no atoms are scattered, regardless of the tolerance. The error bars on the measurements give the uncertainty from the fitting routine and the percentages next to the measurements indicate the maximum scattered fraction of atoms to that momentum for these settings.

The results from the Demkov model are depicted by triangles that are connected by the line. These values, indicate FWHM of the sech^2 part of the scattering probability (Eq. 5.10) and are given by the value of $2\Delta N_{HWHM}$ at which the argument $\pi\Delta E(\Delta N_{HWHM})/2\hbar\gamma(\Delta N_{HWHM}) = 0.88$. The Pendellösung phase ϕ does in principle depend on the laser angle and might change the tolerance through the $\sin(\phi(p_{\parallel}))$ component in the scattering probability. With these calculations, however, we assume that over the range of one resonance peak this phase does not change by much. We therefore take this phase area constant per diffraction order. In that case, the scattering profile is fully determined by the sech function. The measured acceptance angles agree quite well with this Demkov model, except for the fifth order, where the scattering efficiency is quite low.

The open circles in the graph are the result from a series of full numerical calculations (Sec. 5.2). These agree quite well with the measurements and the model. The results from the calculations seem to vary more per diffraction order than the measurements which have a very smooth behavior. This is probably caused by the fact that parameters such as laser power varied slightly during the experiment, causing some effective averaging that smooth out the variations in the measurements. If we evaluate the acceptance angle from the simulations at a slightly different laser power, where the maximum transfer efficiency is maximal, the simulated acceptance angles agree much better with the Demkov model. The actual acceptance angle thus strongly depends on the laser power.

We might be tempted to use a much simpler criterion for the tolerance on the Bragg condition based on the idea of transit time broadening, i.e, the energy uncertainty associated with the finite interaction time. In that case the acceptance angle is set by the angle offset at which the difference in kinetic energy between the original and the scattered beam exceeds the transit-time broadened energy uncertainty $\Delta E = \hbar/\tau$. The result of this estimate is given in Fig. 5.8 by the dashed line. For the interaction time we took the value that corresponds to the waist of the laser profile. Clearly, this estimate results in an acceptance angle that is much too low and that drops off much more quickly with the diffraction order. Another choice of τ would result in different values for the acceptance angle. The trend as a function of N , however, would remain the same.

As another check on the Demkov model, we also measured the tolerance on the Bragg condition as a function of the total laser power. For this we again measured the total number of atoms that is scattered to second order as a function of the laser angle for a fixed laser power and determined the Gaussian width of this scattering probability. This was repeated for 3 different values of the laser power. The result of these measurements is given in Figure 5.9 by the filled squares. These measurements agree well with the Demkov model (full line). The trend in the graph is that the tolerance only increases very slowly with the laser power. The model shows a sharp decrease in the acceptance angle for very low laser intensities (<2 mW). At this point however, the phase area ϕ is also too small to see any scattering so that the acceptance angle has little meaning.

The acceptance angles that result from the full numerical calculations are given by the open circles that are connected by the dashed line. The size of these circles indicate the maximum transfer efficiency and the graph shows that for each laser power at which the transfer is maximal (largest circles), the acceptance angle agrees very well with the Demkov model. However, when following a single section of the dashed line connecting the simulations, i.e, when traversing a single maximum of the Pendelösung oscillations, the acceptance angle changes rapidly as a function of the laser power. This discrepancy is probably caused by the effect of the laser angle on the phase area. Although this effect only introduces a small shift in the Pendellösung oscillation, this shift itself could have a relatively large effect on the width of the acceptance profile. A full calculation of the effective interaction strength by adiabatic elimination of the off-resonant levels instead of the approximation 5.14 would probably give an even better correspondence. However, for the moment we can conclude that the Demkov model captures the physics of the Bragg tolerance correctly, both qualitatively and quantitatively, and provides a very convenient handle to optimize the experimental parameters.

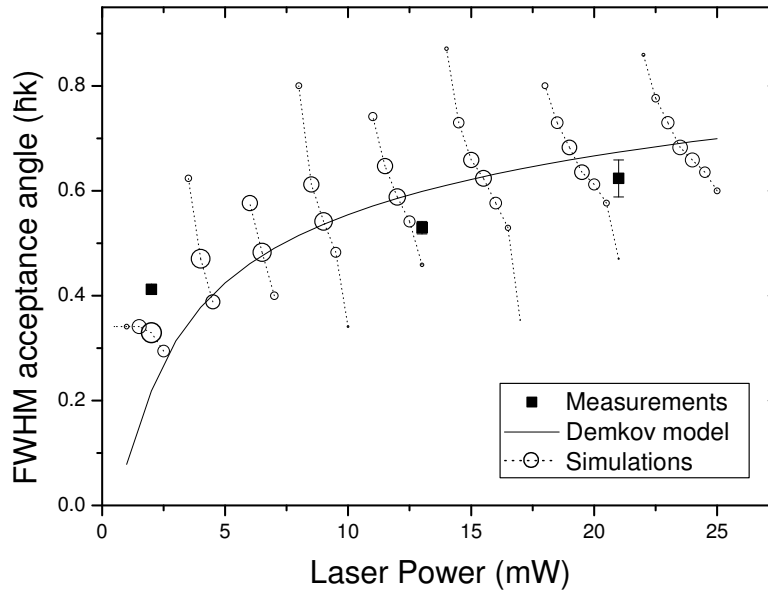


Figure 5.9: FWHM acceptance angle for Bragg scattering as a function of the single beam laser power ($w_{laser}=1.6$ mm, $\Delta_l=1(2\pi)$ GHz, $N=2$). The three measurements were taken for maximum scattering. The circles, connected by the dashed lines, give the results from the numerical calculations and the size of these circles indicate the maximum transfer at that laser power. The jumps in the acceptance angles occur at the minima of the Pendelösung oscillations.

5.7 Optimal waist

The previous paragraph showed that the Demkov model is in excellent agreement with the measurements and the simulations. In this Section we will now use this model to determine the optimal settings to get an optimal acceptance angle and to diffract as many atoms as possible without any diffraction to unwanted angles. The goal is then to get a FWHM acceptance angle for Bragg scattering of $1\hbar k$.

The scattering probability (Equation 5.10) consists of two parts that are (largely) independent and can be optimized separately: the oscillating part depends on the phase area ϕ , representing the Pendelösung oscillation and the envelope function depending on the energy difference representing the tolerance. The phase area has to be set differently for the atom beam splitters and the atom beam mirrors, but for now we will consider the mirrors, $\phi = \pi$. At large laser detuning, the independent parameters that we can use to tune the process are the diffraction order N , the effective 2-photon Rabi frequency $\Omega_{eff,2photon} = \Omega_0^2/2\omega_{rec}\Delta_l$ and the interaction time τ . When we choose a fixed order N and hence a fixed diffraction angle, the two conditions for the phase area and acceptance angle determine the optimal values for the laser power and the interaction time.

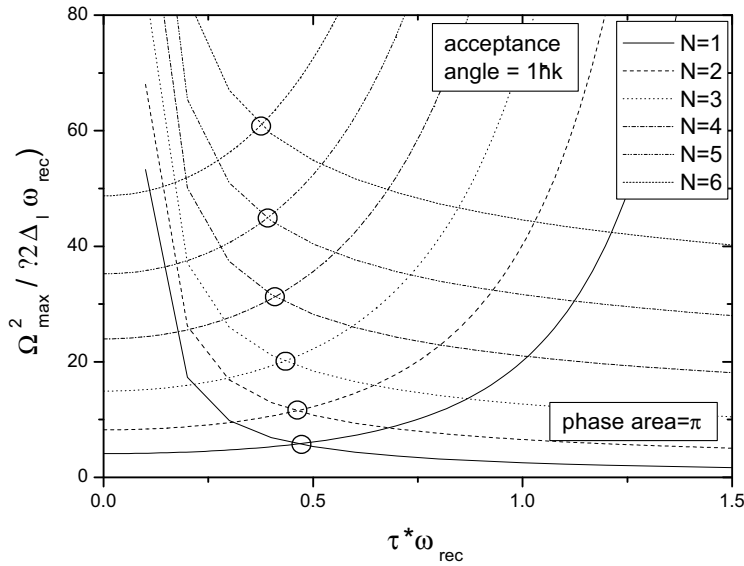


Figure 5.10: Relation between the laser power and waist following from two criteria: the first maximum of the Pendellösung oscillation (phase area = π) and an optimal acceptance angle according to the Demkov model. The optimal laser waist is where the two lines intersect (inside circles). $\Delta_l = 1(2\pi)$ GHz.

In Figure 5.10 the relation between the value of Ω_0 at the center of the laser profile (Ω_{max}) and τ that results from each of the two criteria is plotted for several values of N . The relation for the phase area is obtained by a numerical integration routine combined with a search algorithm that searches for the optimal value of Ω_{max} for each value of τ . The other lines are the result from the required HWHM width of the envelope. They are the result of combining Equations 5.12, 5.14 and 5.15, yielding:

$$\frac{\Omega_{max}^2}{2\omega_{rec}\Delta_l} = 8 \left[((N-1)!)^2 N \Delta N \right]^{1/N} e^{2\left(\frac{\pi \Delta N \omega_{rec} \tau}{2 \times 0.88}\right)^2}, \quad (5.17)$$

where $\Delta N = 0.5$ for a FWHM acceptance angle of $1\hbar k$. The optimal value for τ and for Ω_{max} for each order N are given by the intersection of the two lines, indicated by the circles in Figure 5.10. For a FWHM acceptance angle of $1\hbar k$ all six diffraction orders require an interaction time of $\tau_{opt} \approx 0.4/\omega_{rec}$ which in our setup gives an optimal laser waist of 0.4 mm, independent of the diffraction order, which is very convenient.

To compare these results with the simulations the procedure described above was repeated for a target acceptance angle of 0.25, 0.5 and $0.75\hbar k$. In Figure 5.11 the results are plotted as required acceptance angle versus the optimal waist (solid symbols). The lines indicate the results from the full numerical simulations. They represent the FWHM acceptance angles that are obtained by a Gaussian fit through the simulations at four values of the laser waist.

Again, the results from the simulations and the Demkov model are close, except for the lowest diffraction order. The most likely explanation for this is that the low momentum

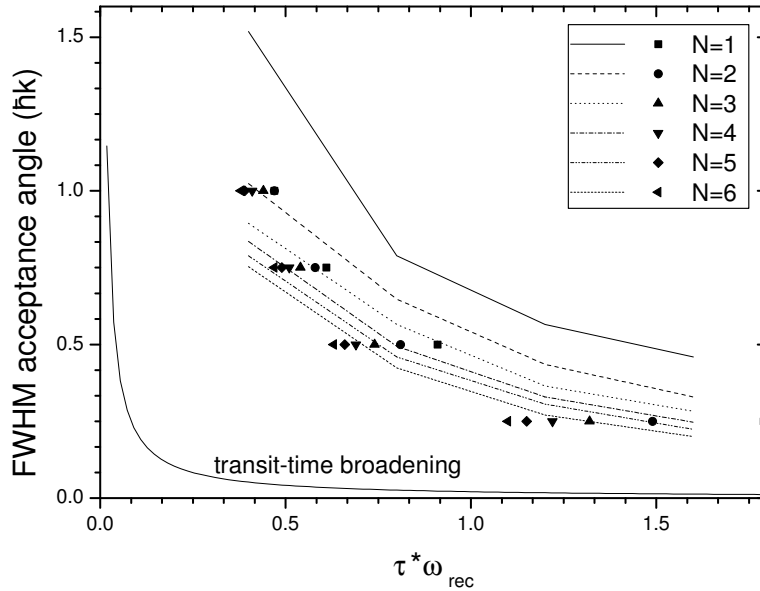


Figure 5.11: The optimal waist for the lowest six diffraction orders and four values of the required acceptance angle. For comparison the lines indicate the acceptance angle that are obtained from full numerical simulations at four different values of the laser waist. The optimal setting that is obtained from a transit-time broadening calculation is also drawn.

states have small energy differences. It is then easier to make non-adiabatic transitions between these states. This makes the used two level approximation less accurate.

The lower line in Fig. 5.11 indicates the result from the transit-time broadening estimate. Again, it is clear that the Demkov model is a much better approximation.

5.8 Conclusion

We have shown in this chapter that atomic Bragg scattering can very well be described by a Demkov model. The presence of Pendellösung oscillations indicate that the interaction of the atoms with the laser is mostly adiabatic and effectively limited to two states. The two relevant states correspond to the initial incoming plane wave and the reflected wave with a momentum difference of $2N\hbar k$ and the smallest energy difference. In the Demkov model, transitions between the two states occur at the two points $\pm t_0$ where the effective interaction strength is equal to the energy difference. When these points are calculated using an analytical approximation for the effective interaction strength it is straight forward to calculate the acceptance angle for Bragg scattering. The dependence of this acceptance angle as a function of the laser intensity and the diffraction order N was tested experimentally. This model, without any adjusted parameters, was found to be in excellent agreement with

the experiments. Although the model works best for laser power with maximum reflection of the atom beam, it is a good tool to estimate the optimal settings for an atom interferometer. For a FWHM acceptance angle of $1\hbar k$ we found $w_{opt} \approx 0.4$ mm, independent of the diffraction order.

Comparison with a widely used transit-time broadening approach revealed that the Demkov model is a great improvement and works much better in predicting the acceptance angle.

References

- [1] E. Fermi and L. Marshall, *Phys. Rev.* **71** 666 (1947)
- [2] Stephan Dürr, Stefan Kunze and Gerhard Rempe, *Quantum Semiclass. Opt.* **8** 531 (1996)
- [3] Peter J. Martin, Bruce G. Oldaker, Andrew H. Miklich and David E. Pritchard, *Phys. Rev. Lett.* **60** 515 (1987)
- [4] M. Kozuma, L. Deng, E.W. Hagley, J. Wen, R. Lutwak, K. Helmerson, S.L. Rolston and W.D. Phillips, *Phys. Rev. Lett.* **82** 871 (1999)
- [5] David M. Giltner, Roger W McGowan and Siu Au Lee, *Phys. Rev. A* **52** 3966 (1995)
- [6] A.E.A. Koolen, G.T. Jansen, K.F.E.M. Domen, H.C.W. Beijerinck and K.A.H. van Leeuwen, *Phys. Rev. A* **65** 041601 (2002)
- [7] G.T. Jansen, *Bragg Diffraction of He* by a Standing Light Wave*, internal report, Eindhoven University of Technology (2001)
- [8] A.C.H. Meesters, *Assessment of Very Large Area Atom Interferometers*, internal report, Eindhoven University of Technology (2003)
- [9] S. Kunze, S. Dürr, and G. Rempe, *Europhys. Lett.* **34** 343 (1996)
- [10] C. Keller, J. Schmiedmayer, A. Zeilinger, T. Nonn, S. Dürr and G. Rempe, *Appl. Phys. B* **69** 303 (1999)
- [11] Stephan Dürr and Gerhard Rempe, *Phys. Rev. A* **59** 1495 (1999)
- [12] C. Champenois, M. Büchner, R. Delhuille, R. Mathenvet, C. Robillaird, C. Rizzo, and J. Vigué, *Eur. Phys. J. D* **13** 271 (2001)
- [13] E.E. Nikitin, S.Ya. Umanskii, *Theory of Slow Atomic Collisions*, (Springer, 1984).
- [14] Bruce W. Shore, *The Theory of Coherent Atomic Excitation*, Volume 1, (Wiley-Interscience, 1990).
- [15] Demkov Yu. N. *Zh. Eksp. Teor. Fjz.* **45** 159 (1963) (*Sov. Phys. JETP* **18** 138 (1964))
- [16] Bruce W. Shore, *Phys. Rev. A* **24** 1413 (1981)

Chapter 6

Interferometer Theory

6.1 Introduction

Atom interferometers are very sensitive to a large variety of physical phenomena such as rotation [1] and gravity [2] and therefore they are excellent devices to measure these effects very accurately. On the other hand, these same effects can be troublesome sources of noise if one is looking for other signals (see for example [3]).

There are numerous effects that contribute to the interferometer phase, including the mentioned inertial effects but also including alignment errors. It is impossible to do a measurement without detailed knowledge of all relevant contributions. Effects of alignment errors on the interferometer phase and contrast were already investigated by Champenois [4], however in this paper each error was taken into account separately and the calculations did not include rotation and gravity. In this chapter we will calculate the full interferometer phase accounting for all possible alignment errors, variations in initial velocity and position and rotation, gravity and a quadratic potential. All of these effects are included simultaneously, so that we can evaluate the cross terms as well.

The ideal interferometer setup is schematically drawn in Figure 6.1. The beam enters the interferometer through the aperture at the left and is subsequently split and recombined by three standing light waves that are positioned at equal distances. The associated classical trajectories that contribute to the detector signal are indicated by the dashed lines.

To calculate the phase difference between the two paths we need to calculate two effects: the interaction with the lasers and the propagation between the lasers. The propagation between the lasers is described in Section 6.2, where the phase evolution is calculated by using a WKB approximation along the classical trajectories. The effect of the lasers is described in Section 6.3. In Section 6.4 we combine the two effects and obtain an expression for all relevant effects that influence the interferometer phase at a detectable level. At the end, in Section 6.5, we evaluate some of the phase terms and translate them into design criteria for the interferometer.

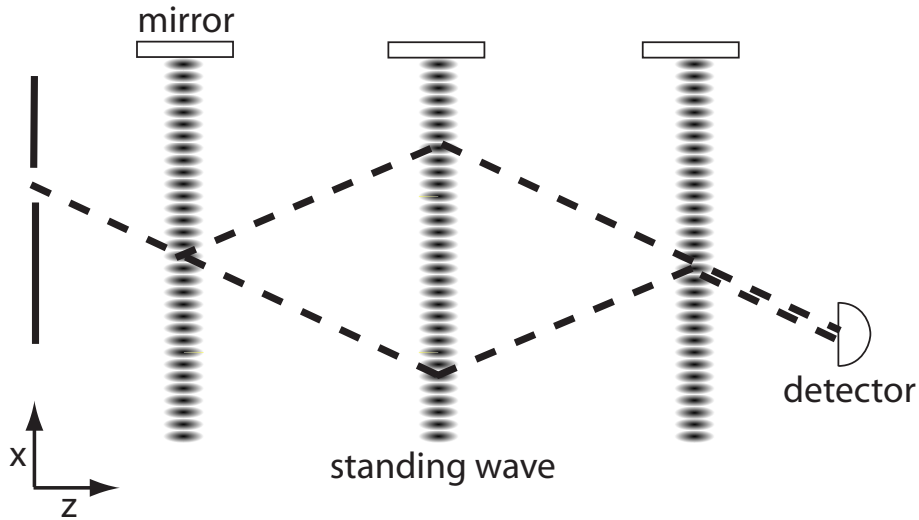


Figure 6.1: Schematic representation of the interferometer setup. The atomic beam enters through the aperture at the left. Three standing light waves positioned at equal distances split and recombine the atom beam. At the end of the setup the beam intensity is measured by a detector.

6.2 Free Propagation

6.2.1 WKB approximation

All parameters in the setup are fixed and the beam that enters through the aperture runs continuously. We can then describe the atoms as a continuous atomic wavefunction. In the interferometer this wavefunction and thus the detector signal is described by the time-independent Schrödinger equation

$$\hat{H}\Psi(\mathbf{r}) = E\Psi(\mathbf{r}), \quad (6.1)$$

with the boundary conditions that are given by the input beam at the aperture

$$\Psi(x, y, z = 0) = \Psi_0(x, y) \quad (6.2)$$

$$d\Psi(x, y, z = 0)/dz = f(x, y) \quad (6.3)$$

and the energy E of Equation 6.1 matching these boundary conditions. The Hamiltonian \hat{H} describes all energy terms within the interferometer region, including the interaction with the lasers and their spatial profile. The intensity at the detector is given by $|\Psi(\mathbf{r}_{detector})|^2$. In the case of a pulsed input beam, this solution is a Fourier component of the full time-dependent solution with frequency E/\hbar .

Unfortunately, it is impossible to get a simple analytic solution from the full problem so we will make a few approximations. First, we will approximate the laser beams by infinitely thin sheets that are approximately perpendicular to the beam axis (see Section 6.3). The interferometer is then divided by these sheets into 4 sections where the effect of the lasers is summarized in a coupling relation for the wavefunctions on either side of each interface. We then have to solve Equation 6.1 for each section of the interferometer with a Hamiltonian

that usually only has a small potential energy term and thus represents “almost free” propagation.

For a reduced Hamiltonian that is at most quadratic in momentum and position the time-independent Schrödinger equation can in principle be solved. That is, the solution can be expressed in terms of (integrals over) standard functions. The full solution to the problem that matches the boundary conditions, however, still gets extremely complicated and is not useful for simple sensitivity relations. We will therefore make a second approximation and consider the classical trajectories of the atoms and use a WKB approximation to calculate the phase.

The following is a simplified version of the result of Maslov [5]. We write the wavefunction $\Psi(\mathbf{r})$ as the product of an amplitude $A(\mathbf{r})$ and a phase factor $\exp(i\phi(\mathbf{r}))$. If the amplitude A varies much more slowly than the phase ϕ (i.e. $(\nabla^2 A)/A \ll (\nabla\phi)^2$) we can use the WKB approximation and decouple the equations for the amplitude and the phase. In general, these equations can still not be solved. However, we are only interested in the phase at the points where the amplitude is high. If the wavefunction at the boundary is peaked at the point \mathbf{r}_0 , the amplitude of the full wavefunction is large in the neighborhood of the classical trajectory that starts at position \mathbf{r}_0 with initial momentum

$$\mathbf{p}_0 = \hbar\nabla\phi(\mathbf{r}_0) \quad (6.4)$$

and energy

$$E = H(\mathbf{p}_0, \mathbf{r}_0). \quad (6.5)$$

It can then be shown that the approximate solution for the phase around this classical trajectory $\mathbf{r}_{cl}(t)$ is given to first order in $\mathbf{r} - \mathbf{r}_{cl}(\tau)$ by

$$\phi(\mathbf{r}) = \phi(\mathbf{r}_0) + \frac{1}{\hbar} \int_0^{\mathbf{r}_{cl}(\tau)} \mathbf{p}_{cl}(t) \cdot d\mathbf{r}_{cl}(t) + \frac{1}{\hbar} \mathbf{p}_{cl}(\tau) \cdot (\mathbf{r} - \mathbf{r}_{cl}(\tau)). \quad (6.6)$$

The second order term can be found in [5]. If the trajectory does not reach the point \mathbf{r} where we want to evaluate the phase, the time $\tau(\mathbf{r})$ describes the time at which the classical trajectory comes closest to this point \mathbf{r} . This time τ is then given by the relation

$$(\mathbf{r} - \mathbf{r}_{cl}(\tau)) \cdot \frac{d}{dt} \mathbf{r}_{cl}(\tau) = 0. \quad (6.7)$$

The phase 6.6 has three contributions: the phase of the wave at the point where it enters the section, $\phi(\mathbf{r}_0)$, the path integral of $\mathbf{p} \cdot d\mathbf{r}$ over the classical trajectory and a continuation of the wave as a plane wave with wave vector $\mathbf{p}_{cl}(\tau)/\hbar$ from the final point $\mathbf{r}_{cl}(\tau)$ to the point \mathbf{r} . In the special case of a non-rotating reference frame the momentum is parallel to the velocity $\mathbf{v} = d\mathbf{r}_{cl}/dt$ (see Subsec. 6.2.2) and the last phase term vanishes, because of the condition 6.7.

Equation 6.6 gives the phase of the wavefunction at any point \mathbf{r} in the region of free propagation (between lasers) with only the classical trajectory as input. The interferometer consists of two arms with multiple sections and the calculation of the interferometer phase requires the evaluation of Equation 6.6 over all partial trajectories.

For a time-based atom interferometer with pulsed lasers the expression for the phase is similar to Equation 6.6, but with two differences. Firstly, the time τ is now imposed

by the pulse sequence and does not have to be calculated from the trajectory. This makes it a lot easier to calculate higher order correction factors for the interferometer phase [6]. Secondly, the path integral over $\mathbf{p}_{cl} \cdot d\mathbf{r}$ is replaced by an integration of the Lagrangian over time [7] which effectively adds a phase integral of $\int E(t)dt/\hbar$. Because of the relative ease of the calculations spatial interferometers are often approximated as time-based by taking the axial velocity constant. This approach, however, can lead to large discrepancies in the interferometer phase if there is a path length difference between the two arms. Although the two approaches produce many phase terms that are equivalent, the two type of interferometers are fundamentally different.

6.2.2 Classical Trajectories

As mentioned above, the calculation of the “propagation phase” only requires the classical trajectory. In this section we will therefore derive an expression for the classical trajectory in terms of the initial position and momentum, where we account for rotation (e.g, the daily rotation of the earth) and potentials.

In classical mechanics the motion of a particle is fully determined by the (classical) Hamiltonian $H(\mathbf{p}, \mathbf{r})$. The trajectory $\mathbf{r}_{cl}(t)$ is given by the Hamilton equations

$$\frac{d}{dt}\mathbf{r}_{cl}(t) = \nabla_{\mathbf{p}}H(\mathbf{p}_{cl}(t), \mathbf{r}_{cl}(t)) \quad (6.8)$$

$$\frac{d}{dt}\mathbf{p}_{cl}(t) = -\nabla_{\mathbf{r}}H(\mathbf{p}_{cl}(t), \mathbf{r}_{cl}(t)). \quad (6.9)$$

We shall limit ourselves in this work to a second order expansion of the potential energy. In the rotating frame the Hamiltonian is:

$$H(\mathbf{p}, \mathbf{r}) = \frac{\mathbf{p}^2}{2m} - m\mathbf{g} \cdot \mathbf{r} - \frac{m}{2}\mathbf{r} \cdot \overset{\Rightarrow}{\Gamma}\mathbf{r} - (\mathbf{r} + \mathbf{R}) \cdot \overset{\Rightarrow}{\Omega}\mathbf{p}, \quad (6.10)$$

where boldfaced symbols indicate column vectors and symbols with an arrow are matrices.

In the case of gravity, the vector \mathbf{g} is equal to the gravitational acceleration, but in the case of a general potential field $V(\mathbf{r})$ the vector $m\mathbf{g}$ contains the first order expansion coefficients $\nabla V(\mathbf{r})$. The matrix $m\overset{\Rightarrow}{\Gamma}$ contains the second order coefficients, $\nabla\nabla^T V(\mathbf{r})$, where the T indicates the transposed vector. The rotation is described by the matrix

$$\overset{\Rightarrow}{\Omega} = \begin{pmatrix} 0 & \Omega_z & -\Omega_y \\ -\Omega_z & 0 & \Omega_x \\ \Omega_y & -\Omega_x & 0 \end{pmatrix}, \quad (6.11)$$

such that

$$\mathbf{r} \cdot \overset{\Rightarrow}{\Omega}\mathbf{p} = -\mathbf{r} \cdot \boldsymbol{\Omega} \times \mathbf{p} = \boldsymbol{\Omega} \cdot \mathbf{r} \times \mathbf{p} \quad (6.12)$$

gives the usual rotational energy term. The matrix notation was chosen over the usual vector notation, because matrix multiplications are easier to work with than vector cross products. The vector \mathbf{R} is the offset of the origin of the coordinate system to the center of rotation (center of the earth if the rotation of the earth is considered, or an arbitrary other point on the rotation axis).

The Hamilton equations 6.8 and 6.9 can be written in the form

$$\frac{d}{dt} \begin{pmatrix} \mathbf{r}_{cl}(t) \\ \mathbf{p}_{cl}(t)/m \end{pmatrix} = \vec{M} \begin{pmatrix} \mathbf{r}_{cl}(t) \\ \mathbf{p}_{cl}(t)/m \end{pmatrix} + \begin{pmatrix} \vec{\Omega}\mathbf{R} \\ \mathbf{g} \end{pmatrix} \quad (6.13)$$

$$\vec{M} \equiv \begin{pmatrix} \vec{\Omega} & \mathbf{1} \\ \vec{\Gamma} & \vec{\Omega} \end{pmatrix}. \quad (6.14)$$

The solution to these equations can be written in terms of the initial conditions and the time-dependent 3×3 matrices \vec{A} , \vec{B} , \vec{C} and \vec{D} and vectors $\boldsymbol{\xi}$ and $\boldsymbol{\zeta}$:

$$\begin{pmatrix} \mathbf{r}_{cl}(t) \\ \mathbf{p}_{cl}(t)/m \end{pmatrix} = \begin{pmatrix} \vec{A}(t) & \vec{B}(t) \\ \vec{C}(t) & \vec{D}(t) \end{pmatrix} \begin{pmatrix} \mathbf{r}_0 \\ \mathbf{p}_0/m \end{pmatrix} + \begin{pmatrix} \boldsymbol{\xi}(t) \\ \boldsymbol{\zeta}(t)/m \end{pmatrix} \quad (6.15)$$

$$\mathbf{p}_0 = m \left(\mathbf{v}_0 - \vec{\Omega}(\mathbf{r}_0 + \mathbf{R}) \right). \quad (6.16)$$

This translates Equation 6.13 to a new set of differential equations that are independent of the initial conditions. In the case that all parameters of rotation and gravity are constant this set can be solved exactly. Furthermore, if $\|\Omega\|$ and $\sqrt{\|\Gamma\|}$ are small compared to the transit time T (i.e. $\|\Omega\|T$, $\|\Gamma\|T^2 \ll 1$) the unknown matrices and vectors can be obtained by a series expansion in t [8]:

$$\begin{pmatrix} \vec{A}(t) & \vec{B}(t) \\ \vec{C}(t) & \vec{D}(t) \end{pmatrix} = e^{\vec{M}t} = 1 + \vec{M}t + \frac{1}{2!} \vec{M}^2 t^2 + \dots \quad (6.17)$$

$$\begin{aligned} \begin{pmatrix} \boldsymbol{\xi}(t) \\ \boldsymbol{\zeta}(t)/m \end{pmatrix} &= \vec{M}^{-1} \left(e^{\vec{M}t} - 1 \right) \begin{pmatrix} \vec{\Omega}\mathbf{R} \\ \mathbf{g} \end{pmatrix} \\ &= \left(t + \frac{1}{2!} \vec{M}t^2 + \frac{1}{3!} \vec{M}^2 t^3 + \dots \right) \begin{pmatrix} \vec{\Omega}\mathbf{R} \\ \mathbf{g} \end{pmatrix}. \end{aligned} \quad (6.18)$$

We will need these expansions to calculate the time at which the classical trajectories hit the lasers and to find simple expressions for the phase sensitivity (see Section 6.4).

6.3 Laser Interaction

The atom interferometer uses Bragg scattering (Chapter 5) to split, reflect and recombine the two paths of the interferometer and the following calculations are based on these beamsplitters. Other more complicated schemes are investigated to split the atom beam with laser beams [9]. If such a scheme is indeed used in the interferometer, the theory that is developed in this section can easily be modified.

To calculate the total interferometer phase, we need to summarize the effect of each splitter in a simple beam splitter rule that gives a relation between the wavefunction on either side of the laser sheet. For this, we will first consider two simpler examples of atom beam splitters. The kind of beam splitters that is most easily described consists of

mechanical gratings [10]. The beamsplitter rule in that case is simply that the wavefunction behind the grating is equal to the (binary) amplitude modulated initial wavefunction. The two wavefunctions are equal at the positions where the grating is open and the transmitted wave is zero where the grating is closed.

The second kind of beam splitter is a running laser wave. The atoms are (partially) excited by the laser to another internal state [11]. The atoms that are excited have absorbed a photon from the laser beam together with its associated momentum and will thus spatially separate downstream of the laser from the atoms that have not absorbed a photon. This excitation process takes a finite amount of time, which depends on the available laser power. In the limit of infinite laser intensity, however, the interaction time can be reduced to zero (so-called short pulse limit). Typical laser pulses are indeed short enough that deviations from this limit are far below the resolution of the experiment (see Chapter 7). In that case the beamsplitter rule becomes: the motional, external part of the wavefunction of the excited atoms is equal to the external wavefunction of the original atoms times the phase factor of the laser beam $\exp(ikx + i\phi_0)$. De-excitation on the other hand gives a multiplication with $\exp(-ikx - i\phi_0)$. This multiplication corresponds to adding (or subtracting) $\hbar k$ to the atoms momentum.

For Bragg scattering it is impossible to get to the limit of infinitely short interaction time, because the length of the interaction time is essential for selectivity in the transverse momentum (Chap. 5). In principle, this leads to small corrections to the (classical) position and momentum of the diffracted atom. We will ignore this however and describe the effect of Bragg scattering on the wavefunction in a similar way as scattering by a running wave: the diffracted part of the wavefunction Ψ' acquires a phase factor (see also Section 5.2)

$$\Psi'(\mathbf{r}') = \Psi_0(\mathbf{r}')e^{\pm i(\mathbf{k}_{eff} \cdot (\mathbf{r}' - \mathbf{r}_m))}, \quad (6.19)$$

where \mathbf{r}_m is the position of the mirror and \mathbf{r}' is any position on the laser interface. The effective wavevector \mathbf{k}_{eff} is the component of $2N\mathbf{k}_{laser}$ perpendicular to the mirror surface, with N the Bragg order. The sign of \mathbf{k}_{eff} is not defined for a standing wave and can be chosen freely, as long as one applies the beamsplitter phase consistently. The sign of this phase depends on the direction in which the atoms are diffracted. Diffraction into the direction along \mathbf{k}_{eff} adds the phase (+ sign), while diffraction into the opposite direction subtracts the phase (minus sign).

The rules that are stated above describe changes in the wavefunction on the laser interface. To calculate the total wavefunction in the section behind the laser we also need to know the phase gradient (momentum) transverse to the laser. This can be derived from the criterion of energy conservation. The multiplication with the laser phase factor adds a momentum component $\hbar\mathbf{k}_{eff}$. Apart from this momentum kick, there is also a small contribution \mathbf{p}_{comp} in the direction transverse to the laser to keep $|\mathbf{v}|$ constant and close the energy balance.

We can now translate the laser phase rule into a recipe that can be incorporated into the semiclassical approximation of Subsection 6.2.1. The results are given in Table 6.1.

	before	after
classical position	\mathbf{r}_{cl}	\mathbf{r}_{cl}
classical momentum	\mathbf{p}_{cl}	$\mathbf{p}_{cl} \pm \hbar \mathbf{k}_{eff} + \mathbf{p}_{comp}$
phase at classical trajectory	ϕ_0	$\phi_0 \pm (\mathbf{k}_{eff} \cdot (\mathbf{r}_{cl} - \mathbf{r}_m))$

Table 6.1: Beamsplitter rule in terms of the semiclassical approximation. The sign depends on the direction of the diffracted beam relative to \mathbf{k}_{eff} . The size of \mathbf{p}_{comp} has to be calculated from the criterion of energy conservation.

6.4 Total Phase Calculation

With the theory that is introduced in Sections 6.2 and 6.3 we can now calculate the total interferometer phase. Inertial effects are completely taken into account in the expression for the classical trajectories (Eq. 6.15). The effect of the misalignment of the lasers is twofold: it will change the laser phases (Eq. 6.19) and it will change the trajectories because of its effect on the transferred momentum. See Figure 6.2 where an exaggerated schematic with misalignments is drawn. In this example, the misalignment angle of the second laser amongst others makes the upper trajectory of the first section longer than the lower trajectory.

We will take all of the misalignment and inertial effects into account simultaneously to include all cross terms, but assume that these effects are small so that we can make a series expansion in the associated parameters. In Subsection 6.4.1 we will first derive expressions for the arrival times of the atoms and an expression for the total change in momentum by the laser beams. These expressions are then approximated by a series expansion in small parameters that represent the deviations from the perfectly aligned situation with straight trajectories. This allows us to get polynomial expressions from which we can easily obtain the dominant sensitivities. In Subsection 6.4.2 the outline of the full phase calculation is given and the results are presented in Subsection 6.4.3.

6.4.1 Approximations

The laser beams are modeled by infinite sheets that are perfectly parallel with the y-axis. The wavevector \mathbf{k} of each of the lasers lies approximately parallel to the x axis, but is rotated by small angle θ around the z axis and an angle φ in the xz plane. To second order in the angles:

$$\mathbf{k}_{eff,i} = (k_{x,i}, k_{y,i}, k_{z,i})^T = k_{eff}(1 - (\theta_i^2 + \varphi_i^2)/2, \theta_i, \varphi_i)^T \quad i = 1, 2, 3, \quad (6.20)$$

where $k_{eff} = 2N\hbar k$ and N is the Bragg diffraction order. The positions of the mirrors are the pivot points of the laser sheets. They are at a distance $x_{m,i}$ from the z-axis and positioned at $z = 0, L + \Delta L, 2L$.

With the construction of the normal vectors \mathbf{n}_i to the laser sheets we can calculate the time t_i at which the classical trajectory crosses the laser plane from the equation:

$$(\mathbf{r}_{cl}(t_i) - \mathbf{r}_{laser}) \cdot \mathbf{n}_i = 0, \quad (6.21)$$

$$\mathbf{n}_i = (\mathbf{k}_{eff,i} \times \mathbf{e}_y) / k_{eff,i}, \quad (6.22)$$

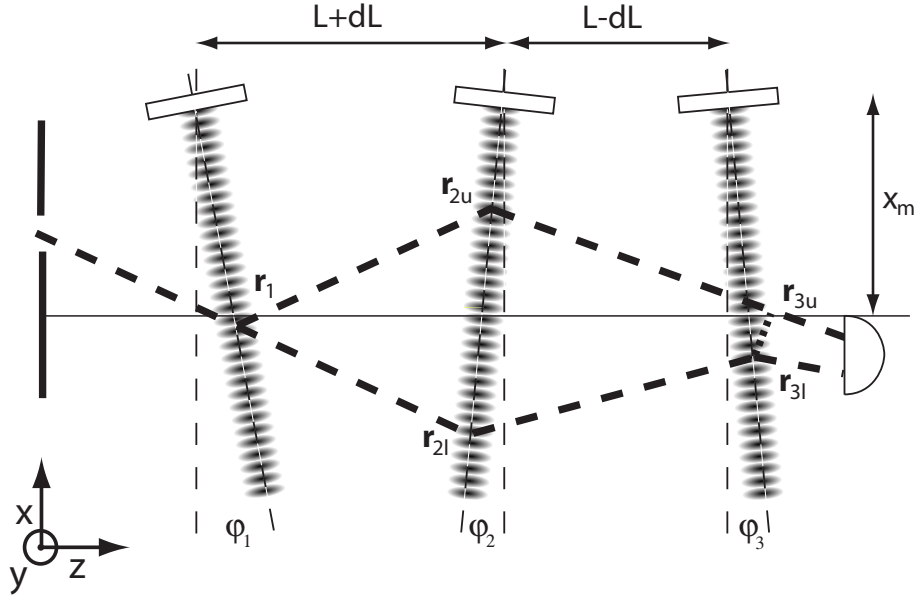


Figure 6.2: Highly exaggerated representation of the trajectories when the lasers are misaligned. The classical trajectories hit the lasers at the indicated positions $\mathbf{r}_1, \mathbf{r}_{2u}, \mathbf{r}_{2l}$ and \mathbf{r}_{3l} . The end of the upper path \mathbf{r}_{3u} is the point of the upper trajectory that lies closest to \mathbf{r}_{3l} . The interferometer phase is the difference in accumulated phase between the paths $\mathbf{r}_1 - \mathbf{r}_{2u} - \mathbf{r}_{3u}$ and $\mathbf{r}_1 - \mathbf{r}_{2l} - \mathbf{r}_{3l}$.

where \mathbf{r}_{laser} can be any fixed point on the laser plane (usually the position of the mirror \mathbf{r}_m is taken). We will approximate the classical trajectories by parabolas. In terms of the dummy variables \mathbf{r}_0 , \mathbf{v}_0 and \mathbf{a}_0 :

$$\mathbf{r}_{cl}(t) = \mathbf{r}_0 + \mathbf{v}_0 t + \mathbf{a}_0 t^2 / 2. \quad (6.23)$$

These dummy variables will be different for each section of the interferometer. All effects from gravity and rotation on the trajectory are temporarily summarized in the vectors \mathbf{v}_0 and \mathbf{a}_0 . In the full calculation these will be replaced by their full expression that follows from Equation 6.15 (in combination with Eq. 6.17 and Eq. 6.18). We assume that the acceleration (gravity, rotation) is small enough to give only small deviation from a straight line. We then obtain the following approximate solution to Equation 6.21:

$$\begin{aligned} t_i &= \frac{-(\mathbf{r}_0 - \mathbf{r}_{laser}) \cdot \mathbf{n}_i}{\mathbf{v}_0 \cdot \mathbf{n}_i} - \frac{\mathbf{a}_0 \cdot \mathbf{n}_i ((\mathbf{r}_0 - \mathbf{r}_{laser}) \cdot \mathbf{n}_i)^2}{2(\mathbf{v}_0 \cdot \mathbf{n}_i)^2} + \dots \\ &\approx -\frac{(\mathbf{r}_0 - \mathbf{r}_{laser}) \cdot \mathbf{n}_i}{v_{z0}} \left(2 - \frac{\mathbf{v}_0 \cdot \mathbf{n}_i}{v_{z0}} \right) \\ &\quad - \frac{\mathbf{a}_0 \cdot \mathbf{n}_i ((\mathbf{r}_0 - \mathbf{r}_{laser}) \cdot \mathbf{n}_i)^2}{2v_{z0}^3} \left(4 - 3 \frac{\mathbf{v}_0 \cdot \mathbf{n}_i}{v_{z0}} \right) + \dots, \end{aligned} \quad (6.24)$$

where we made an extra expansion of the velocity terms $\mathbf{v}_0 \cdot \mathbf{n}_i$ around the initial axial velocity v_{z0} .

In principle, one has to calculate the phase integral over the full path from the aperture to the detector. To limit the computational work, however, only the phase evolution in between the standing light waves was calculated. Obviously, there is no harm in omitting the section before the first atom beam splitter. The omission of the last section before the detector is not trivial as the two trajectories have a slightly different position and momentum, leading to a slightly different phase. Numerical calculations, however, show that this difference is very small and that the detector is positioned close enough to the final beamsplitter¹ that the phase contribution of this final section can be neglected. The interferometer phase difference between the two paths then no longer changes when the “lower path” has been diffracted by the last laser (at the position \mathbf{r}_{3l}). The “upper beam” is not diffracted by the last laser and does not acquire an extra phase when it passes through. Therefore, regardless of whether this path hits the last laser before or after the lower path, the total phase difference is fixed as soon as the lower path arrives at the last laser. The phase difference between the two paths at this point is equal to the interferometer phase.

The time associated with the closest point on the upper path to \mathbf{r}_{3l} (needed for Eq. 6.6) has to be calculated with Equation 6.7. In terms of the initial position, velocity and acceleration after the second laser we can approximate the associated arrival time to first order in the acceleration by

$$t_{3u} \approx -\frac{c_3}{c_2} - \frac{c_1 c_3^2}{c_2^3} + \dots \approx \frac{c_3}{v_{z0}^2} \left(2 + \frac{c_2}{v_{z0}^2}\right) + \frac{c_1 c_3^2}{v_{z0}^6} \left(4 + \frac{3c_2}{v_{z0}^2}\right) + \dots \quad (6.25)$$

$$c_1 = -\frac{3}{2} \mathbf{a}_0 \cdot \mathbf{v}_0 \quad (6.26)$$

$$c_2 = (\mathbf{r}_{3l} - \mathbf{r}_0) \cdot \mathbf{a}_0 - v_0^2 \quad (\approx -v_{z0}^2) \quad (6.27)$$

$$c_3 = (\mathbf{r}_{3l} - \mathbf{r}_0) \cdot \mathbf{v}_0. \quad (6.28)$$

The final approximation that we have to make is on the velocity change on diffraction by the laser beams. The atoms acquire a velocity increase of $\Delta \mathbf{v} = \hbar \mathbf{k}_{eff} / m$ along the laser, but the velocity perpendicular to the laser plane (along \mathbf{n}) also changes with an amount v_{comp} because of energy conservation. In terms of the initial velocity \mathbf{v}_i the velocity of the atom \mathbf{v}_f directly after the laser beam becomes:

$$\begin{aligned} \mathbf{v}_f &= \mathbf{v}_i + \Delta \mathbf{v} + v_{comp} \mathbf{n} \quad (6.29) \\ v_{comp} &= -\mathbf{v}_i \cdot \mathbf{n} + \sqrt{(\mathbf{v}_i \cdot \mathbf{n})^2 - \Delta \mathbf{v}^2 - 2\Delta \mathbf{v} \cdot \mathbf{v}_i} \\ &\approx -\frac{\Delta \mathbf{v}^2 + 2\mathbf{v}_i \cdot \Delta \mathbf{v}}{2\mathbf{v}_i \cdot \mathbf{n}} \\ &\approx -\left(\frac{\Delta \mathbf{v}^2 + 2\mathbf{v}_i \cdot \Delta \mathbf{v}}{2v_{z0}}\right) \left(2 - \frac{\mathbf{v}_i \cdot \mathbf{n}}{v_{z0}}\right). \quad (6.30) \end{aligned}$$

As long as the position of the atom does not change during the interaction with the laser, this calculation can also be performed in terms of the momentum \mathbf{p} . We use the velocity here instead, because the lasers are aligned to be almost perpendicular to the atom beam ($\mathbf{v} \cdot \mathbf{k}_{laser}$ is small), while the momentum (Eq. 6.16) could have a large component along the laser.

¹The detector is however placed far enough to have a spatial separation between the two output ports.

6.4.2 Calculations Outline

Using the approximation of Equations 6.24, 6.25 and 6.29 and the series expansion of the classical trajectory, we can now calculate the total interferometer phase. For this we use the following recipe:

1. **Full lower trajectory:** the lower path starts at \mathbf{r}_1 (which lies on the first laser plane) with velocity \mathbf{v}_1 . Using the series expansion of Equation 6.15 in t we calculate the acceleration and then the arrival time t_{2l} at the second laser from Eq. 6.24 with the position $\mathbf{r}_{2l} = \mathbf{r}_{cl}(t_{2l})$ and the velocity. The second section of the lower path starts at \mathbf{r}_{2l} , but with an added velocity $+\hbar\mathbf{k}_{eff,2}/m$ (plus compensation, Eq. 6.29). Then, like in the first section, we calculate the acceleration and velocity at this position and from these the arrival time t_{3l} at the third laser. The position on the trajectory at this time is called \mathbf{r}_{3l} .
2. **Full upper trajectory:** the upper path also starts at \mathbf{r}_1 but with velocity $\mathbf{v}_1 + \hbar\mathbf{k}_{eff,1}/m + \mathbf{v}_{comp}$. Again, the initial acceleration is calculated, followed by the arrival time t_{2u} at the second laser and the position \mathbf{r}_{2u} at this time. Here the velocity is changed by $-\hbar\mathbf{k}_{eff,2}/m + \text{compensation}$. The final position \mathbf{r}_{3u} of the upper path is given by the time t_{3u} that is obtained from Equation 6.25.
3. **Propagation Phase:** From the classical trajectories we calculate the four integral contributions to the interferometer phase (see Equation 6.6)

$$\begin{aligned} \phi_{prop} = & \frac{1}{\hbar} \left(\int_0^{t_{2u}} \mathbf{p}_{2u}(t) \cdot \mathbf{v}_{2u}(t) dt + \int_0^{t_{3u}} \mathbf{p}_{3u}(t) \cdot \mathbf{v}_{3u}(t) dt \right. \\ & \left. - \int_0^{t_{2l}} \mathbf{p}_{2l}(t) \cdot \mathbf{v}_{2l}(t) dt - \int_0^{t_{3l}} \mathbf{p}_{3l}(t) \cdot \mathbf{v}_{3l}(t) dt \right). \end{aligned} \quad (6.31)$$

(the vectors $\mathbf{p}_i(t)$ and $\mathbf{v}_i(t)$ indicate the classical momentum and velocity along the trajectory, while \mathbf{p}_i and \mathbf{v}_i denote their values at the end of each section).

4. **Laser Phase:** The classical positions at the laser planes give the contribution of the imprint of the laser phase:

$$\begin{aligned} \phi_{laser} = & \mathbf{k}_{eff,1} \cdot (\mathbf{r}_1 - \mathbf{r}_{m1}) - \mathbf{k}_{eff,2} \cdot (\mathbf{r}_{2u} - \mathbf{r}_{m2}) \\ & - \mathbf{k}_{eff,2} \cdot (\mathbf{r}_{2l} - \mathbf{r}_{m2}) + \mathbf{k}_{eff,3} \cdot (\mathbf{r}_{3l} - \mathbf{r}_{m3}). \end{aligned} \quad (6.32)$$

5. **Separation Phase:** The final contribution to the total interferometer phase stems from the fact that the two classical paths do not exactly overlap and is given to first order in the separation by

$$\phi_{sep} = (\mathbf{r}_{3l} - \mathbf{r}_{3u}) \cdot \mathbf{p}_{3u} / \hbar. \quad (6.33)$$

6. **Total Interferometer Phase:** The total phase difference between the two paths that is seen in the detector signal is

$$\phi_{tot} = \phi_{prop} + \phi_{laser} + \phi_{sep}. \quad (6.34)$$

By using the discussed approximations, the obtained interferometer phase is polynomial in all parameters. We then expand the expression for the phase into one large summation and evaluate each of the terms separately for typical values of the parameters. This allows us to easily obtain the strongest dependencies. The results are given in the next subsection.

6.4.3 Results

The expression for the total interferometer phase was calculated algebraically on a computer using Maple software following the recipe that was described in the previous subsection. The total expression for this phase was expanded into a sum of terms and all of these terms were evaluated with typical values for the parameters (see Table 6.2). For parameters that have an average value of zero, like the misalignment angles, the maximum value within the uncertainty interval was taken. Then the phase terms were sorted in order of numerical value and stored in a list. The largest few terms of this list are given in Table 6.3 in the column “piecemeal max.”, where similar terms are combined again for clarity. Note that the numerical value in this column does not give the numerical value of the total, combined phase term, but rather the maximum of the summed components. One could also say that we estimated, e.g, the difference between angles with the value of the maximum individual angle. This number gives a clear ordering of the parameters that have the largest effect on the interferometer phase. For example, the table clearly shows that the (relative) positions of the mirrors have to be extremely stable.

For the numerical values in this column (“piecemeal max.”), we only considered the gravity and the rotation of the earth and did not account for additional potential fields or e.g, the rotation of the setup relative to the laboratory. The gravitational acceleration \mathbf{g} ($g = 9.8 \text{ m/s}^2$) lies exactly along the y-axis and the interferometer plane is almost perpendicular to this with small laser angles $\theta_i=1 \text{ mrad}$ for misalignment. The angles φ_i of the lasers in the interferometer (xz) plane can be aligned more accurately by looking at the scattering efficiency. We took $\varphi_i = 0.2 \text{ mrad}$ which corresponds to an error of 0.5 photon recoil in the velocity along the laser beam.

The three mirrors are placed at $z = 0$, $z = L + \Delta L = 155 \text{ mm}$ and $z = 2L = 300 \text{ mm}$. If the laser angles were perfectly aligned these values would be the same for the positions where the atoms interact with the laser. However, because of the angles and the separation between the mirrors and the atom beam, the z-coordinate of the interaction points is slightly different. The first interaction point, where the actual interferometer starts, is given in terms of the atoms offset from the z-axis

$$\mathbf{r}_1 = (x_1, y_1, \varphi_1(x_1 - x_{m1}))^T = (100, 100, 40)^T \mu\text{m}. \quad (6.35)$$

The origin of the coordinate system was (thus) chosen at the nominal position where the atom beam intersects the first laser beam. The considered atoms have an axial velocity of 250 m/s and an angle that is close to the Bragg condition, but have a mismatch of a fraction $\Delta N = 0.1$ of the photon recoil velocity (corresponding to 9 mm/s) such that:

$$\mathbf{v}_1 = (v_{x0}, v_{y0}, v_{z0})^T = (-0.47, 0.025, 250)^T \text{ m/s}. \quad (6.36)$$

The calculations are for fifth order Bragg scattering $N = 5$.

The considered rotation is that of the earth with radius $R = 6.7 \times 10^6$ m (we take \mathbf{R} along the y-axis). Because the exact orientation of the setup is unknown, the three components of $\boldsymbol{\Omega}$ were all taken equal $\Omega_x = \Omega_y = \Omega_z = 7 \times 10^{-5} \text{ s}^{-1}$. In reality, the rotational components will thus be smaller. For example, in the case that the axis of the interferometer is aligned perfectly from north to south, Ω_x is zero. For completeness, we also included the gradient in \mathbf{g} for a spherically symmetric earth with $2\Gamma_{xx} = 2\Gamma_{zz} = -\Gamma_{yy} = 2g_y/R = 3 \times 10^{-6} \text{ s}^{-2}$ and all other components zero. The effect of this gradient is too small, however, and does not appear in the list.

A few terms in Table 6.3 can be identified with traditional phases, like the Sagnac phase shift and the acceleration terms. The term that is commented by the time integral, can be easily explained with the difference in kinetic energy (of the motion along the lasers) integrated over the transit time. The difference in this kinetic energy is caused by the slight misalignment $\Delta N v_{rec}$. In a perfectly symmetric interferometer this energy difference would be compensated in the two sections of the interferometer. The difference in length $2\Delta L$, however, breaks the symmetry and leaves the phase that is indicated in Table 6.3. This effect was also found in [4].

The largest contribution to the phase by far is the well known contribution of the phase of the standing waves. In this case we estimated the value of this term solely from the distance of the mirrors from the atoms (0.2 m). This is the only term in the list where the numerical value of the individual terms in the column “piecemeal max.” can be quite misleading. The three mirrors are placed at approximately the same distance and the three terms will cancel each other for the most part. The actual phase that remains is then orders of magnitude smaller than the value that is given here. However, even with this refinement, the combined phase term often is still much larger than the other phases. Because of the high sensitivity and because it can be adjusted very easily (e.g, by moving a mirror), this effective laser phase is sometimes used to mimic or compensate for other phase terms [12].

It is clear from the list that many of the phase terms cancel each other. To get an idea of the extent of this cancelation, the column “ideal mean” was added in which the total phase contribution of that row is given for a perfect alignment of the lasers. We see that most of the phase terms disappear and only the Sagnac phase and the centrifugal acceleration remain. The gravity terms also disappears, because in the ideal case of this configuration, gravity is perpendicular to the interferometer plane.

In this work, however, we are interested in misalignment effects and specifically the resulting loss of contrast. Loss of contrast is caused by a variation of phase, either from atom to atom or in time. If all parameters are constant (in time), the quality of the interference signal is determined by the statistical spread in atomic parameters. The fourth column of Table 6.3 gives the RMS phase spread of the interferometer phase when the error on the atomic parameters in Table 6.2 are taken as an RMS spread and the alignment of the lasers is the worst possible within the given error intervals. It is then assumed that the temporal fluctuations of these parameters are much smaller than the alignment error and do not contribute to the phase spread. Some phase terms are independent of atomic parameters and therefore do not have an (atomic) phase spread. Notably, this is the case for the large laser phase term. Because of the magnitude of this term, however, in practice

we cannot neglect the temporal variations in the relative mirror distance and we will have to reckon with the associated phase fluctuations

$$\sigma_\phi = 2Nk_{laser} \sigma_{\Delta x}, \quad (6.37)$$

$$\sigma_{\Delta x} \equiv \sqrt{\langle (x_{m1} + x_{m3} - 2x_{m2})^2 \rangle}. \quad (6.38)$$

The spread of many other terms is the same as the value in the second column. Only terms with v_{z0} as the only atomic parameter have a phase spread that is smaller than the value in the second column, because this is the only atomic parameter with a relatively narrow distribution ($\sigma_v/\bar{v} \approx 1\%$) that is not centered around zero. The largest contribution to the atomic phase spread comes from the second term in the list. To reduce the phase spread the alignment will have to be considerably better than the value that was used for this table. We will get back to this in more detail in the next section.

To check the validity of this list, the same calculations were performed fully numerically without the approximations of Subsection 6.4.1. The trajectories were still approximated by parabolas, but the arrival times were from a full numerical solution of Equations 6.7 and 6.21. We found that the difference between the full numerically calculated interferometer phase and the result with the approximations differed at most by 4 mrad. We can thus conclude that the series expansions are indeed valid for the numerical ranges of Table 6.2.

An extra potential can be added to the calculations by changing the numerical values of \mathbf{g} and $\vec{\Gamma}$. Some of the largest contributions to the interferometer phase that arise are given in Table 6.4. Closer inspection of this list reveals that most of the phase terms can be written in terms of the gradient along the lasers. There are only two terms that involve the potential gradient along the beam axis. These terms are introduced by the requirement of energy conservation on diffraction by the lasers and are often very small. The only term without perturbation effects is the top entry, which is the equivalent of the acceleration term kgT^2 in the treatment of time-based interferometers.

6.5 Design Considerations

Using the results of the previous section, we can now set up the specifications of the interferometer. With respect to the phase, there are two parameters that are of importance: the phase stability and the phase spread. The basic difference between these two is the time scale of the fluctuations with respect to the total integration (measurement) time. The phase spread describes the variations in phase that exist between atoms with different properties, such as the longitudinal velocity, and the variations that are caused by fast temporal fluctuations in the interferometer parameters. The phase stability relates to fluctuations that are slow compared to the measurement time. Both of these effects influence the accuracy of a phase measurement from the interference signal. The phase spread will give an average signal over a range of signals with different phases. This reduces the fringe contrast and the sensitivity and thereby the accuracy of the measurement. The phase stability influences the accuracy through the uncertainty in the reference phase.

In the following we consider only the phase spread: we will assume that all fluctuations are much faster than the measuring time. This is a reasonable assumption, because the

description	expression	value
laser angle in xz plane	$\varphi_1 = \varphi_2 = \varphi_3$	0 ± 0.2 mrad
laser angle around z-axis	$\theta_1 = \theta_2 = \theta_3$	0 ± 1 mrad
laser separation (on mirrors)	L	0.15 ± 0 m
error in z-position mirror 2	ΔL	0 ± 5 mm
mirror distance from z-axis	$x_{m1} = x_{m2} = x_{m3}$	200 ± 1 mm
gravity	$g_x = g_z$	0 ± 0
	g_y	-9.8 ± 0 m/s ²
rotation	$\Omega_x = \Omega_y = \Omega_z$	$(7.3 \pm 0) \times 10^{-5}$ s ⁻¹
center of rotation	$R_x = R_z$	0 ± 0
	R_y	$(6.7 \pm 0) \times 10^6$ m
Bragg order	N	5 ± 0
error in transverse velocity	ΔN	0 ± 0.1
atomic mass	m	$(6.6 \pm 0) \times 10^{-27}$ kg
laser wavenumber	$k = 2\pi/\lambda_{laser}$	$(5.8 \pm 0) \times 10^6$ m ⁻¹
(single photon) recoil velocity	$v_{rec} = \hbar k/m$	92 ± 0 mm/s
position of first laser	z_1	0 ± 0
transverse position at first laser	$x_1 = y_1$	0 ± 0.1 mm
velocity at first laser	$v_{x0} = -(N + \Delta N)v_{rec}$	
	v_{y0}	0 ± 25 mm/s
	v_{z0}	250 ± 2 m/s

Table 6.2: Numerical values that are used in Table 6.3. The errors on the atomic parameters indicate the RMS spread. The values of the laser parameters indicate the ideal setting \pm the maximum alignment error.

limited beam flux sets the minimum integration time to at least a few seconds so that all fluctuations with a frequency that is larger than 1 Hz are indeed averaged out. Furthermore, variations that are much slower than the integration time can be eliminated by differential measurements. In that case the stability is not a main concern and we only need to set a limit to the phase spread. The requirement is then simply that the phase spread is not large enough to significantly reduce the contrast of the interference signal.

A quantitative measure of the contrast is called the visibility V . This is the ratio of the amplitude of the interference fringes to the offset in the detector signal, or in terms of the maximum and minimum detector signal (see Fig. 6.3):

$$V = \frac{I_{max} - I_{min}}{I_{max} + I_{min}}. \quad (6.39)$$

The phase accuracy is determined by the shot-noise limit: [13]

$$\sigma_{\phi, meas} = \frac{\sigma_{Ncounts}}{dNcounts/d\phi} = \frac{1}{V\sqrt{Ncounts}}. \quad (6.40)$$

In an ideal interferometer ($V = 1$), the RMS deviation in the measured phase thus decreases with the number of measured atoms N_{counts} and can be made arbitrarily small by measuring

expression	piecemeal max.	ideal mean	max. atomic spread	
$-k_{eff}(x_{m1} + x_{m3} - 2x_{m2})$	2×10^7	0	0.	laser phases
$-2k_{eff}v_{rec} \Delta N \Delta L/v_{z0}$	22	0	22.	$\int \Delta E_{kin,x} dt/\hbar$
$k_{eff}y_1(\theta_1 + \theta_3 - 2\theta_2)$	12	0	12.	
$-k_{eff}(\theta_1^2 x_{m1} + \theta_3^2 x_{m3} - 2\theta_2^2 x_{m2})/2$	12	0	0.	
$2k_{eff}v_{y0}(\theta_3 - \theta_2)L/v_{z0}$	1.7	0	1.7	
$-2k_{eff}\Omega_y L^2/v_{z0}$	0.7	0.7	0.007	Sagnac phase
$-k_{eff}\Omega_x \Omega_y R L^2/v_{z0}^2$	0.7	0.7	0.01	centrifugal acceleration
$-k_{eff}(\varphi_1^2 x_{m1} + \varphi_3^2 x_{m3} - 2\varphi_2^2 x_{m2})/2$	0.5	0	0.	
$k_{eff}g_y(2\theta_3 - \theta_2)L^2/v_{z0}^2$	0.4	0	0.008	gravity
$k_{eff}v_{rec} \Delta N (\varphi_1 x_{m1} + \varphi_3 x_{m3} - 2\varphi_2 x_{m2})/v_{z0}$	0.2	0	0.2	
$\hbar k_{eff}^2(2\theta_1\theta_2 - 2\theta_2^2 + \theta_3\theta_2 - \theta_1^2)L/v_{z0}m$	0.07	0	0.0007	
$2k_{eff}\theta_2 v_{y0} \Delta L/v_{z0}$	0.06	0	0.06	
$-4k_{eff}\Omega_y L \Delta L/v_{z0}$	0.05	0	0.0005	
$-2k_{eff}\Omega_x \Omega_y R L \Delta L/v_{z0}^2$	0.05	0	0.001	
$2k_{eff}\theta_2 g_y L \Delta L/v_{z0}^2$	0.05	0	0.001	
$-k_{eff}x_1(\theta_1^2 + \theta_3^2 - 2\theta_2^2)/2$	0.006	0	0.006	
...				

Table 6.3: List of contributions to the interferometer phase in order of estimated size. The value in the column “piecemeal max.” indicates the estimated maximum value of the individual terms using the numerical values of the parameters from Table 6.2. The third column gives the mean value of the combined terms in the case of perfect laser alignment. The column “max. atomic spread” gives the RMS phase spread that is caused by the statistical spread on the atomic parameters in the case of worst optical alignment (within error).

effects from added potential
$k_{eff}g_x L^2/v_{z0}^2$
$k_{eff}g_y(2\theta_3 - \theta_2)L^2/v_{z0}^2$
$2k_{eff}g_x L \Delta L/v_{z0}^2$
$k_{eff}v_{rec}g_z \Delta N L^2/v_{z0}^3$
$k_{eff}(\Gamma_{xx}x_1 + \Gamma_{xy}y_1)L^2/v_{z0}^2$
$2k_{eff}\Gamma_{xx}x_1(\varphi_2 x_{m2} - \varphi_3 x_{m3})L/v_{z0}^2$
$k_{eff}\Gamma_{xy}y_1(\varphi_2 x_{m2} - \varphi_3 x_{m3})L/v_{z0}^2$
$k_{eff}v_{rec} \Delta N(\Gamma_{yz}y_1 + \Gamma_{zx}x_1)L^2/2v_{z0}^3$
...

Table 6.4: Possible extra contributions to the phase from a potential

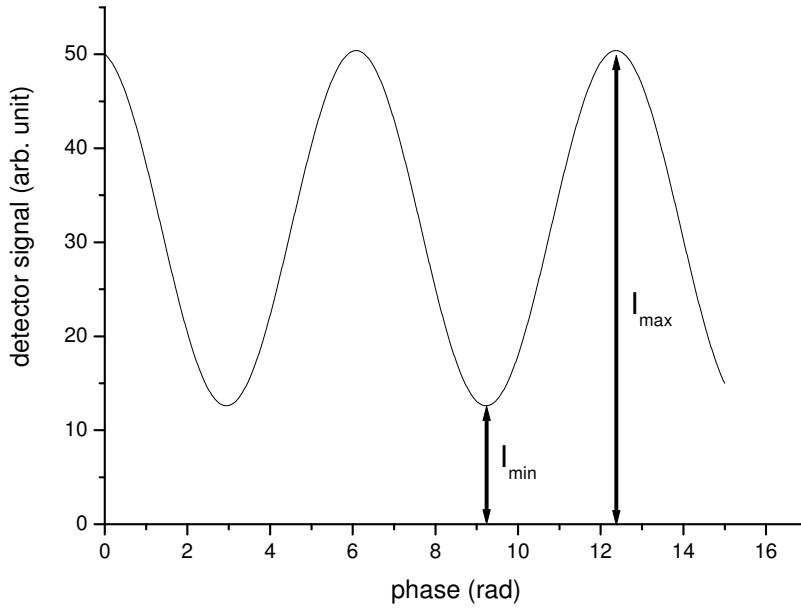


Figure 6.3: Example of interference fringes with an indication of the maximum and the minimum detector signal.

ever more atoms. In a non-ideal interferometer the visibility is smaller than unity and the error on the measured phase is larger. In the following, we will demand a maximum phase spread of $\sigma_{\phi max} = 0.1$ rad, at which the visibility is still 98% and the phase accuracy is thus hardly affected.

The main problem in atom interferometers is the relative motion of the mirrors. From the top entry of Table 6.3 we obtain the requirement that the three mirrors have to be stable within

$$\sigma_{\Delta x} < \frac{\sigma_{\phi max}}{k_{eff}} = 1.7 \times 10^{-9} \text{ m}, \quad (6.41)$$

at fifth order Bragg scattering. This criterion can be relaxed slightly with a factor of 5 by taking first order Bragg scattering, but even then this stability is not easy to achieve. The setup will have to be carefully isolated from vibrations and the mirrors may have to be actively locked with a feedback loop. For this purpose, an optical interferometer has already been implemented parallel to the atom interferometer to measure and actively stabilize the relative positioning of the mirrors [14, 15].

Except for an actual movement of the mirrors, the effective phase of the standing wave can also be influenced by fluctuations in the laser frequency and wavelength. The required stability of the laser frequency (for $N=5$) is

$$\sigma_{\omega, laser} < \frac{c \sigma_{\phi max}}{2N x_m} = 2.4 \times 10^6 (2\pi) \text{ Hz}. \quad (6.42)$$

Note that we can not assume that the laser frequency is the same for all three standing waves, because the frequency can change as the atom moves through the interferometer.

This stability is readily obtained by most lasers. Fluctuations in the refractive index on the optical path between the atom beam and the mirrors, e.g, by air flows, have the same effect as a fluctuation of the laser frequency. These often have an even larger impact than changes in the laser frequency and careful shielding is necessary to avoid such air flows.

The second source of concern in an atom interferometer is the angle of the laser mirrors. The exact criterion on these angles is more difficult to determine than the criterion on the position, because the angles of the lasers affect more than just the interferometer phase. The angle of the lasers directly translates to the angle of the atom beam. At the output of the interferometer the two beams have a momentum difference $\Delta\mathbf{p} = \mathbf{p}_{3u} - \mathbf{p}_{3l} \approx \hbar(\mathbf{k}_{eff,1} + \mathbf{k}_{eff,3} - 2\mathbf{k}_{eff,2})$. This momentum difference between the two beams sets two criteria. Firstly, the angle between the two beams may not be so large that they do not overlap anymore. To first order in the laser angles we get

$$(\theta_1 + \theta_3 - 2\theta_2) < \frac{\Delta x_{det} v_{z0}}{2N v_{rec} z_{det}} = 13 \text{ mrad} \quad (6.43)$$

for a detector distance z_{det} of 2 m and a maximum separation of 100 μm , which is approximately the atom beam size at the detector. Secondly, the difference in the (transverse component of the) wavevector introduces spatial fringes on the detector. To avoid that these fringes reduce the contrast of the interferometer, the wavelength of these fringes along the detector surface must be larger than the detector area (or the detector resolution of the position sensitive detector). Again to first order in the laser angles we obtain

$$(\theta_1 + \theta_3 - 2\theta_2) < \frac{1}{2N k_{laser} w_{det}} = 0.17 \text{ mrad} \quad (6.44)$$

for a detector resolution w_{det} of 100 μm .

A third criterion for the laser angles stems from the tolerance on Bragg scattering (Chap. 5). This only has a minute effect on the angles θ_i , but the angles φ_i have to be aligned (to the atom beam) with an accuracy that is better than 0.4 mrad.

As a last consideration for the laser angles we look at the contribution to the interferometer phase. We find the most stringent restrictions from the terms in Table 6.3 that have the largest phase spread. For the laser angles we get

$$\theta_1 + \theta_3 - 2\theta_2 < \frac{\sigma_{\phi max}}{k_{eff} \sigma_{y1}} = 17 \mu\text{rad} \quad (6.45)$$

if the atom beam is spatially completely incoherent over the entrance aperture and

$$\theta_3 - \theta_2 < \frac{\sigma_{\phi max} v_{z0}}{2k_{eff} L \sigma_{vy0}} = 57 \mu\text{rad} \quad (6.46)$$

if the beam is spatially fully coherent ($\sigma_{y1} = 0$). The angles in the interferometer plane must fulfill the following relation

$$\varphi_1 + \varphi_3 - 2\varphi_2 \leq \frac{\sigma_{\phi max} v_{z0}}{k_{eff} v_{rec} \Delta N x_m} = 0.23 \text{ mrad}. \quad (6.47)$$

Then if we compare all the requirements on the laser angles we can summarize them by taking the strongest requirement. Applying the requirements for differences on the angles separately we get the limits that are given in Table 6.5.

	max.
$\sigma_{\Delta x}$	1.7 nm
ϕ	0.23 mrad
θ	17 μ rad
ΔL	23 μ m

Table 6.5: Maximum errors of the laser parameters.

The last parameter that involves the positioning of the laser mirrors is the difference in length of the interferometer sections $2\Delta L$ which affects both the overlap at the end of the detector and the atomic phase spread. A straight forward calculation that arises from the requirement that the two atom beams at the end of the interferometer may not be separated by more than their diameter gives

$$\Delta L < \frac{\Delta x_{det} v_{z0} m}{2\hbar k_{eff}} = 14 \text{ mm.} \quad (6.48)$$

The second term in Table 6.3 gives

$$\Delta L < \frac{\sigma_{\phi max} v_{z0}}{2k_{eff} v_{rec} \Delta N} = 23 \mu\text{m.} \quad (6.49)$$

The demands on the symmetry of the setup thus are severe and the length of the two sections should be set very carefully.

Lastly, we will consider the external potential that is applied to the interferometer. For neutral atoms the most common source of potential energy is caused by an external magnetic field $V(\mathbf{x}) = -\boldsymbol{\mu} \cdot \mathbf{B}(\mathbf{x}) = m_i \mu_B g_i B(\mathbf{x})$, where $\boldsymbol{\mu}$ is the magnetic moment, g_i the Landé factor, m_i is the magnetic quantum number relative to the magnetic field and μ_B is the Bohr magneton. The only term in Table 6.4 without any perturbation effects is the top term and this will therefore usually be the dominant contribution to the phase. Using this expression we find an upper limit for the allowed field gradient along the lasers

$$\frac{dB}{dx} \leq \frac{m \sigma_{\phi max} v_{z0}^3}{m_j \mu_B g_j k_{eff} L^2 \sigma v_{z0}} = 1.8 \times 10^{-4} \text{ T/m} \quad (6.50)$$

for atoms with $m_j = 1$. The sensitivity to magnetic field gradients is thus quite high and (stray) fields have to be avoided. A possibility to reduce the sensitivity to magnetic fields is to prepare the atom beam for $m_j = 0$. In fact, without any additional shielding from stray magnetic fields this seems essential.

6.6 Conclusion

In this chapter we calculated the phase sensitivity of a static spatial atom interferometer. Under the assumption that the classical atomic trajectories are approximately straight lines, we were able to make a series expansion of the interferometer phase and find the dominant contributions. Among the largest few sensitivity terms are traditional phases

like the Sagnac phase and the gravitation phase. There are, however, also a few terms that arise from imperfect alignment of the lasers that are usually ignored. It was shown that the phase contribution from these terms can easily be larger than the traditional phases and one has to take special care that these effects do not wash out the interference signal. Maximum values were found for the position and angle of the mirrors of the standing light waves. The most restrictive are on the relative transverse position of the laser mirrors $\sigma_{\Delta x} \leq 2$ nm, the angle of the standing light waves with the interferometer plane $\theta < 17 \mu\text{rad}$ and the difference in length of the two interferometer sections $\Delta L < 23 \mu\text{m}$. The maximum allowed magnetic field gradient is $dB/dx < 2$ G/m which implies that without any additional shielding, interference fringes will only be visible for atoms with $m_j = 0$.

References

- [1] John F. Clauser, *Physica* **151B**, 262 (1988).
- [2] M. Kasevich and S. Chu, *Appl. Phys. B* **54**, 321 (1992).
- [3] A. Miffre, M. Jacquy, M. Büchner, G. Tréneç and J. Vigué, *Appl. Phys. B* **84** 617 (2006).
- [4] C. Champenois, M. Büchner and J. Vigué, *Eur. Phys. J. D* **5** 363 (1999).
- [5] Victor P. Maslov, *The Complex WKB Method for Nonlinear Equations 1*, (Birkhäuser, Basel, 1994).
- [6] K. Bongs, R. Launay, M.A. Kasevich, *Appl. Phys. B* **84** 599 (2006).
- [7] Pippa Storey and Claude Cohen-Tannoudji, *J. Phys. II* **4** 1999 (1994).
- [8] Bordé Ch. J., *J. Opt. B: Quant. Semiclass. Opt.* **5**, S199 (2003).
- [9] W. van Dijk, *Quasi-Bragg Scattering*, internal report, Eindhoven University of Technology (2004).
- [10] J. Schmiedmayer *et al* in *Atom Interferometry*, (Academic Press, New York, 1997) (ed P. Berman), p1.
- [11] B. Young *et al* in *Atom Interferometry*, (Academic Press, New York, 1997) (ed P. Berman), p366.
- [12] T.L. Gustavson, A. Landragin and M.A. Kasevich, *Class. Quantum Grav.* **17** 2385 (2000).
- [13] Marlan O. Scully and Jonathan P. Dowling, *Phys. Rev. A* **48** 3186 (1993).
- [14] David M. Giltner, Roger W. McGowan and Siu Au Lee, *Phys. Rev. Lett* **75** 2638 (1995).
- [15] A.C.H. Meesters, *Assessment of Very Large Atom Interferometers*, internal report, Eindhoven University of Technology (2003)

Chapter 7

Laser Pulse Length Effects in Time-Based Atom Interferometers

7.1 Introduction

We saw in the previous chapter that atom interferometers are very sensitive to a great number of effects such as gravity and rotation. Atom interferometers are therefore ideal setups for precision measurements of these effects. The accuracy of a measurement is limited by the relatively small flux of atoms and technical noise. As technical developments progress, these sources of noise are ever further reduced and the accuracy increased. The accuracy of a measurement, however, is also limited by the quality of the model that is used to interpret the signal. Usually, simple expressions are used such as the Sagnac phase. These expressions only contain a few parameters that have to be known, which makes it relatively easy to do precision measurements, but they rely on several approximations. Although these formulas work very well [1, 2], there is bound to be some limit at which they are no longer valid. As interferometric measurements often aim for extremes in sensitivity and accuracy, it is important to investigate this limit and the range beyond. It is the goal of this chapter to take the calculations one step further and find out what the validity range of these traditional phase expressions is. Specifically, we will focus on the effect of the finite length of the laser pulses in time based interferometers which is usually neglected. The calculations are performed in the context of an interferometer that is being constructed at Stanford to test the equivalence principle to a relative accuracy of 10^{-15} . They can, however, readily be applied to other atom interferometers.

We will start with a description of the experiment in Section 7.2, after which we introduce all effects that we will consider by introducing the Hamiltonian. The considered interferometer is time-based in which spatially the laser beams overlap fully with the atoms and are turned on for a few short pulses. The evolution between pulses can be solved exactly. In Section 7.3 the Hamiltonian is therefore transformed to a reference frame that moves along with the free propagation of the atoms in which nothing changes between the laser pulses. The evolution during the laser pulses can not be solved exactly, but in Section 7.4 we assume that the pulses are sufficiently short that we can use a series expansion in the pulse length. Then in Section 7.5 we combine the effect of three laser pulses and

calculate the propagator of the full interferometer sequence. Finally, with this propagator we calculate the interferometer signal including phase and amplitude. The goal of all the mathematics is to account for as many effects as possible by coordinate transformations. The remaining dynamics then still have to be approximated, but because they are small, the overall accuracy of the calculation is still very high.

This chapter gives a full quantum mechanical calculation for the interferometer phase that includes effects from the shape of the initial atom cloud and the finite length of the laser pulses. These two effects are usually neglected, but a numerical comparison shows that the phase difference that is introduced by these approximations can easily exceed $10 \mu\text{rad}$. This is above the target accuracy of the experiment and it is therefore imperative to compare the measurements with the full quantum mechanical calculations.

7.2 Experiment

In the group of Prof. M. Kasevich at Stanford University, an experiment is being prepared which is to set a new limit on the equivalence principle using the extraordinary sensitivity of atom interferometers to gravity. The equivalence principle is a fundamental assumption in both Newtonian mechanics and General Relativity and states that gravitational mass and inertial mass are the same. If these two are the same, they cancel out in the equations of motion with the consequence that all objects in a gravitational field have the same acceleration g and follow the same trajectories. If the two masses are not exactly equal two objects with different mass ratios (gravitational mass/inertial mass) will feel a different gravitational acceleration. A difference in g between two objects with different mass thus indicates a violation of the equivalence principle. The target accuracy of the Stanford experiment is

$$\frac{\Delta(g_1 - g_2)}{g} = 10^{-15}, \quad (7.1)$$

which would set a new limit on the validity of the equivalence principle [3]. The gravity induced phase difference between the two paths in the interferometer that is being built is approximately 3×10^8 rad. Therefore we need a phase resolution of 10^{-7} rad to reach the target accuracy of g . Obviously, before such an accuracy can be claimed, one needs a detailed understanding of all effects besides gravity that give rise to a phase shift and may cause an erroneous interpretation of gravity differences. In this chapter we will consider a few of these effects, including gradients in the gravitational acceleration, the rotation of the Earth, finite lengths of laser pulses and effects of the shape of the initial atomic wavefunction.

The experiment is composed of two distinct measurements of the gravitational acceleration for two different species of atoms. In the following, however, we will consider the measurement with only one species. The interferometer is of a time-based Mach-Zehnder type in which the atoms are launched vertically, see Figure 7.1. The experiment starts with the formation of a cold atomic sample underneath a “launching” tower. This cloud then is accelerated upwards with a laser pulse to a velocity that is such that the top of the parabolic trajectory lies underneath the top of the tower.

During the free fall of the atoms through the tower, three other laser pulses act as

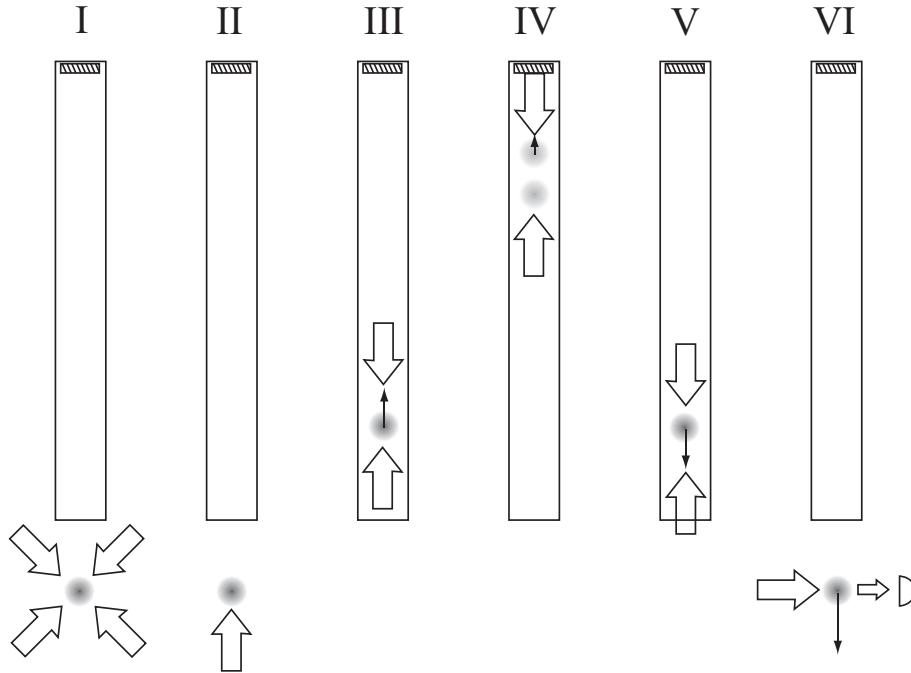


Figure 7.1: Schematic representation of the pulse sequence in the Stanford experiment. Large arrows indicate lasers and the small arrows the atomic velocity. I:cooling, II:acceleration, III: $\pi/2$ pulse, IV: π pulse, V: $\pi/2$ pulse, VI:detection.

beamsplitters for the atomic interferometer. The goal of these pulses is to (partially) excite and de-excite the atoms to a different internal energy level with an associated different momentum. The first pulse of length τ excites the atoms to an equal superposition of the original and the excited state ($\pi/2$ pulse). Then because of the momentum difference, the excited atoms, or strictly speaking the excited state part of the total wavefunction, and the atoms that have not absorbed any photons will spatially separate. At $t = T + \tau$, when the atoms are at the top of the tower, a second pulse of length 2τ inverts the atomic populations (π pulse). That is, the excited atoms will now be de-excited and lose the extra momentum. The other atoms in the original energy level will now be excited and acquire the extra photon momentum. After the second pulse the two atomic clouds will again get closer together. At the moment that the two clouds are again at (approximately) the same position, at $t = 2T + 3\tau$, a third laser pulse ($\pi/2$) is applied. If there was no phase difference between the two trajectories all atoms will end up in the original energy level with the same momentum. If there is a phase difference, a part of the atoms will be in the excited level. Finally, a detection pulse measures the number of atoms in one of the two energy states, from which this phase difference is deduced.

7.3 External Hamiltonian

We will describe the experiment analogous to Section 6.2.2 in the coordinate system that is indicated in Figure 7.2 which models a lab on the rotating surface of the earth. The

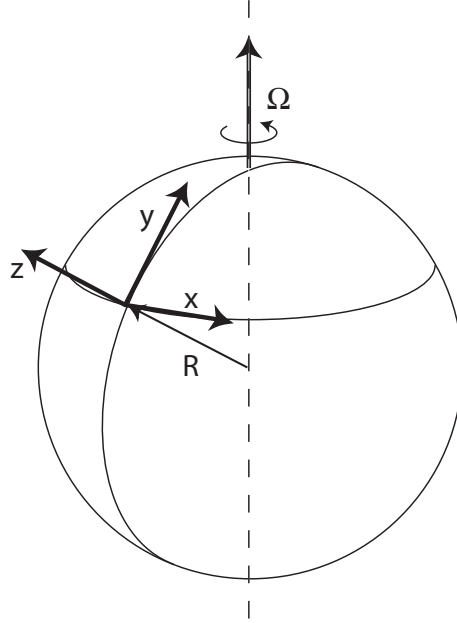


Figure 7.2: Schematic representation of the coordinate system.

origin of this coordinate system lies at the interferometer and is located at a distance \mathbf{R} from the center of rotation. This vector¹ \mathbf{R} is drawn relative to the center of the earth, although it can be defined to any point on the axis of rotation with the same results for the calculations. The rotation is described by the vector $\boldsymbol{\Omega}$.

The total Hamiltonian that describes the evolution of the atomic cloud in the rotating frame is composed of a part \hat{H}_0 that describes the internal energy levels of the atoms, a part \hat{H}_{ext} that describes inertial effects and a time-dependent term \hat{H}_{laser} that gives the interaction with the laser pulses:

$$\hat{H}_{tot} = \hat{H}_0 + \hat{H}_{ext}(\hat{\mathbf{r}}, \hat{\mathbf{p}}) + \hat{H}_{laser}(\hat{\mathbf{r}}, t). \quad (7.2)$$

The external Hamiltonian like in Section 6.2.2 is given by:

$$\hat{H}_{ext} = \frac{\hat{\mathbf{p}}^2}{2m} - m\mathbf{g} \cdot \hat{\mathbf{r}} - \frac{m}{2} \hat{\mathbf{r}} \cdot \vec{\Gamma} \hat{\mathbf{r}} - (\hat{\mathbf{r}} + \mathbf{R}) \cdot \vec{\Omega} \hat{\mathbf{p}} + V(\hat{\mathbf{r}}), \quad (7.3)$$

where \mathbf{g} is the local gravitational acceleration at the origin of the coordinate system (at $\mathbf{r} = \mathbf{0}$), $\vec{\Gamma}$ is the gravity gradient (second order expansion of the local gravitational potential or the first order derivative of \mathbf{g} at the origin of the coordinate system) and \mathbf{R} is the separation of the origin of the coordinate system from the center of rotation. By using this matrix notation for the rotation (see Subsection 6.2.2 for the definition of $\vec{\Omega}$) we avoid

¹In this work boldfaced symbols indicate 3-dimensional vectors, symbols with a hat are quantum mechanical operators and symbols with a double arrow on top represent 3×3 matrices. Vectors are in column notation such that the product of a matrix followed by a vector gives a new vector. A dot between two vectors indicates the dot product which results in a number. Identity- and zero matrices and vectors do not have an extra symbol, but it is always clear from the context what the dimensions are.

vector cross products and are able to write all terms in the Hamiltonian as dotproducts and matrix multiplications which are more convenient to work with. The potential V includes all terms that are of higher order in r and p . In this work, however, we will take this potential zero. Note that $\hat{\mathbf{r}}$ and $\hat{\mathbf{p}}$ are both vectors (with 3 components) and operators (for commutation relations see Appendix A.1).

The Schrödinger equation with the total Hamiltonian can not be solved exactly, but with only the external Hamiltonian it can. It is then a logical step to use an interaction representation in which the external Hamiltonian has been eliminated and has thus been taken into account exactly. Bordé showed ([4, 5], see also Appendix A.2) that this elimination can be achieved by a series of transformations, which replace $\hat{\mathbf{r}}$ (and $\hat{\mathbf{p}}$) in the following way

$$\hat{\mathbf{r}} = \vec{A}\hat{\mathbf{r}}' + \vec{B}\hat{\mathbf{p}}'/m + \boldsymbol{\xi} \quad (7.4)$$

$$\hat{\mathbf{p}} = m\vec{C}\hat{\mathbf{r}}' + \vec{D}\hat{\mathbf{p}}' + \boldsymbol{\zeta}. \quad (7.5)$$

The prime on the position and the momentum operator in these equations only refers to the interaction picture that is used; The coordinate system is the same in both pictures. In the following we will therefore drop the primes. After the transformations the Hamiltonian has the following form:

$$\hat{H} = \hat{H}_0 + \hat{H}_{laser} \left(\vec{A}(t)\hat{\mathbf{r}} + \vec{B}(t)\hat{\mathbf{p}}/m + \boldsymbol{\xi}(t), t \right). \quad (7.6)$$

The 3×3 matrices \vec{A} (components are dimensionless) and \vec{B} (components have the dimension of time) which describe this coordinate transformation obey the following set of differential equations:

$$\frac{d}{dt} \begin{pmatrix} \vec{A} & \vec{B} \\ \vec{C} & \vec{D} \end{pmatrix} = \vec{M} \begin{pmatrix} \vec{A} & \vec{B} \\ \vec{C} & \vec{D} \end{pmatrix} \quad (7.7)$$

with the initial condition:

$$\begin{pmatrix} \vec{A} & \vec{B} \\ \vec{C} & \vec{D} \end{pmatrix}_{t=0} = \begin{pmatrix} 1 & 0 \\ 0 & 1 \end{pmatrix} \quad (7.8)$$

where \vec{M} is a 6×6 matrix:

$$\vec{M} \equiv \begin{pmatrix} \vec{\Omega} & 1 \\ \vec{\Gamma} & \vec{\Omega} \end{pmatrix}. \quad (7.9)$$

The vectors $\boldsymbol{\xi}(t)$ and $\boldsymbol{\zeta}(t)$ follow the differential equations:

$$\begin{aligned} \frac{d}{dt} \begin{pmatrix} \boldsymbol{\xi} \\ \boldsymbol{\zeta}/m \end{pmatrix} &= \vec{M} \begin{pmatrix} \boldsymbol{\xi} \\ \boldsymbol{\zeta}/m \end{pmatrix} + \begin{pmatrix} \vec{\Omega}\mathbf{R} \\ \mathbf{g} \end{pmatrix} \\ \begin{pmatrix} \boldsymbol{\xi} \\ \boldsymbol{\zeta}/m \end{pmatrix}_{t=0} &= \begin{pmatrix} 0 \\ 0 \end{pmatrix}. \end{aligned} \quad (7.10)$$

There is a slight apparent difference with the result of Bordé [6], because he places the origin of his coordinate system at the center of the earth ($\mathbf{R} = 0$). This however results

in confusing definitions of \mathbf{g} and $\vec{\Gamma}$. Therefore we chose to recast his calculations in the reference frame of Fig. 7.2, so that \mathbf{g} and $\vec{\Gamma}$ indeed describe the local acceleration and gradient at the position of the interferometer instead of the center of the earth.

The set of differential equations 7.10 is identical to the classical Hamilton equations for an atom that starts at $\mathbf{r}_0 = \mathbf{0}$ and $\mathbf{p}_0 = \mathbf{0}$ where the classical position has been replaced by $\boldsymbol{\xi}$ and the classical momentum by $\boldsymbol{\zeta}$. For these special initial conditions, the vector $\boldsymbol{\xi}(t)$ thus describes the classical trajectory. One can readily show that the classical trajectories for general initial conditions are given by:

$$\begin{pmatrix} \mathbf{r}_{cl}(t) \\ \mathbf{p}_{cl}(t)/m \end{pmatrix} = \begin{pmatrix} \vec{A}(t) & \vec{B}(t) \\ \vec{C}(t) & \vec{D}(t) \end{pmatrix} \begin{pmatrix} \mathbf{r}_0 \\ \mathbf{p}_0/m \end{pmatrix} + \begin{pmatrix} \boldsymbol{\xi}(t) \\ \boldsymbol{\zeta}(t)/m \end{pmatrix} \quad (7.11)$$

$$\mathbf{p}_0 = m \left(\mathbf{v}_0 - \vec{\Omega}(\mathbf{r}_0 + \mathbf{R}) \right). \quad (7.12)$$

The transformations 7.5 are thus the quantum equivalent of a coordinate transformation to a system that follows the free fall of the atom (see also Section 6.2.2).

The big advantage of these transformations is that in this interaction picture most of the time (between laser pulses) nothing happens and the atomic wavefunction changes only during the short laser pulses. Because of the short duration of the laser pulses (typically 10 μ s) these changes are relatively small and it is easier to use a perturbative approach.

If $\vec{\Omega}$ and $\vec{\Gamma}$ are time-independent, it is possible to find an exact solution to Equations 7.8 and 7.10. Furthermore, the rotation rate and the gravity gradient are usually sufficiently small compared to the time scale T of the experiment ($\|\vec{\Omega}_{Earth}\|T \ll 1$, $\|\vec{\Gamma}_{Earth}\|T^2 \ll 1$) to allow a series expansion in time [6]:

$$\begin{pmatrix} \vec{A} & \vec{B} \\ \vec{C} & \vec{D} \end{pmatrix} = e^{\vec{M}t} = 1 + \vec{M}t + \frac{1}{2!} \vec{M}^2 t^2 + \dots \quad (7.13)$$

$$\begin{aligned} \begin{pmatrix} \boldsymbol{\xi} \\ \boldsymbol{\zeta}/m \end{pmatrix} &= \vec{M}^{-1} \left(e^{\vec{M}t} - 1 \right) \begin{pmatrix} \vec{\Omega}\mathbf{R} \\ \mathbf{g} \end{pmatrix} \\ &= \left(t + \frac{1}{2!} \vec{M}t^2 + \frac{1}{3!} \vec{M}^2 t^3 + \dots \right) \begin{pmatrix} \vec{\Omega}\mathbf{R} \\ \mathbf{g} \end{pmatrix}. \end{aligned} \quad (7.14)$$

7.4 Laser Interaction

With the removal of the external Hamiltonian (in the new interaction picture) the Hamiltonian Eq. 7.6 still includes the internal Hamiltonian and the interaction with the lasers. To continue, we need to specify these two terms and form a model for the laser interaction and the relevant internal energy levels. In this work, we will only consider a two-level atom interacting with a single (infinitely large) running laser wave. This is a valid approximation if the energy differences with all other levels are large in comparison with the laser detuning. One can think of single photon processes in which the laser is tuned to resonance with an atomic transition. However, often multi-photon processes such as Raman transitions and Bragg scattering can also be described as an effective two level system.

In the rotating wave approximation without spontaneous emission, the effective laser interaction relative to the original lab frame and in $(|e\rangle, |g\rangle)$ spinor notation² is:

$$\hat{H}_{laser} = \frac{\hbar}{2} \begin{pmatrix} 0 & \Omega_R e^{i(\mathbf{k}_{eff} \cdot \hat{\mathbf{r}} - \Delta_l t + \phi_0)} \\ \Omega_R e^{-i(\mathbf{k}_{eff} \cdot \hat{\mathbf{r}} - \Delta_l t + \phi_0)} & 0 \end{pmatrix}. \quad (7.15)$$

Where Ω_R is the effective Rabi-frequency, \mathbf{k}_{eff} is the effective laser wavevector, Δ_l is the effective laser detuning from resonance and ϕ_0 is the phase offset of the laser. Then, after the transformations described in the previous section, we get:

$$\hat{H}'_{laser} = \frac{\hbar}{2} \begin{pmatrix} 0 & \Omega_R e^{i\hat{\phi}(t)} \\ \Omega_R e^{-i\hat{\phi}(t)} & 0 \end{pmatrix} \quad (7.16)$$

$$\hat{\phi}(t) = \mathbf{k}_{eff} \cdot \left(\vec{A}(t)\hat{\mathbf{r}} + \vec{B}(t)\hat{\mathbf{p}} + \boldsymbol{\xi}(t) \right) - \Delta_l t + \phi_0. \quad (7.17)$$

The evolution of the atom during the laser pulse from the starting point t_0 is given by the 2×2 propagator matrix \hat{U}_{laser} :

$$|\Psi(t_0 + \tau)\rangle = \hat{U}_{laser}(t_0, \tau) |\Psi(t_0)\rangle, \quad (7.18)$$

whose time dependence is given by the Schrödinger equation

$$i\hbar \frac{d}{d\tau} \hat{U}_{laser}(t_0, \tau) = \hat{H}'_{laser} \hat{U}_{laser}(t_0, \tau) \quad (7.19)$$

$$\hat{U}_{laser}(t_0, 0) = 1. \quad (7.20)$$

This can be a very complicated set of equations, because of the time dependence of \hat{H}'_{laser} (through $\hat{\phi}$) and the fact that \hat{H}'_{laser} is an operator (function of $\hat{\mathbf{r}}$ and $\hat{\mathbf{p}}$). It can be solved in the case of uniform gravitational field without rotation and gravity gradients [7]. In general, however, it is impossible to get a closed form solution to this set of equations and one has to resort to numerical calculations.

When the inertial effects (\mathbf{g} , $\vec{\Gamma}$ and $\vec{\Omega}$) and the detuning are small enough, the phase $\hat{\phi}(t)$ only changes very slowly with time. We know that in this case the evolution will look very much like an unperturbed Rabi oscillation (with $\Delta_l = 0$). The atoms will oscillate between the ground and the excited state and the upper level acquires the phase of the laser [8]. To take these two effect into account exactly, we take two more transformations (see Appendix A.4), after which the remaining changes in the wavefunction are only very small. Then we get an approximate solution using a Dyson expansion of the propagator and transform this solution back to the frame of Equation 7.17. The result is still fully analytic, but very extensive so we will leave its evaluation to the computer.

Some insight can be obtained if we keep track of all the exponential phase terms. If we take those terms separately, the effect of a laser pulse that starts at t_0 is described by a matrix that has the following form:

$$\hat{U}_{laser} = \begin{pmatrix} e^{i\hat{\phi}(t_0+\tau)} \hat{U}_{ee}(t_0, \tau) e^{-i\hat{\phi}(t_0)} & e^{i\hat{\phi}(t_0+\tau)} \hat{U}_{eg}(t_0, \tau) \\ \hat{U}_{ge}(t_0, \tau) e^{-i\hat{\phi}(t_0)} & \hat{U}_{gg}(t_0, \tau) \end{pmatrix}. \quad (7.21)$$

²an atom is described by a vector whose first component is the wavefunction of the excited state and the second component is the wavefunction of the ground state

The coefficient with \hat{U}_{ee} , for example, describes the effect on the wavefunction for atoms that are initially in the excited state and remain in the excited state after the laser pulse. The full recipe for all the coefficients \hat{U}_{ij} can be found in Appendix A.4.

We see that the phases of the diagonal terms are very small: the ground state diagonal term does not have an explicit phase term and the excited state diagonal has two phase factors that largely cancel out because of the short length of the laser pulse τ . The off-diagonal elements of this matrix, however, carry a large phase factor $\hat{\phi}(t_i)$, the phase of the laser. This constitutes the laser phase rule: an atom acquires the phase of a photon when this photon is absorbed and the phase is lost when the photon is emitted. This laser phase rule forms the basis for most atomic phase calculations. All standard phase terms like the Sagnac phase and the kgT^2 gravity term are directly derived from the phase $\phi(t)$ (Eq. 7.17). The terms \hat{U}_{ij} , however, also give a contribution to the phase and have to be taken into account for precision measurements.

7.5 Atom Interferometry

With the inertial effects taken into account by Bordés $ABCD\xi$ transformation (Section 7.3) and the effect of individual laser pulses described by Equation 7.21, we have all the tools we need to calculate the output of the interferometer. In this section we will derive a general expression for the interferometer signal, from which the phase and the amplitude of the detector signal can be derived.

As mentioned in Section 7.2, the interferometer will be of a pulsed Mach-Zehnder type. Because transitions between internal (electronic) energy levels are accompanied by a change in the atomic momentum, atoms that absorb or emit photons in a different laser pulse, will follow a different trajectory. In Figure 7.3 the timing of the pulses is depicted together with a schematic indication of all possible atomic trajectories $z(t)$. In reality the trajectories will be parabolic, but for clarity this has been omitted from the drawing. We assume that the laser is infinitely wide so that the laser intensity is uniform. Furthermore, we assume square pulses in time (laser is either on or off) with constant intensity that is the same for all three pulses. The length τ of the first and the last pulse are chosen such that they form an effective $\pi/2$ pulse that transfers half of the atoms from one internal state to the other. The second pulse is of length 2τ to create a π pulse. The two periods T in between pulses are taken identical, so that the total time lapse from beginning of first pulse to end of third pulse is $2T + 4\tau$.

After the third pulse, the total number of atoms in the ground state is measured. In general, especially for an atomic cloud with large width or divergence, this number is formed by a superposition of four interfering paths. Two paths end up at (approximately) the same position, but two other paths end up at some distance. When the spatial separation between paths is much larger than the size of the detection area and the width of the atomic beam, the two extreme paths do not contribute to the detector signal and only two paths are needed to describe the interference signal. A fact that further ratifies this approach is that experimentally the length of the second pulse can be tuned very accurately such that the relative occupation of the two extreme paths is very low. The figure shows that the two extreme paths are followed by atoms that do not make a transition during the second

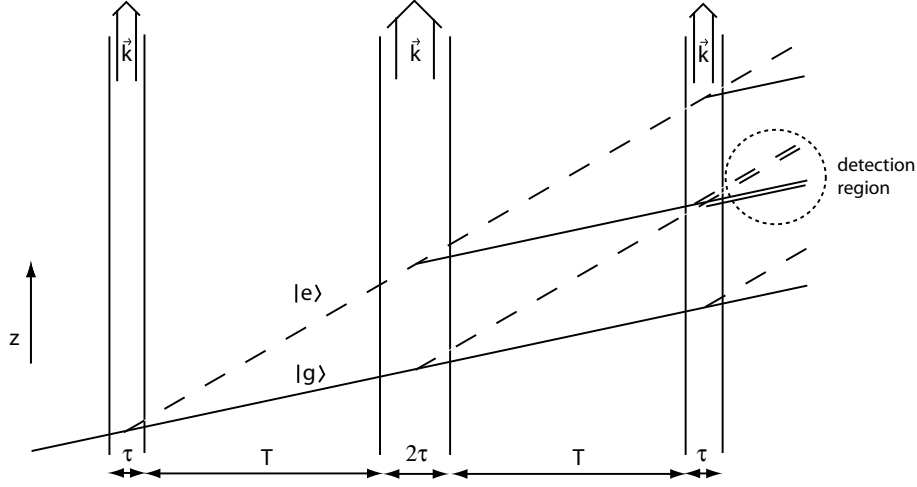


Figure 7.3: Schematic representation of a time based MachZehnder interferometer.

laser pulse. Mathematically, the complex amplitudes of these paths have a diagonal term of the second laser matrix \hat{U}_{laser} and these paths can thus be removed from the model by setting these terms to zero.

This time based interferometer can readily be described by cutting the total sequence in five parts with constant laser intensity. The interaction between pulses is trivial: $H'_{laser} = 0$, and thus the wavefunction in the comoving reference frame does not change. The total evolution in the interferometer \hat{U}_{MZ} is then described by the interaction with the laser, $\hat{U}_{laser}(t_{start}, \tau_{pulse})$, only:

$$\hat{U}_{MZ} = \hat{U}_{laser}(2T + 3\tau, \tau) \hat{U}_{laser}(T + \tau, 2\tau) \hat{U}_{laser}(0, \tau). \quad (7.22)$$

After setting the diagonal terms of the second laser interaction matrix to zero (two path approximation), we obtain the evolution matrix of the total interferometer. The coefficient of the total propagator that describes the transition from ground state at the beginning to ground state at the end is given by the lower diagonal element of the total propagator, $\hat{U}_{MZ,gg}$ (see Appendix A.5):

$$\hat{U}_{MZ,gg} = e^{-i\hat{\phi}_3^0} e^{i\hat{\phi}_2^+} \left(\hat{g}_1 + e^{-i\hat{\phi}_{MZ}} \hat{g}_2 \right) \quad (7.23)$$

$$\begin{aligned} \hat{\phi}_{MZ} = & \hat{\phi}_1^+ - \hat{\phi}_2^0 - \hat{\phi}_2^+ + \hat{\phi}_3^0 \\ & - \frac{i}{2} \left([\hat{\phi}_2^+, \hat{\phi}_3^0] + [\hat{\phi}_2^0, \hat{\phi}_1^+] - [\hat{\phi}_2^+ - \hat{\phi}_3^0, \hat{\phi}_1^+ - \hat{\phi}_2^0] \right). \end{aligned} \quad (7.24)$$

The operators \hat{g}_1 and \hat{g}_2 describe the two complex valued contributions from the two interfering paths of the interferometer that include the transition amplitudes from the laser pulses and the (usually small) phase corrections from the finite pulse length. An expression of these two variables in terms of the components of the laser matrices can be found in Appendix A.5 (Eq. A.68).

The interferometer phase $\hat{\phi}_{MZ}$ is composed of the effective (in the co-moving reference frame) laser phase operator at the end of the first pulse (denoted with a plus sign, $\hat{\phi}_1^+$)

and the end of the second pulse ($\hat{\phi}_2^+$). It also contains the phases at the beginning of the second ($\hat{\phi}_2^0$) and the third pulse ($\hat{\phi}_3^0$) (Eq. A.66). Notice that \hat{g}_1 , \hat{g}_2 and $\hat{\phi}_{MZ}$ are operators, because they are a function of $\hat{\mathbf{r}}$ and $\hat{\mathbf{p}}$.

In the case that all atoms were initially in the ground state with wavefunction $|\Psi_{0,g}\rangle$, the fraction of atoms that are still in the ground state at the end of the interferometer sequence can be calculated as:

$$\begin{aligned} P_{gg} &= \langle \Psi_{0,g} | \hat{U}_{MZ,gg}^\dagger \hat{U}_{MZ,gg} | \Psi_{0,g} \rangle \\ &= \langle \Psi_{0,g} | \hat{g}_1^\dagger \hat{g}_1 + \hat{g}_1^\dagger e^{i\hat{\phi}_{MZ}} \hat{g}_2 + \hat{g}_2^\dagger e^{-i\hat{\phi}_{MZ}} \hat{g}_1 + \hat{g}_2^\dagger \hat{g}_2 | \Psi_{0,g} \rangle, \end{aligned} \quad (7.25)$$

where the dagger denotes the Hermite conjugate. This is an oscillating function, where $\langle \Psi_{0,g} | \hat{g}_1^\dagger e^{i\hat{\phi}_{MZ}} \hat{g}_2 | \Psi_{0,g} \rangle + c.c.$ describes the interference fringes and the two terms $\hat{g}_i^\dagger \hat{g}_i$ give the offset.

The easiest way to calculate Eq. 7.25 is to expand $|\Psi_{0,g}\rangle$ in eigenfunctions of $\hat{U}_{MZ,gg}$. This operator $\hat{U}_{MZ,gg}$ fully consists of operators $\hat{\phi}$ which are all linear combinations of $\hat{\mathbf{r}}$ and $\hat{\mathbf{p}}$. The eigenfunctions of such linear combinations of $\hat{\mathbf{r}}$ and $\hat{\mathbf{p}}$ can be calculated analytically and can be found in Appendix A.6. The different phase operators $\hat{\phi}$ consist of different combinations of $\hat{\mathbf{r}}$ and $\hat{\mathbf{p}}$ and do not commute. Therefore, we need to transform to a different set of eigenfunctions for each of the phase operators (see Section 7.6).

Often, in a semi-classical approximation, it is assumed that the original wavefunction is sufficiently located in both space and momentum to approximate it by a delta function in phase space. In that case, the interferometer signal is calculated by replacing the operators $\hat{\mathbf{r}}$ and $\hat{\mathbf{p}}$ in $\hat{U}_{MZ,gg}$ with the initial expectation value ($\hat{\mathbf{r}} \rightarrow \langle \hat{\mathbf{r}} \rangle_0$ and $\hat{\mathbf{p}} \rightarrow \langle \hat{\mathbf{p}} \rangle_0$). In general, however, this substitution does not give the correct result (for example $\langle \hat{x} \rangle^2 \neq \langle \hat{x}^2 \rangle$) and one has to perform a full expansion in eigenfunctions.

7.6 Phase Calculations

In the previous sections we derived an abstract expression for the interferometer signal in the form of operators. For comparison of the theory with the experiment we need to evaluate the expectation value Eq. 7.25. For this, we will start in this chapter by defining the experimental parameters. Subsequently, in Subsection 7.6.2 we will explain how the interferometer signal and the phase are calculated from the expectation value of the full propagator. Subsection 7.6.3 then gives the numerical results of both the interferometer contrast and phase as a function of the laser pulse length and the size of the initial wavefunction. We will see that both these parameters have a significant effect on the interferometer phase that exceeds the target accuracy of the experiment and that indeed it is essential to use the full quantum mechanical treatment to interpret the interferometer signal. However, there are settings at which this correction to the phase is smaller than the required accuracy. We will therefore conclude in Subsection 7.6.4 where we investigate if, at these settings, a semiclassical approach is sufficient to describe the signal.

7.6.1 Parameters

For the numerical calculation of the phase we will use the geometry that is sketched in Fig. 7.2 where we only consider the gravitational field and the rotation of the earth. The gravitational acceleration \mathbf{g} ($g=9.8$ m/s²) is along the z-axis and the x-axis is chosen such that $\Omega_x = 0$ ($\Omega_y=7.29\times 10^{-5} \sin(0.86)$ s⁻¹ at 41 degrees latitude). For the gravitational gradient $\vec{\Gamma}$ we take the field of a perfectly spherical earth $2\Gamma_{xx} = 2\Gamma_{yy} = -\Gamma_{zz} = 2g_z/R$ where $R = 6.38 \times 10^6$ m is the radius of the earth and all other components are zero. For the atomic parameters we will take the values of rubidium ($m = 1.44 \times 10^{-25}$ kg). The atoms interact with two counterpropagating lasers with slightly different frequencies that are tuned such that two ground state levels are resonantly coupled through a far detuned upper level (Raman transition). This way we still have an effective two level system but can transfer more momentum, $\lambda_{eff}=390$ nm. We will assume that the intensity of the pulses is perfectly matched to their length $\Omega_R = \pi/2\tau$.

The atoms are launched with a velocity $v_{z0} = -g_z T$. With a separation between pulses $T = 1.43$ s the atoms reach a maximum height of 10 m. Unless stated otherwise, the atomic cloud has exactly this initial velocity and the middle point of the wavepacket lies exactly at the origin of the coordinate system. In that case, the initial momentum is

$$\mathbf{p}_0 = m \left(\mathbf{v}_0 - \vec{\Omega} \mathbf{R} \right). \quad (7.26)$$

The two photon laser pulses are exactly on resonance (effective detuning $\Delta_l=0$) at the beginning of the interferometer sequence. Because of the curved trajectory, however, the Doppler shift gives a continuous chirp to the effective detuning and quickly brings the atoms out of resonance. Without adjustment of the laser frequency, the (effective) laser detuning at the second pulse would be too large, there would be no momentum transfer and hence the interferometer would not work. To minimize this effect, it is assumed that at the beginning of each pulse the laser frequency is adjusted to compensate for the Doppler shift that is associated with the classical velocity at that moment (the dot indicates a time derivative):

$$\Delta_i = \Delta_l - \mathbf{k}_{eff} \cdot \left(\dot{\vec{A}}(t_i) \mathbf{r}_0 + \dot{\vec{B}}(t_i) \mathbf{p}_0 + \dot{\boldsymbol{\xi}}(t_i) \right). \quad (7.27)$$

Changing the laser frequency during the interferometer sequence keeps the effective detuning small and the used Dyson expansion of the interferometer propagator valid, but changes the laser offset phase ϕ_0 from pulse to pulse. It can readily be shown that this adds a phase to the interferometer signal:

$$\phi_{tune} = \int_{\tau}^{T+\tau} \Delta_l(t) dt - \int_{T+3\tau}^{2T+3\tau} \Delta_l(t) dt. \quad (7.28)$$

This phase is independent of the laser frequency during the pulses and we will omit this phase from further calculations. In the experiment, however, this phase has to be known as precisely as the intended resolution of the measurement and thus requires careful tracking of the laser phase.

7.6.2 Full Wavefunction Integral

In this section we will calculate the interferometer signal as given by Eq. 7.25. However, since we are only interested in the phase and the amplitude of the interference signal, it is sufficient to calculate the expectation value of only one of the complex conjugated $g_1 g_2$ terms. The phase Φ_{int} and amplitude A_{int} of the interference fringes then follow from the result:

$$\Phi_{int} = \arg \left(\langle \Psi_{0,g} | \hat{g}_1^\dagger e^{i\hat{\phi}_{MZ}} \hat{g}_2 | \Psi_{0,g} \rangle \right) \quad (7.29)$$

$$A_{int} = 2 \left| \langle \Psi_{0,g} | \hat{g}_1^\dagger e^{i\hat{\phi}_{MZ}} \hat{g}_2 | \Psi_{0,g} \rangle \right|. \quad (7.30)$$

To calculate this expectation value we write the operators \hat{g}_1 , \hat{g}_2 and $\hat{\phi}_{MZ}$ in terms of linear combinations of $\hat{\mathbf{r}}$ and $\hat{\mathbf{p}}$. Next we insert the identity

$$1 \equiv \int_{-\infty}^{\infty} d\mathbf{p}^3 |\phi(\mathbf{p})\rangle \langle \phi(\mathbf{p})| \quad (7.31)$$

in front of each combination of $\hat{\mathbf{r}}$ and $\hat{\mathbf{p}}$, where $|\phi(\mathbf{p})\rangle$ is an associated eigenvector (see Appendix A.6) to transform the wavefunction to the basis of these eigenvectors. With this transformation we can treat the operators as normal functions of the vectors \mathbf{p} . The cost of these transformations is the introduction of overlap integrals, but these evaluate to simple Gaussians (Appendix A.6, Eq. A.83). To limit the number of these transformations, we approximate the phase derivatives that we need to evaluate the laser transformation matrices (see \hat{H}_8 , Eq. A.58):

$$\frac{d\hat{\phi}}{dt}(t) \approx \mathbf{k}_{eff} \cdot \left(\dot{\hat{A}}(t_i) \hat{\mathbf{r}} + \dot{\hat{B}}(t_i) \hat{\mathbf{p}} + \dot{\hat{\boldsymbol{\xi}}}(t_i) \right) + \mathbf{k}_{eff} \cdot \ddot{\hat{\boldsymbol{\xi}}}(t_i) (t - t_i), \quad (7.32)$$

where we have added the second derivative of $\boldsymbol{\xi}$ because of its relative size. The explicit expression for the time derivative of the phase is only used for the correction terms to the laser interaction. The actual contribution of this expression to the interferometer phase is given by the time integral during the pulse length τ . Because the pulses are short compared to the total length of the pulse sequence, it is likely that this lower order series expansion of the phase evolution during the pulses suffices for the same accuracy of the calculation. The order of the time-expansion of the overall phase ϕ_{MZ} does not influence the number of integrals that have to be performed, because this only has one combination of $\hat{\mathbf{r}}$ and $\hat{\mathbf{p}}$. Therefore, the order of the expansion of $\phi_{MZ}(t)$ in t can be much higher.

To check the validity of this approximation, Table 7.1 gives numerical estimates of the contribution of time derivatives to the correction terms of the laser interaction. In this table the time derivative of the phase is broken up in contributions from \hat{A} , \hat{B} and $\hat{\boldsymbol{\xi}}$. The numerical values are for an interaction time of 100 μs and an atomic cloud of RMS size $\sigma_r = 50 \mu\text{m}$ with an associated momentum spread $\sigma_p = \hbar/2\sigma_r$. The lowest entries indicate the terms that are omitted in the approximation of Equation 7.32. The table shows that for $\tau = 10^{-4}$ s the phase error for all three components is smaller than the intended accuracy 10^{-7} , making this approximation highly valid. Obviously, the approximation gets even better for shorter τ .

	$ \vec{A}^T \mathbf{k}_{eff} \sigma_r$	$ \vec{B}^T \mathbf{k}_{eff} \sigma_p$	$\mathbf{k}_{eff} \cdot \boldsymbol{\xi}$
$\dot{\phi}(T)\tau$	4.4×10^{-7}	2.3×10^{-3}	2.3×10^3
$\ddot{\phi}(T)\tau^2$	2.5×10^{-13}	2.6×10^{-12}	1.6×10^{-2}
$\phi^{(3)}(T)\tau^3/2$			3.5×10^{-13}

Table 7.1: Estimates of the change in laser phase during a laser pulse, broken up into terms of the series expansion in time and in the contributions from \vec{A} , \vec{B} and $\boldsymbol{\xi}$. Values are given for 100 μs pulse lengths and the maximum position and momentum differences ($\sigma_p = \hbar/\sigma_r$) are taken for a 50 μm RMS cloud radius.

The contribution from $\boldsymbol{\xi}$ would give a very large phase if it weren't exactly compensated for by the laser detuning (Eq. 7.27). The second term $\mathbf{k} \cdot \boldsymbol{\xi} \approx \mathbf{k} \cdot \mathbf{g}$ however also gives a phase that is relatively close to unity, indicating that pulse length $\tau = 10^{-4}$ s is at the limit of the validity of the Dyson expansion. Sometimes, the laser frequency is chirped during the pulses to compensate for this large phase term. A very complicated phase evolution of the laser could even compensate the entire $\mathbf{k} \cdot \boldsymbol{\xi}$ term, thereby greatly improving the validity of the used expansion. The \vec{A} and \vec{B} terms, however, can not be compensated by a chirped laser frequency and remain as limiting factors for the accuracy.

With the approximation of the phase (Eq. 7.32), the expression for the interferometer phase has 7 operators that are linear combinations of $\hat{\mathbf{r}}$ and $\hat{\mathbf{p}}$. Together with the transformation Equation 7.31 we get a 21-fold integration of a Gaussian times a polynomial. In terms of the unevaluated laser matrix elements and the unevaluated overlap integrals, this has the form:

$$\begin{aligned}
& \langle \Psi_{0,g} | \hat{g}_1^\dagger e^{i\phi_{MZ}} \hat{g}_2 | \Psi_{0,g} \rangle \\
= & \int d\mathbf{p}_1^3 \int d\mathbf{p}_2^3 \int d\mathbf{p}_3^3 \int d\mathbf{p}_4^3 \int d\mathbf{p}_5^3 \int d\mathbf{p}_6^3 \int d\mathbf{p}_7^3 U_{gg}^1(\mathbf{r}_C, \mathbf{p}_1)^* \\
& \times U_{eg}^2(\mathbf{r}_C, \mathbf{p}_2)^* U_{ge}^3 \left(\mathbf{r}_C + \hbar \left(\vec{B}_3^0 - \vec{B}_2^+ \right)^T \mathbf{k}_{eff}, \mathbf{p}_3 - \hbar \left(\vec{A}_3^0 - \vec{A}_2^+ \right)^T \mathbf{k}_{eff} \right)^* \\
& \times e^{i\phi_{MZ}(\mathbf{r}_C, \mathbf{p}_4)} U_{gg}^3 \left(\mathbf{r}_C + \hbar \left(\vec{B}_2^0 - \vec{B}_1^+ \right)^T \mathbf{k}_{eff}, \mathbf{p}_5 - \hbar \left(\vec{A}_2^0 - \vec{A}_1^+ \right)^T \mathbf{k}_{eff} \right) \\
& \times U_{ge}^2 \left(\mathbf{r}_C + \hbar \left(\vec{B}_2^0 - \vec{B}_1^+ \right)^T \mathbf{k}_{eff}, \mathbf{p}_6 - \hbar \left(\vec{A}_2^0 - \vec{A}_1^+ \right)^T \mathbf{k}_{eff} \right) U_{eg}^1(\mathbf{r}_C, \mathbf{p}_7) \\
& \times \langle \Psi_{0,g} | \dot{\phi}(t_1), \mathbf{p}_1 \rangle \langle \dot{\phi}(t_1), \mathbf{p}_1 | \dot{\phi}(t_2), \mathbf{p}_2 \rangle \langle \dot{\phi}(t_2), \mathbf{p}_2 | \dot{\phi}(t_3), \mathbf{p}_3 \rangle \langle \dot{\phi}(t_3), \mathbf{p}_3 | \phi_{MZ}, \mathbf{p}_4 \rangle \\
& \times \langle \phi_{MZ}, \mathbf{p}_4 | \dot{\phi}(t_3), \mathbf{p}_5 \rangle \langle \dot{\phi}(t_3), \mathbf{p}_5 | \dot{\phi}(t_2), \mathbf{p}_6 \rangle \langle \dot{\phi}(t_2), \mathbf{p}_6 | \dot{\phi}(t_1), \mathbf{p}_7 \rangle \langle \dot{\phi}(t_1), \mathbf{p}_7 | \Psi_{0,g} \rangle,
\end{aligned} \tag{7.33}$$

where the asterisk denotes the complex conjugate and the superscript indices on the functions U indicate the associated laser pulse. The phase term ϕ_{MZ} is obtained from Equation 7.24 by replacing $\hat{\mathbf{r}}$ with an arbitrary, but fixed offset position \mathbf{r}_C (we take $\mathbf{r}_C = \mathbf{0}$) and $\hat{\mathbf{p}}$ with the running integration variable \mathbf{p}_4 . The eigenfunctions $|\dot{\phi}(t_i), \mathbf{p}_j\rangle$ are calculated with Equations A.77 and A.81, taking $\mathbf{v} = \dot{\vec{A}}^T(t_i)\mathbf{k}_{eff}$, $\mathbf{w} = \dot{\vec{B}}^T(t_i)\mathbf{k}_{eff}$ and $\mathbf{p}_c = \mathbf{p}_j$. A

similar recipe is applied for $|\phi_{MZ}, \mathbf{p}_4\rangle$. Finally, the initial wavefunction is a 3D-Gaussian

$$\langle \mathbf{r} | \Psi_{g,0} \rangle = e^{-(\mathbf{r}-\mathbf{r}_0)^2/w_0^2 + i\mathbf{p}_0 \cdot \mathbf{r}/\hbar}, \quad (7.34)$$

with waist $w_0 = 2\sigma_{r,0}$, momentum \mathbf{p}_0 (Eq. 7.26) and a possible offset position \mathbf{r}_0 which is usually taken zero. This is the optimal initial wavefunction that has minimum uncertainty in \mathbf{r} and \mathbf{p} . In practice, this form is very difficult to obtain and the actual atomic wavefunction has a more complicated form. In that case the following results that are based on this Gaussian shape can be considered as a limiting case for an optimal interference signal.

Equation 7.33 can in principle be solved analytically, however the solution is too extensive to handle in full symbolic form. Therefore we calculated the exact solution of the integral only with numerical values of the parameters and repeated this calculation for various values of the pulse length and the initial RMS cloud radius $\sigma_{r,0}$. The amplitude and the phase were then evaluated from the result using Equations 7.29 and 7.30 using symbolic algebra software (Maple). The result of the integration is in the form of a large phase in an exponential term, multiplied with a complex number with small phase. By evaluating the phases of these terms separately, it is possible to determine the full phase without the need to take the modulus of 2π . The calculations were performed with 50 digits accuracy and a 5th order expansion of \vec{A} , \vec{B} and ξ in t (Eq. 7.13 and 7.14).

7.6.3 Results

The resulting amplitude A_{int} are drawn in Figure 7.4 as a function of the initial RMS cloud size $\sigma_{r,0}$. It turns out that the contrast hardly changes with the interaction time and that the graphs for $\tau \leq 13 \mu\text{s}$ are indistinguishable. Only close to $100 \mu\text{s}$ does the amplitude decrease slightly (see the $\tau = 63 \mu\text{s}$ plot), but at this point the approximations used lose their validity. The contrast depends much more strongly on $\sigma_{r,0}$ with two boundaries above and below which the amplitude quickly drops to zero. The position of these boundaries, i.e, the maximum allowed position spread $\sigma_{r,max}$ and maximum allowed Heisenberg limited momentum spread $\sigma_{p,max} = \hbar/2\sigma_{r,min}$, can be estimated from the expression of ϕ_{MZ} . These boundaries are given by the difference in initial position or momentum over which the interferometer phase has changed by π . From a leading terms estimate of \vec{A} and \vec{B} we get

$$\sigma_{r,max} = \frac{\pi}{2k_{eff}\Gamma T^2} = 1.6 \times 10^{-2}\text{m} \quad (7.35)$$

$$\sigma_{r,min} = \frac{2\hbar k_{eff}\Omega T^2}{m\pi} = 1.1 \times 10^{-6}\text{m}. \quad (7.36)$$

In this case, the criterion on the maximum spread in position originates in the difference in gravity that acts on atoms on opposite sides of the cloud. The other criterion traces back to the difference in Sagnac phase between two atoms that have opposite initial velocity perpendicular to the laser. The numerical values are in good agreement with the graph. Although usually $\sigma_{r,min} < \sigma_{r,max}$ it is possible that the restrictions on both the momentum and the position spread are so strong that $\sigma_{r,min} > \sigma_{r,max}$ and there is no range in which interference fringes can be observed.

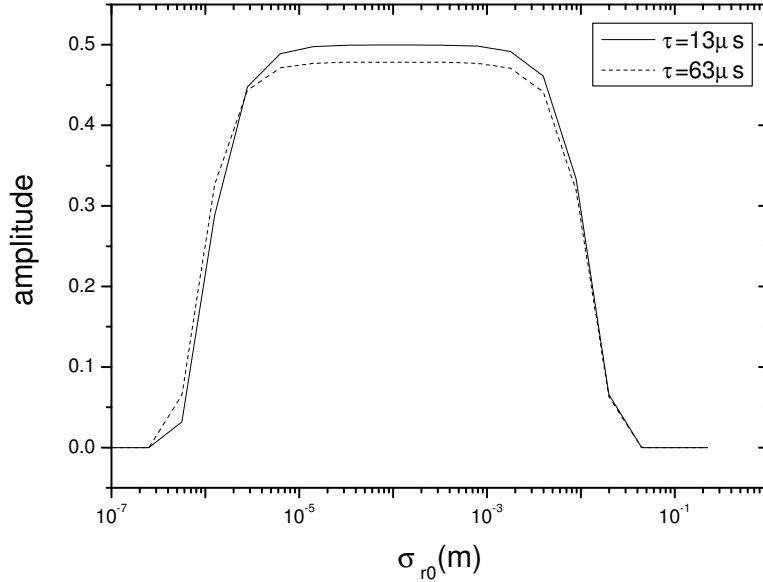


Figure 7.4: amplitude of the interference signal as a function of the initial cloud size w_0

The phases that are obtained from Equation 7.33 for $\sigma_{r,0}=0.35$ mm are plotted in Figure 7.5 relative to the phase at $\tau = 10^{-7}$ s (approximately 3.2×10^8 rad) as a function of the interaction time τ . In this plot, the total time lapse of the interferometer sequence $2T + 4\tau$ was kept constant, but the graph shows that there is still a strong dependence on the laser interaction time. This effect was also found when only gravity was considered [9]. This strong phase dependence on τ can largely be eliminated by choosing a different compensation of T on the pulse length (calculation showed that the optimal choice was to keep approximately $2T+2\tau$ fixed), but it is unclear what the physical significance of this is and we will stick to our choice. The behavior of the phase as a function of τ looks very similar for other values of $\sigma_{r,0}$. Therefore, we will take the interferometer phase for this initial waist $\phi_{0.35\text{ mm}}(\tau)$ as a reference for the following graphs and consider the differences with this reference only.

In Figure 7.6 the interferometer phase relative to the reference $\phi_{0.35\text{ mm}}(\tau)$ is plotted as a function of $\sigma_{r,0}$ for various values of the interaction time τ . The plot shows that there is a minimum in the phase at $\sigma_{r,0}=0.35$ mm for all interaction times τ (this is the reason why this was chosen as a reference). For larger initial clouds the interferometer phase increases with $\sigma_{r,0}$ squared and for smaller $\sigma_{r,0}$ the phase goes with $1/\sigma_{r,0}^2$. It is unclear what the reason is for the power of 2, but qualitatively we can expect such a behavior because the phase operator depends on \hat{r} and \hat{p} . The measured phase is a kind of average of this operator over the entire cloud and we can expect that when the cloud gets larger (either in real or in momentum space) that the average value gets shifted more and more. The phase minimum is at the point where the contributions from the size and the momentum

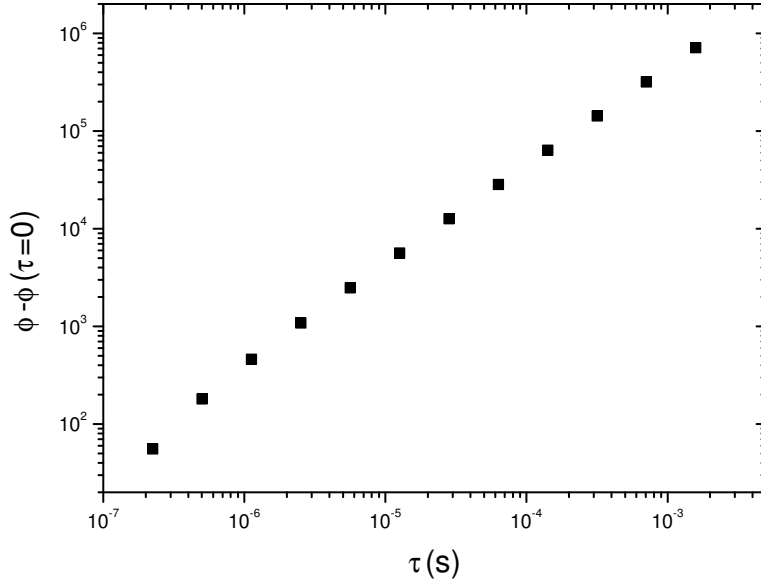


Figure 7.5: Interferometer phase relative to phase at $\tau = 10^{-7}$ s as a function of τ for $\sigma_{r,0}=0.35$ mm

spread are equal. Experimentally, this cloud size is the best to choose, because then the sensitivity for differences in cloud size is minimal. The graphs also clearly shows that shorter interaction times give less effect of $\sigma_{r,0}$ on the phase. In the limit $\tau \rightarrow 0$ we return to the short pulse limit in which there is no effect of the initial cloud size at all.

In Figure 7.7 the same data is now plotted as a function of τ . According to the graph, the phase (relative to the reference $\phi_{0.35\text{mm}}(\tau)$) grows approximately cubical with τ for all values of the initial RMS cloud size and over the entire plotted range of τ . At $\tau=100 \mu\text{s}$ the phase term $\mathbf{k}_{eff} \cdot \mathbf{g}\tau^2 \approx 1$. Then the approximations are no longer valid which explains the jumps in phase and the missing points (in the logarithmic scale).

7.6.4 Semiclassical Approximation

There is a range of the initial RMS cloud size around 1 mm in which the phase does not change by more than 10^{-7} rad, the target accuracy of the experiment. It is thus possible that within this range a semiclassical approach is sufficient for the required accuracy. To test this, we calculated the signal Eq. 7.25 not by a full expansion in eigenvectors, but simply by replacing all $\hat{\mathbf{r}}$ by \mathbf{r}_0 and all $\hat{\mathbf{p}}$ by \mathbf{p}_0 . The phase difference between this calculation and the full eigenvector integral (Eq. 7.33) is given in Figure 7.8 as a function of the pulse length. Again, the approximations are only valid for interaction times up to $100 \mu\text{s}$.

The semiclassical calculations are completely independent on the initial waist and depend only on the initial position and momentum. The full quantum calculations do depend

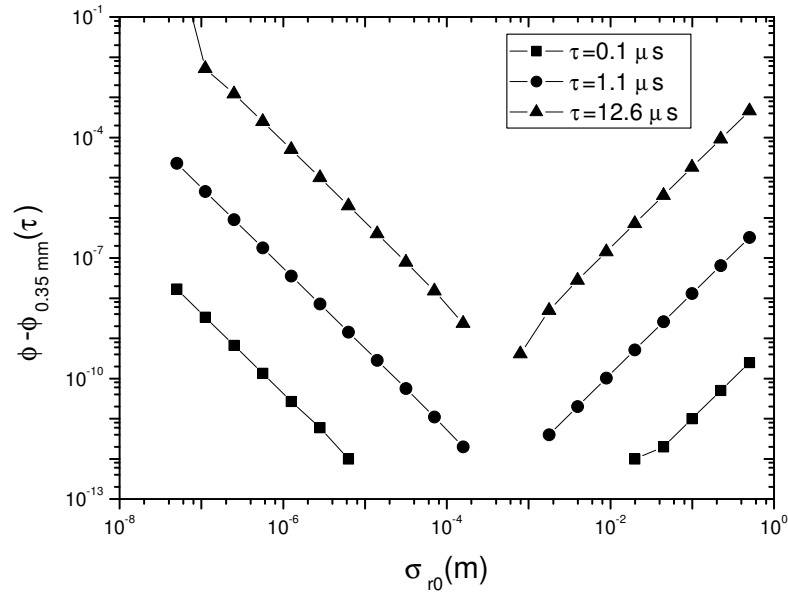


Figure 7.6: Interferometer phase relative to the phase for $\sigma_{r,0}=0.35$ mm (Fig. 7.5) as a function of $\sigma_{r,0}$

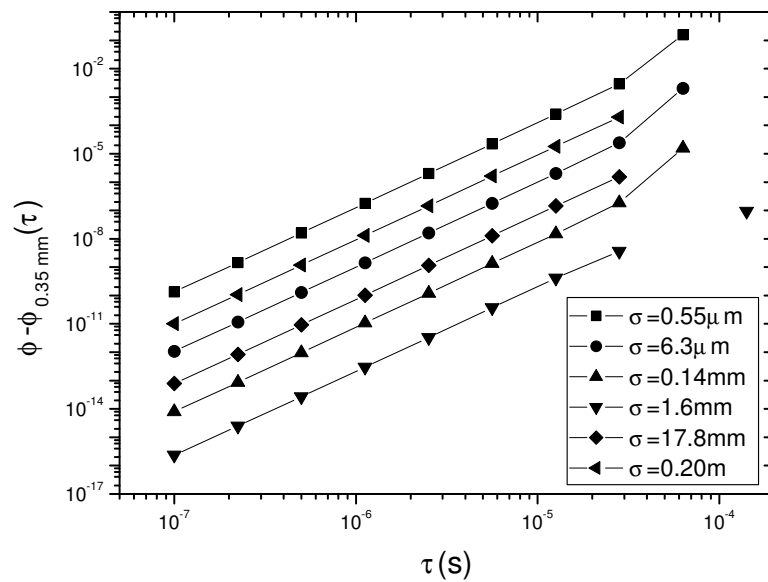


Figure 7.7: Interferometer phase relative to the phase for $\sigma_{r,0}=0.35$ mm (Fig. 7.5) as a function of τ

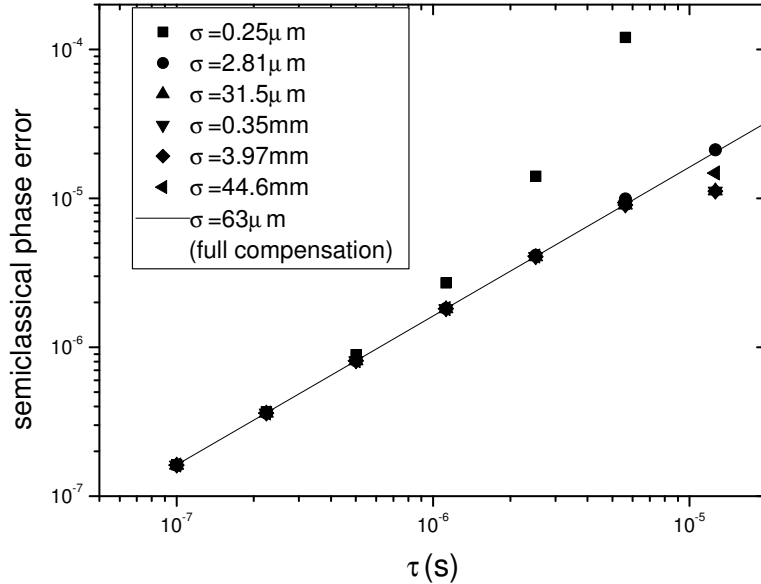


Figure 7.8: Difference in interferometer phase between semiclassical calculations and the full quantum approach as a function of the interaction time τ for various values of the initial waist w_0 . The line indicates the phase error when rotation is zero and the Doppler shift from the classical trajectory is exactly compensated with a chirped laser frequency.

on the size of the cloud, but on the scale of the graph, this dependency is hardly visible. This means that the error of the semiclassical calculation is much larger than the effect of the initial cloud size on the interferometer phase. There are thus other effects at play that are at this point not yet understood. The calculations show that the error that is made by the semiclassical approximation is a few orders of magnitude larger than the required resolution (10^{-7} rad). This approximation is thus highly inappropriate for these kind of precision measurements and the full quantum calculations have to be used to interpret the signals.

The same calculations were performed for the situation in which the Doppler shift associated with the classical trajectory $\mathbf{k}_{eff} \cdot \boldsymbol{\xi}$ was completely compensated by the chirp of the laser frequency and the rotation was set to zero. The resulting difference in phase between the full quantum calculation and the semiclassical phase is given in Figure 7.8 by the line. The graph clearly shows that this improved compensation hardly has an effect on the validity of the semiclassical approximation.

7.7 Conclusions

In this chapter, the signal of a temporal Mach-Zehnder atom interferometer was calculated by a full integration of the Schrödinger equation. Other than in most calculations, this work takes into account the finite length of the laser pulses. The calculations show that the interferometer phase indeed changes with this pulse length, but also that the measured phase now depends on the shape and size of the initial atomic cloud. Although a final closed form solution was not obtained, the series of transformations that are derived in this section allow a series expansion that remains valid to the level of 10^{-16} (for pulses of $100 \mu\text{s}$) and greatly speed up the final numerical calculation of the signal.

Two main conclusions can be drawn from the calculations. The first conclusion is that the contrast of the considered interferometer (at zero temperature) is quite tolerant to the choice of the initial atomic cloud size. The range of initial cloud sizes that still give an interference signal, however, decreases rapidly with the total length of the interferometer sequence and the effective laser wavenumber. This has to be kept in mind when designing an even larger interferometer or when higher order photon processes are used that give a larger spatial separation between the two paths.

The second conclusion is that a semiclassical approach for calculating the interferometer signal gives an error in the calculated phase of approximately $1 \mu\text{rad}$, even when very short pulses of $1 \mu\text{s}$ are used. This means that in the considered interferometer, a semiclassical determination of \mathbf{g} from the signal is “only” accurate to 13 decimals, still two orders of magnitude from the intended accuracy. It is possible that a large component of the difference is common to all atom, such that this error cancels out in a difference measurement. Further research is necessary to investigate this possibility.

Although the results of the calculations are at this point too extensive for full symbolic results, the method that is explained in this chapter allows for a full quantum mechanical calculation of interferometer phases. It is an improvement on traditional semiclassical approaches and allows the study on new effects that influence the phases.

Appendix

A.1 Mathematical Tools

This appendix gives a list of operator identities that will be used in following sections. First, some general equations for two operators \hat{A} and \hat{B} [10, 11]:

$$e^{\hat{A}}\hat{B}e^{-\hat{A}} = \hat{B} + [\hat{A}, \hat{B}] + \frac{1}{2!}[\hat{A}, [\hat{A}, \hat{B}]] + \dots \quad (\text{A.1})$$

$$e^{\hat{A}+\hat{B}} = e^{\hat{A}}e^{\hat{B}}e^{-\frac{1}{2}[\hat{A}, \hat{B}]} \quad (\text{A.2})$$

$$\text{if } [\hat{A}, [\hat{A}, \hat{B}]] = [\hat{B}, [\hat{A}, \hat{B}]] = 0.$$

The following are some commutation relations for $\hat{\mathbf{r}}$ and $\hat{\mathbf{p}}$ in combination with arbitrary vectors \mathbf{v} and \mathbf{w} and matrix \vec{M} . These relations can readily be verified by writing all vectors out in their individual components and then using the well-known commutation relation between \hat{x} and \hat{p}_x :

$$[\mathbf{v} \cdot \hat{\mathbf{r}}, \mathbf{w} \cdot \hat{\mathbf{r}}] = 0 \quad (\text{A.3})$$

$$[\mathbf{v} \cdot \hat{\mathbf{p}}, \mathbf{w} \cdot \hat{\mathbf{p}}] = 0 \quad (\text{A.4})$$

$$[\mathbf{v} \cdot \hat{\mathbf{p}}, \mathbf{w} \cdot \hat{\mathbf{r}}] = -i\hbar\mathbf{v} \cdot \mathbf{w} \quad (\text{A.5})$$

$$[\hat{\mathbf{r}} \cdot \vec{M}\hat{\mathbf{r}}, \mathbf{v} \cdot \hat{\mathbf{r}}] = 0 \quad (\text{A.6})$$

$$[\hat{\mathbf{r}} \cdot \vec{M}\hat{\mathbf{p}}, \mathbf{v} \cdot \hat{\mathbf{r}}] = -i\hbar\hat{\mathbf{r}} \cdot \vec{M}\mathbf{v} \quad (\text{A.7})$$

$$[\hat{\mathbf{p}} \cdot \vec{M}\hat{\mathbf{p}}, \mathbf{v} \cdot \hat{\mathbf{r}}] = -i\hbar\mathbf{v} \cdot (\vec{M} + \vec{M}^T)\hat{\mathbf{p}} \quad (\text{A.8})$$

$$[\hat{\mathbf{r}} \cdot \vec{M}\hat{\mathbf{r}}, \mathbf{v} \cdot \hat{\mathbf{p}}] = i\hbar\mathbf{v} \cdot (\vec{M} + \vec{M}^T)\hat{\mathbf{r}} \quad (\text{A.9})$$

$$[\hat{\mathbf{r}} \cdot \vec{M}\hat{\mathbf{p}}, \mathbf{v} \cdot \hat{\mathbf{p}}] = i\hbar\mathbf{v} \cdot \vec{M}\hat{\mathbf{p}} \quad (\text{A.10})$$

$$[\hat{\mathbf{p}} \cdot \vec{M}\hat{\mathbf{p}}, \mathbf{v} \cdot \hat{\mathbf{p}}] = 0 \quad (\text{A.11})$$

$$[\hat{\mathbf{p}}, \vec{M}\hat{\mathbf{r}}] \equiv \hat{\mathbf{p}} \cdot \vec{M}\hat{\mathbf{r}} - (\vec{M}\hat{\mathbf{r}}) \cdot \hat{\mathbf{p}} = -i\hbar\text{Tr}(M) \quad (\text{A.12})$$

Then using Equation A.1 and the above mentioned commutation relations, we can derive the following transformations for $\hat{\mathbf{r}}$

$$e^{\mathbf{v} \cdot \hat{\mathbf{r}}}\hat{\mathbf{r}}e^{-\mathbf{v} \cdot \hat{\mathbf{r}}} = \hat{\mathbf{r}} \quad (\text{A.13})$$

$$e^{\mathbf{v} \cdot \hat{\mathbf{p}}}\hat{\mathbf{r}}e^{-\mathbf{v} \cdot \hat{\mathbf{p}}} = \hat{\mathbf{r}} - i\hbar\mathbf{v} \quad (\text{A.14})$$

$$e^{\hat{\mathbf{r}} \cdot \vec{M}\hat{\mathbf{r}}}\hat{\mathbf{r}}e^{-\hat{\mathbf{r}} \cdot \vec{M}\hat{\mathbf{r}}} = \hat{\mathbf{r}} \quad (\text{A.15})$$

$$e^{\hat{\mathbf{p}} \cdot \vec{M}\hat{\mathbf{p}}}\hat{\mathbf{r}}e^{-\hat{\mathbf{p}} \cdot \vec{M}\hat{\mathbf{p}}} = \hat{\mathbf{r}} - i\hbar(\vec{M} + \vec{M}^T)\hat{\mathbf{p}} \quad (\text{A.16})$$

$$e^{\hat{\mathbf{r}} \cdot \vec{M}\hat{\mathbf{p}}}\hat{\mathbf{r}}e^{-\hat{\mathbf{r}} \cdot \vec{M}\hat{\mathbf{p}}} = e^{-i\hbar\vec{M}^T}\hat{\mathbf{r}} \quad (\text{A.17})$$

and for $\hat{\mathbf{p}}$:

$$e^{\mathbf{v} \cdot \hat{\mathbf{r}}}\hat{\mathbf{p}}e^{-\mathbf{v} \cdot \hat{\mathbf{r}}} = \hat{\mathbf{p}} + i\hbar\mathbf{v} \quad (\text{A.18})$$

$$e^{\mathbf{v}\cdot\hat{\mathbf{p}}}\hat{\mathbf{p}}e^{-\mathbf{v}\cdot\hat{\mathbf{p}}} = \hat{\mathbf{p}} \quad (\text{A.19})$$

$$e^{\hat{\mathbf{r}}\cdot\vec{M}\hat{\mathbf{r}}}\hat{\mathbf{p}}e^{-\hat{\mathbf{r}}\cdot\vec{M}\hat{\mathbf{r}}} = \hat{\mathbf{p}} + i\hbar(\vec{M} + \vec{M}^T)\hat{\mathbf{r}} \quad (\text{A.20})$$

$$e^{\hat{\mathbf{p}}\cdot\vec{M}\hat{\mathbf{p}}}\hat{\mathbf{p}}e^{-\hat{\mathbf{p}}\cdot\vec{M}\hat{\mathbf{p}}} = \hat{\mathbf{p}} \quad (\text{A.21})$$

$$e^{\hat{\mathbf{r}}\cdot\vec{M}\hat{\mathbf{p}}}\hat{\mathbf{p}}e^{-\hat{\mathbf{r}}\cdot\vec{M}\hat{\mathbf{p}}} = e^{i\hbar\vec{M}\hat{\mathbf{r}}}\hat{\mathbf{p}}. \quad (\text{A.22})$$

Finally, using these transformation rules we get the following commutation relation between an operator that is an arbitrary function of $\hat{\mathbf{r}}$ and $\hat{\mathbf{p}}$ and an operator with a linear combination of $\hat{\mathbf{r}}$ and $\hat{\mathbf{p}}$ in an exponential:

$$\begin{aligned} e^{\mathbf{v}\cdot\hat{\mathbf{r}}+\mathbf{w}\cdot\hat{\mathbf{p}}}f(\hat{\mathbf{r}},\hat{\mathbf{p}}) &= e^{\mathbf{v}\cdot\hat{\mathbf{r}}+\mathbf{w}\cdot\hat{\mathbf{p}}}f(\hat{\mathbf{r}},\hat{\mathbf{p}})e^{-\mathbf{v}\cdot\hat{\mathbf{r}}-\mathbf{w}\cdot\hat{\mathbf{p}}}e^{\mathbf{v}\cdot\hat{\mathbf{r}}+\mathbf{w}\cdot\hat{\mathbf{p}}} \\ &= f(\hat{\mathbf{r}}-i\hbar\mathbf{w},\hat{\mathbf{p}}+i\hbar\mathbf{v})e^{\mathbf{v}\cdot\hat{\mathbf{r}}+\mathbf{w}\cdot\hat{\mathbf{p}}}. \end{aligned} \quad (\text{A.23})$$

A.2 Elimination of the external Hamiltonian

Using the transformation rules that were derived in the previous section, it is possible to transform the Schrödinger equation to an interaction picture in which the motion of the external Hamiltonian has been eliminated. Consider the external Hamiltonian (Eq. 7.3):

$$\hat{H}_{ext} = \frac{\hat{\mathbf{p}}^2}{2m} - m\mathbf{g}\cdot\hat{\mathbf{r}} - \frac{m}{2}\hat{\mathbf{r}}\cdot\vec{\Gamma}\hat{\mathbf{r}} - (\hat{\mathbf{r}} + \mathbf{R})\cdot\vec{\Omega}\hat{\mathbf{p}} + V(\hat{\mathbf{r}}). \quad (\text{A.24})$$

We will now perform a series of transformations to eliminate the terms of the external Hamiltonian one by one analogous to [4] and [5]. The new effective Hamiltonian after each transformation \hat{U} is calculated by

$$\hat{H}_{new} = \hat{U}^{-1}\left(\hat{H}_{old}\hat{U} - i\hbar\frac{d}{dt}\hat{U}\right) \quad (\text{A.25})$$

$$|\Psi_{old}\rangle = \hat{U}|\Psi_{new}\rangle. \quad (\text{A.26})$$

To keep the size of the equations limited, we will first ignore the potential $V(\hat{\mathbf{r}})$ and first derive the transformations that can eliminate the external Hamiltonian. Later, in Section A.3, the effect of these transformations on the potential is derived.

First we take the transformation

$$\hat{U}_1 = e^{-\frac{i}{\hbar}\boldsymbol{\xi}\cdot\hat{\mathbf{p}}}, \quad (\text{A.27})$$

which is equivalent to a translation over $\boldsymbol{\xi}$ (Eq. A.14). We will see later that a specific choice of $\boldsymbol{\xi}$ eliminates the linear terms in $\hat{\mathbf{r}}$. The new effective Hamiltonian is:

$$\begin{aligned} \hat{H}_1 &= \frac{\hat{\mathbf{p}}^2}{2m} - m\mathbf{g}\cdot(\hat{\mathbf{r}} + \boldsymbol{\xi}) - \frac{m}{2}(\hat{\mathbf{r}} + \boldsymbol{\xi})\cdot\vec{\Gamma}(\hat{\mathbf{r}} + \boldsymbol{\xi}) \\ &\quad - ((\hat{\mathbf{r}} + \boldsymbol{\xi}) + \mathbf{R})\cdot\vec{\Omega}\hat{\mathbf{p}} - \dot{\boldsymbol{\xi}}\cdot\hat{\mathbf{p}}, \end{aligned} \quad (\text{A.28})$$

where the dot over a symbol indicates a time derivative. Then we apply the transformation

$$\hat{U}_2 = e^{\frac{i}{\hbar}\boldsymbol{\zeta}\cdot\hat{\mathbf{r}}}, \quad (\text{A.29})$$

which gives a momentum boost ζ to the system. After combining all terms with equal powers of $\hat{\mathbf{r}}$ and $\hat{\mathbf{p}}$ we get

$$\begin{aligned} \hat{H}_2 = & \frac{\hat{\mathbf{p}}^2}{2m} - \frac{m}{2} \hat{\mathbf{r}} \cdot \vec{\Gamma} \hat{\mathbf{r}} - \hat{\mathbf{r}} \cdot \vec{\Omega} \hat{\mathbf{p}} + \\ & \left(\frac{\zeta}{m} - \vec{\Omega}^T \boldsymbol{\xi} - \vec{\Omega}^T \mathbf{R} - \dot{\boldsymbol{\xi}} \right) \cdot \hat{\mathbf{p}} + \\ & \left(-m\mathbf{g} - \frac{m}{2} (\vec{\Gamma} + \vec{\Gamma}^T) \boldsymbol{\xi} - \vec{\Omega} \zeta + \dot{\zeta} \right) \cdot \hat{\mathbf{r}} + \\ & \left(\frac{\zeta^2}{2m} - m\mathbf{g} \cdot \boldsymbol{\xi} - \frac{m}{2} \boldsymbol{\xi} \cdot \vec{\Gamma} \boldsymbol{\xi} - (\boldsymbol{\xi} + \mathbf{R}) \cdot \vec{\Omega} \zeta - \dot{\boldsymbol{\xi}} \cdot \zeta \right). \end{aligned} \quad (\text{A.30})$$

We can eliminate the terms that are linear in $\hat{\mathbf{r}}$ and $\hat{\mathbf{p}}$ by choosing

$$\dot{\boldsymbol{\xi}} = \frac{\zeta}{m} + \vec{\Omega}^T \boldsymbol{\xi} + \vec{\Omega}^T \mathbf{R} \quad (\text{A.31})$$

$$\dot{\zeta} = m\mathbf{g} + \frac{m}{2} (\vec{\Gamma} + \vec{\Gamma}^T) \boldsymbol{\xi} + \vec{\Omega} \zeta. \quad (\text{A.32})$$

Closer inspection of these choices reveals that we can write them as

$$\dot{\boldsymbol{\xi}} = \nabla_{\hat{\mathbf{p}}} \hat{H}_{ext}(\hat{\mathbf{r}}, \hat{\mathbf{p}})|_{\hat{\mathbf{r}}=\boldsymbol{\xi}, \hat{\mathbf{p}}=\zeta} \quad (\text{A.33})$$

$$\dot{\zeta} = -\nabla_{\hat{\mathbf{r}}} \hat{H}_{ext}(\hat{\mathbf{r}}, \hat{\mathbf{p}})|_{\hat{\mathbf{r}}=\boldsymbol{\xi}, \hat{\mathbf{p}}=\zeta}. \quad (\text{A.34})$$

In other words, the transformations eliminate the linear terms in $\hat{\mathbf{r}}$ and $\hat{\mathbf{p}}$ if $\boldsymbol{\xi}$ and ζ in these transformations obey the Hamilton equations, given by the external Hamiltonian and thus follow a classical trajectory. Then with the identification of $\boldsymbol{\xi}$ with the classical position and ζ with the classical momentum, the term in Equation A.30 that is independent of $\hat{\mathbf{r}}$ and $\hat{\mathbf{p}}$ is equal to the classical Lagrangian evaluated over the classical trajectory:

$$L_{cl} = -\frac{\zeta^2}{2m} + m\mathbf{g} \cdot \boldsymbol{\xi} + \frac{m}{2} \boldsymbol{\xi} \cdot \vec{\Gamma} \boldsymbol{\xi} + (\boldsymbol{\xi} + \mathbf{R}) \cdot \vec{\Omega} \zeta + \dot{\boldsymbol{\xi}} \cdot \zeta. \quad (\text{A.35})$$

This term can then be eliminated by the transformation

$$\hat{U}_3 = e^{\frac{i}{\hbar} \int_0^t L_{cl} dt}, \quad (\text{A.36})$$

leaving

$$\hat{H}_3 = \frac{\hat{\mathbf{p}}^2}{2m} - \frac{m}{2} \hat{\mathbf{r}} \cdot \vec{\Gamma} \hat{\mathbf{r}} - \hat{\mathbf{r}} \cdot \vec{\Omega} \hat{\mathbf{p}}. \quad (\text{A.37})$$

Note that we do not have to apply initial conditions on the exact form of $\boldsymbol{\xi}$ and ζ to make the eliminations work. These terms alone therefore do not necessarily describe the trajectory of the atom under consideration.

To remove the remaining terms of the external Hamiltonian, we start with the transformation

$$\hat{U}_4 = e^{\frac{i}{\hbar} \hat{\mathbf{r}} \cdot \vec{\lambda} \hat{\mathbf{r}}}. \quad (\text{A.38})$$

In the same manner as before, we leave $\vec{\lambda}$ free for the moment, but we will see that a suitable choice will eliminate another term in the Schrödinger equation. Applying this transformation to Equation A.37 gives

$$\begin{aligned}
\hat{H}_4 &= \frac{1}{2m}(\hat{\mathbf{p}} + (\vec{\lambda} + \vec{\lambda}^T)\hat{\mathbf{r}})^2 - \frac{m}{2}\hat{\mathbf{r}} \cdot \vec{\Gamma}\hat{\mathbf{r}} - \hat{\mathbf{r}} \cdot \vec{\Omega}(\hat{\mathbf{p}} + (\vec{\lambda} + \vec{\lambda}^T)\hat{\mathbf{r}}) + \hat{\mathbf{r}} \cdot \dot{\vec{\lambda}}\hat{\mathbf{r}} \\
&= \frac{\hat{\mathbf{p}}^2}{2m} + \hat{\mathbf{r}} \cdot \left(\frac{\vec{\lambda} + \vec{\lambda}^T}{2m} - \vec{\Omega} \right) \hat{\mathbf{p}} + \hat{\mathbf{p}} \cdot \frac{\vec{\lambda} + \vec{\lambda}^T}{2m} \hat{\mathbf{r}} \\
&\quad + \hat{\mathbf{r}} \cdot \left(\frac{(\vec{\lambda} + \vec{\lambda}^T)^2}{2m} - \frac{m}{2}\vec{\Gamma} - \vec{\Omega}(\vec{\lambda} + \vec{\lambda}^T) + \dot{\vec{\lambda}} \right) \hat{\mathbf{r}}.
\end{aligned} \tag{A.39}$$

Then, if we choose $\vec{\lambda}$ such that

$$\dot{\vec{\lambda}} = -\frac{(\vec{\lambda} + \vec{\lambda}^T)^2}{2m} + \frac{m}{2}\vec{\Gamma} + \vec{\Omega}(\vec{\lambda} + \vec{\lambda}^T) \tag{A.40}$$

we obtain

$$\hat{H}_4 = \frac{\hat{\mathbf{p}}^2}{2m} + \hat{\mathbf{r}} \cdot \left(\frac{\vec{\lambda} + \vec{\lambda}^T}{2m} - \vec{\Omega} \right) \hat{\mathbf{p}} + \hat{\mathbf{p}} \cdot \frac{\vec{\lambda} + \vec{\lambda}^T}{2m} \hat{\mathbf{r}}. \tag{A.41}$$

Next, the transformation

$$\hat{U}_5 = e^{-\frac{i}{\hbar}\hat{\mathbf{p}} \cdot \vec{\mu}} \tag{A.42}$$

$$\begin{aligned}
\hat{H}_5 &= \frac{\hat{\mathbf{p}}^2}{2m} + (\hat{\mathbf{r}} + (\vec{\mu} + \vec{\mu}^T)\hat{\mathbf{p}}) \cdot \left(\frac{\vec{\lambda} + \vec{\lambda}^T}{2m} - \vec{\Omega} \right) \hat{\mathbf{p}} \\
&\quad + \hat{\mathbf{p}} \cdot \frac{\vec{\lambda} + \vec{\lambda}^T}{2m} (\hat{\mathbf{r}} + (\vec{\mu} + \vec{\mu}^T)\hat{\mathbf{p}}) - \hat{\mathbf{p}} \cdot \dot{\vec{\mu}}\hat{\mathbf{p}} \\
&= \hat{\mathbf{p}} \cdot \left(\frac{1}{2m} + (\vec{\mu} + \vec{\mu}^T) \left(\frac{\vec{\lambda} + \vec{\lambda}^T}{2m} - \vec{\Omega} \right) + \frac{\vec{\lambda} + \vec{\lambda}^T}{2m}(\vec{\mu} + \vec{\mu}^T) - \dot{\vec{\mu}} \right) \hat{\mathbf{p}} \\
&\quad + \hat{\mathbf{r}} \cdot \left(\frac{\vec{\lambda} + \vec{\lambda}^T}{2m} - \vec{\Omega} \right) \hat{\mathbf{p}} + \hat{\mathbf{p}} \cdot \left(\frac{\vec{\lambda} + \vec{\lambda}^T}{2m} \right) \hat{\mathbf{r}} \\
&= \hat{\mathbf{r}} \cdot \left(\frac{\vec{\lambda} + \vec{\lambda}^T}{2m} - \vec{\Omega} \right) \hat{\mathbf{p}} + \hat{\mathbf{p}} \cdot \left(\frac{\vec{\lambda} + \vec{\lambda}^T}{2m} \right) \hat{\mathbf{r}}
\end{aligned} \tag{A.43}$$

if we choose for the following relation for $\vec{\mu}$

$$\dot{\vec{\mu}} = \frac{1}{2m} + (\vec{\mu} + \vec{\mu}^T) \left(\frac{\vec{\lambda} + \vec{\lambda}^T}{2m} - \vec{\Omega} \right) + \frac{\vec{\lambda} + \vec{\lambda}^T}{2m}(\vec{\mu} + \vec{\mu}^T). \tag{A.44}$$

Then after commutation of $\hat{\mathbf{r}}$ and $\hat{\mathbf{p}}$ we get

$$\hat{H}_5 = \hat{\mathbf{r}} \cdot \left(\frac{\vec{\lambda} + \vec{\lambda}^T}{m} - \vec{\Omega} \right) \hat{\mathbf{p}} - i\hbar Tr \left(\frac{\vec{\lambda} + \vec{\lambda}^T}{2m} \right) \quad (\text{A.45})$$

and the final transformation

$$\hat{U}_6 = e^{-\frac{i}{\hbar} \int_0^t dt' \left[\hat{\mathbf{r}} \cdot \left(\frac{\vec{\lambda} + \vec{\lambda}^T}{m} - \vec{\Omega} \right) \hat{\mathbf{p}} - i\hbar Tr \left(\frac{\vec{\lambda} + \vec{\lambda}^T}{2m} \right) \right]} \quad (\text{A.46})$$

leaves

$$\hat{H}_6 = 0 \quad (\text{A.47})$$

A.3 Coordinate Transformations

Now, let's take a look at the effect of the transformations of Section A.2 on the potential V . If we take the matrices $\vec{\lambda}$ and $\vec{\mu}$ symmetric, we can summarize the effect of each subsequent transformation on $\hat{\mathbf{r}}$ and $\hat{\mathbf{p}}$ in Table A.1. In this table two columns are shown with combinations of $\hat{\mathbf{r}}$ and $\hat{\mathbf{p}}$. One column starts with $\hat{\mathbf{r}}$ and the other with $\hat{\mathbf{p}}$. On each subsequent row, the result is given that is obtained when the transformation $\hat{U}^{-1}(\dots)\hat{U}$ that is indicated in the first column is applied to the result in the cell above. The lowest entry in the column of $\hat{\mathbf{r}}$, for example, indicates the result when all 6 transformations have been applied to $\hat{\mathbf{r}}$. We see that these 6 transformations transform both $\hat{\mathbf{r}}$ and $\hat{\mathbf{p}}$ into a superposition of the two with coefficients (matrices) that we shall call $\vec{A}, \vec{B}, \vec{C}$ and \vec{D} .

Under the assumption that $\vec{\Omega}$ anticommutes with both $\vec{\lambda}$ and $\vec{\mu}$ ($\vec{\Omega}\vec{\lambda} = -\vec{\lambda}\vec{\Omega}$) and using equations A.40 and A.44 it is straightforward to verify that the evolution of the matrices $\vec{A}, \vec{B}, \vec{C}$ and \vec{D} follows

$$\frac{d}{dt} \begin{pmatrix} \vec{A} & \vec{B} \\ \vec{C} & \vec{D} \end{pmatrix} = \vec{M} \begin{pmatrix} \vec{A} & \vec{B} \\ \vec{C} & \vec{D} \end{pmatrix} \quad (\text{A.48})$$

$$\vec{M} \equiv \begin{pmatrix} \vec{\Omega} & 1 \\ \vec{\Gamma} & \vec{\Omega} \end{pmatrix} \quad (\text{A.49})$$

and we can rewrite Equations A.31 and A.32

$$\frac{d}{dt} \begin{pmatrix} \boldsymbol{\xi} \\ \boldsymbol{\zeta}/m \end{pmatrix} = \vec{M} \begin{pmatrix} \boldsymbol{\xi} \\ \boldsymbol{\zeta}/m \end{pmatrix} + \begin{pmatrix} \vec{\Omega}\mathbf{R} \\ \mathbf{g} \end{pmatrix}. \quad (\text{A.50})$$

Initial conditions for the matrices arise from the condition that at $t=0$ the transformations should reduce to the identity transformation (the atoms did not have time to move):

$$\begin{pmatrix} \vec{A} & \vec{B} \\ \vec{C} & \vec{D} \end{pmatrix}_{t=0} = \begin{pmatrix} 1 & 0 \\ 0 & 1 \end{pmatrix} \quad (\text{A.51})$$

$$\begin{pmatrix} \boldsymbol{\xi} \\ \boldsymbol{\zeta}/m \end{pmatrix}_{t=0} = \begin{pmatrix} 0 \\ 0 \end{pmatrix}. \quad (\text{A.52})$$

trans-formation	result	
	$\hat{\mathbf{r}}$	$\hat{\mathbf{p}}$
\hat{U}_1	$\hat{\mathbf{r}} + \boldsymbol{\xi}$	$\hat{\mathbf{p}}$
\hat{U}_2	$\hat{\mathbf{r}} + \boldsymbol{\xi}$	$\hat{\mathbf{p}} + \boldsymbol{\zeta}$
\hat{U}_3	$\hat{\mathbf{r}} + \boldsymbol{\xi}$	$\hat{\mathbf{p}} + \boldsymbol{\zeta}$
\hat{U}_4	$\hat{\mathbf{r}} + \boldsymbol{\xi}$	$2\vec{\lambda}\hat{\mathbf{r}} + \hat{\mathbf{p}} + \boldsymbol{\zeta}$
\hat{U}_5	$\hat{\mathbf{r}} + 2\vec{\mu}\hat{\mathbf{p}} + \boldsymbol{\xi}$	$2\vec{\lambda}\hat{\mathbf{r}} + (1 + 4\vec{\lambda}\vec{\mu})\hat{\mathbf{p}} + \boldsymbol{\zeta}$
\hat{U}_6	$\exp\left[\int_0^t dt' \left(2\vec{\lambda}/m + \vec{\Omega}\right)\right] \hat{\mathbf{r}}$ $+ 2\vec{\mu} \exp\left[-\int_0^t dt' \left(2\vec{\lambda}/m - \vec{\Omega}\right)\right] \hat{\mathbf{p}}$ $+ \boldsymbol{\xi}$ $\equiv \vec{A}\hat{\mathbf{r}} + \frac{1}{m}\vec{B}\hat{\mathbf{p}} + \boldsymbol{\xi}$	$2\vec{\lambda} \exp\left[\int_0^t dt' \left(2\vec{\lambda}/m + \vec{\Omega}\right)\right] \hat{\mathbf{r}}$ $+ (1 + 4\vec{\lambda}\vec{\mu}) \exp\left[-\int_0^t dt' \left(2\vec{\lambda}/m - \vec{\Omega}\right)\right] \hat{\mathbf{p}}$ $+ \boldsymbol{\zeta}$ $\equiv m\vec{C}\hat{\mathbf{r}} + \vec{D}\hat{\mathbf{p}} + \boldsymbol{\zeta}$

Table A.1: Effect of the six transformations that are subsequently applied to $\hat{\mathbf{r}}$ (middle column) and to $\hat{\mathbf{p}}$ (right column). The table gives the result when the transformation is applied to the result of the previous (entry above).

In Table A.1 only the effect of the transformations on $\hat{\mathbf{r}}$ and $\hat{\mathbf{p}}$ is given. It is however straightforward to show that we get the same substitutions for any function of $\hat{\mathbf{r}}$ and $\hat{\mathbf{p}}$ by expanding this function in a Taylor series and inserting $1 = \hat{U}\hat{U}^{-1}$ where necessary:

$$\hat{U}^{-1}V(\hat{\mathbf{r}})\hat{U} = \hat{U}^{-1} \sum_i (\mathbf{v}_i \cdot \hat{\mathbf{r}})^i \hat{U} = \sum_i \left(\mathbf{v}_i \cdot \left(\hat{U}^{-1}\hat{\mathbf{r}}\hat{U} \right) \right)^i = V\left(\hat{U}^{-1}\hat{\mathbf{r}}\hat{U} \right). \quad (\text{A.53})$$

A.4 Laser Interaction

The laser interaction Hamiltonian in the two level approximation and in rotating wave coordinates is (Eq. 7.15)

$$\hat{H}'_{laser}(\mathbf{r}) = \frac{\hbar}{2} \begin{pmatrix} 0 & \Omega_R e^{i\hat{\phi}(t)} \\ \Omega_R e^{-i\hat{\phi}(t)} & 0 \end{pmatrix}. \quad (\text{A.54})$$

We start by taking out the relative phase evolution of the excited state:

$$\hat{U}_7 = \begin{pmatrix} e^{i\hat{\phi}(t)} & 0 \\ 0 & 1 \end{pmatrix} \quad (\text{A.55})$$

$$\Downarrow$$

$$\hat{H}_7 = \hbar \begin{pmatrix} \frac{d\hat{\phi}(t)}{dt} & \Omega_R/2 \\ \Omega_R/2 & 0 \end{pmatrix}. \quad (\text{A.56})$$

Next we go to a system that rotates with the unperturbed Rabi oscillation starting when the laser pulse is turned on at t_1 ($\tau = t - t_1$)

$$\hat{U}_8 = e^{-\frac{i}{2} \begin{pmatrix} 0 & \Omega_R \\ \Omega_R & 0 \end{pmatrix} \tau} = \begin{pmatrix} \cos(\Omega_R \tau/2) & -i \sin(\Omega_R \tau/2) \\ -i \sin(\Omega_R \tau/2) & \cos(\Omega_R \tau/2) \end{pmatrix} \quad (\text{A.57})$$

$$\downarrow$$

$$\hat{H}_8 = \hbar \frac{d\hat{\phi}(t)}{dt} \begin{pmatrix} \cos^2(\Omega_R \tau/2) & -i \cos(\Omega_R \tau/2) \sin(\Omega_R \tau/2) \\ i \cos(\Omega_R \tau/2) \sin(\Omega_R \tau/2) & \sin^2(\Omega_R \tau/2) \end{pmatrix}. \quad (\text{A.58})$$

The evolution of the wavefunction relative to this ideal Rabi oscillation is obtained by integration of the Schrödinger equation. The formal solution is given by the evolution operator

$$\hat{U}_9 = \mathcal{T} e^{-\frac{i}{\hbar} \int_{t_0}^{t_0+\tau} \hat{H}_8(t') dt'} \quad (\text{A.59})$$

where \mathcal{T} indicates a time ordering operator. For slow changes of the phase $\hat{\phi}(t)$ we can use a Dyson series expansion for the evolution operator

$$\hat{U}_9(t_0, \tau) = 1 + \frac{1}{i\hbar} \int_{t_0}^{t_0+\tau} \hat{H}_8(t') dt' + \frac{1}{(i\hbar)^2} \int_{t_0}^{t_0+\tau} dt' \hat{H}_8(t') \int_{t_0}^{t_0+t'} dt'' \hat{H}_8(t'') + \dots \quad (\text{A.60})$$

For the moment, however, we shall leave it unevaluated. To get the laser pulse evolution operator in the original coordinate system of Equation 7.15 we have to apply the inverse transformations at the beginning and at the end of the pulse

$$\begin{aligned} \hat{U}_{laser}(t_0, \tau) &= \hat{U}_7(t_0 + \tau) \hat{U}_8(\tau) \hat{U}_9(t_0, \tau) \hat{U}_8^{-1}(0) \hat{U}_7^{-1}(t_0) \\ &= \begin{pmatrix} e^{i\hat{\phi}(t_0+\tau)} & 0 \\ 0 & 1 \end{pmatrix} \begin{pmatrix} \hat{U}_{ee}(t_0, \tau) & \hat{U}_{eg}(t_0, \tau) \\ \hat{U}_{ge}(t_0, \tau) & \hat{U}_{gg}(t_0, \tau) \end{pmatrix} \begin{pmatrix} e^{-i\hat{\phi}(t_0)} & 0 \\ 0 & 0 \end{pmatrix} \\ &= \begin{pmatrix} e^{i\hat{\phi}(t_0+\tau)} \hat{U}_{ee}(t_0, \tau) e^{-i\hat{\phi}(t_0)} & e^{i\hat{\phi}(t_0+\tau)} \hat{U}_{eg}(t_0, \tau) \\ \hat{U}_{ge}(t_0, \tau) e^{-i\hat{\phi}(t_0)} & \hat{U}_{gg}(t_0, \tau) \end{pmatrix}. \end{aligned} \quad (\text{A.61})$$

Here we only wrote down the laser phase explicitly and summarized the effect of \hat{U}_8 and \hat{U}_9 in the functions \hat{U}_{ij} .

A.5 Atom Interferometer

In the two path approximation the total interferometer evolution operator is given by

$$\begin{aligned} \hat{U}_{MZ} &= \hat{U}_{laser}(2T + 3\tau, \tau) \hat{U}_{laser}(T + \tau, 2\tau) \hat{U}_{laser}(0, \tau) \\ &= \begin{pmatrix} e^{i\hat{\phi}_3^+} \hat{U}_{ee}^3 e^{-i\hat{\phi}_3^0} & e^{i\hat{\phi}_3^+} \hat{U}_{eg}^3 \\ \hat{U}_{ge}^3 e^{-i\hat{\phi}_3^0} & \hat{U}_{gg}^3 \end{pmatrix} \begin{pmatrix} 0 & e^{i\hat{\phi}_2^+} \hat{U}_{eg}^2 \\ \hat{U}_{ge}^2 e^{-i\hat{\phi}_2^0} & 0 \end{pmatrix} \begin{pmatrix} e^{i\hat{\phi}_1^+} \hat{U}_{ee}^1 e^{-i\hat{\phi}_1^0} & e^{i\hat{\phi}_1^+} \hat{U}_{eg}^1 \\ \hat{U}_{ge}^1 e^{-i\hat{\phi}_1^0} & \hat{U}_{gg}^1 \end{pmatrix} \end{aligned}$$

$$= \begin{pmatrix} e^{i\hat{\phi}_3^+} \hat{U}_{ee}^3 e^{-i\hat{\phi}_3^0} e^{i\hat{\phi}_2^+} \hat{U}_{eg}^2 \hat{U}_{ge}^1 e^{-i\hat{\phi}_1^0} & e^{i\hat{\phi}_3^+} \hat{U}_{ee}^3 e^{-i\hat{\phi}_3^0} e^{i\hat{\phi}_2^+} \hat{U}_{eg}^2 \hat{U}_{gg}^1 \\ + e^{i\hat{\phi}_3^+} \hat{U}_{eg}^3 \hat{U}_{ge}^2 e^{-i\hat{\phi}_2^0} e^{i\hat{\phi}_1^+} \hat{U}_{ee}^1 e^{-i\hat{\phi}_1^0} & + e^{i\hat{\phi}_3^+} \hat{U}_{eg}^3 \hat{U}_{ge}^2 e^{-i\hat{\phi}_2^0} e^{i\hat{\phi}_1^+} \hat{U}_{eg}^1 \end{pmatrix} \quad (\text{A.62})$$

$$t_1 = 0, \quad t_2 = T + \tau, \quad t_3 = 2T + 3\tau \quad (\text{A.63})$$

$$\tau_1 = \tau_3 = \tau, \quad \tau_2 = 2\tau \quad (\text{A.64})$$

$$\hat{U}_{ij}^k = \hat{U}_{ij}(t_k, \tau_k, \hat{\mathbf{r}}, \hat{\mathbf{p}}) \quad (\text{A.65})$$

$$\hat{\phi}_k^0 = \hat{\phi}(t_k, \hat{\mathbf{r}}, \hat{\mathbf{p}}), \quad \hat{\phi}_k^+ = \hat{\phi}(t_k + \tau_k, \hat{\mathbf{r}}, \hat{\mathbf{p}}). \quad (\text{A.66})$$

The operator that describes the transition from ground state to ground state is

$$\begin{aligned} \hat{U}_{MZ,gg} &= \hat{U}_{ge}^3(\hat{\mathbf{r}}, \hat{\mathbf{p}}) e^{-i\hat{\phi}_3^0} e^{i\hat{\phi}_2^+} \hat{U}_{eg}^2(\hat{\mathbf{r}}, \hat{\mathbf{p}}) \hat{U}_{gg}^1(\hat{\mathbf{r}}, \hat{\mathbf{p}}) \\ &\quad + \hat{U}_{gg}^3(\hat{\mathbf{r}}, \hat{\mathbf{p}}) \hat{U}_{ge}^2(\hat{\mathbf{r}}, \hat{\mathbf{p}}) e^{-i\hat{\phi}_2^0} e^{i\hat{\phi}_1^+} \hat{U}_{eg}^1(\hat{\mathbf{r}}, \hat{\mathbf{p}}), \end{aligned} \quad (\text{A.67})$$

where we have added the $\hat{\mathbf{r}}$ and $\hat{\mathbf{p}}$ dependence in the functions \hat{U}_{ij} explicitly, because they have to be replaced when the exponentials in $\hat{U}_{MZ,gg}$ are rearranged. To get one single phase operator we combine the exponential terms using Eq. A.23

$$\begin{aligned} \hat{U}_{MZ,gg} &= e^{-i\hat{\phi}_3^0} e^{i\hat{\phi}_2^+} \hat{U}_{ge}^3 \left(\hat{\mathbf{r}} + \hbar \left(\vec{B}_3^0 - \vec{B}_2^+ \right)^T \mathbf{k}_{eff}, \hat{\mathbf{p}} - \hbar \left(\vec{A}_3^0 - \vec{A}_2^+ \right)^T \mathbf{k}_{eff} \right) \\ &\quad \times \hat{U}_{eg}^2(\hat{\mathbf{r}}, \hat{\mathbf{p}}) \hat{U}_{gg}^1(\hat{\mathbf{r}}, \hat{\mathbf{p}}) \\ &\quad + e^{-i\hat{\phi}_2^0} e^{i\hat{\phi}_1^+} \hat{U}_{gg}^3 \left(\hat{\mathbf{r}} + \hbar \left(\vec{B}_2^0 - \vec{B}_1^+ \right)^T \mathbf{k}_{eff}, \hat{\mathbf{p}} - \hbar \left(\vec{A}_2^0 - \vec{A}_1^+ \right)^T \mathbf{k}_{eff} \right) \\ &\quad \times \hat{U}_{ge}^2 \left(\hat{\mathbf{r}} + \hbar \left(\vec{B}_2^0 - \vec{B}_1^+ \right)^T \mathbf{k}_{eff}, \hat{\mathbf{p}} - \hbar \left(\vec{A}_2^0 - \vec{A}_1^+ \right)^T \mathbf{k}_{eff} \right) \hat{U}_{eg}^1(\hat{\mathbf{r}}, \hat{\mathbf{p}}) \\ &\equiv e^{-i\hat{\phi}_3^0} e^{i\hat{\phi}_2^+} \hat{g}_1 + e^{-i\hat{\phi}_2^0} e^{i\hat{\phi}_1^+} \hat{g}_2 \end{aligned} \quad (\text{A.68})$$

$$\vec{A}_k^0 = \vec{A}(t_k), \quad \vec{A}_k^+ = \vec{A}(t_k + \tau_k) \quad (\text{A.69})$$

$$\vec{B}_k^0 = \vec{B}(t_k), \quad \vec{B}_k^+ = \vec{B}(t_k + \tau_k). \quad (\text{A.70})$$

The operators \hat{g}_1 and \hat{g}_2 describe the amplitudes and small phase corrections of the two paths of the interferometer. Using Equation A.2 we get an expression for the interferometer phase

$$\hat{U}_{MZ,gg} = e^{-i\hat{\phi}_3^0} e^{i\hat{\phi}_2^+} \left[\hat{g}_1 + e^{-i\hat{\phi}_{MZ}} \hat{g}_2 \right] \quad (\text{A.71})$$

$$\begin{aligned} \hat{\phi}_{MZ} &= \hat{\phi}_1^+ - \hat{\phi}_2^0 - \hat{\phi}_2^+ + \hat{\phi}_3^0 \\ &\quad - \frac{i}{2} \left[[\hat{\phi}_2^+, \hat{\phi}_3^0] + [\hat{\phi}_2^0, \hat{\phi}_1^+] - [\hat{\phi}_2^+ - \hat{\phi}_3^0, \hat{\phi}_1^+ - \hat{\phi}_2^0] \right]. \end{aligned} \quad (\text{A.72})$$

A.5.1 Short Pulse Limit

In the short pulse limit $\tau \rightarrow 0$ we can drop the superscripts 0 and + in the phase operators and simplify the interferometer phase to

$$\hat{\phi}_{MZ,sp} = \hat{\phi}_1 + \hat{\phi}_3 - 2\hat{\phi}_2 - \frac{i}{2}[\hat{\phi}_1, \hat{\phi}_3 - 2\hat{\phi}_2]. \quad (\text{A.73})$$

This can be simplified further by filling in the expression for ϕ Eq. 7.17:

$$\begin{aligned} [\phi_1, \phi_3 - 2\phi_2] &= [\phi_1, \mathbf{k}_{eff} \cdot (\vec{A}_3 - 2\vec{A}_2)\hat{\mathbf{r}}] + [\phi_1, \mathbf{k}_{eff} \cdot (\vec{B}_3 - 2\vec{B}_2)\hat{\mathbf{p}}] \\ &\quad + [\phi_1, \mathbf{k}_{eff} \cdot (\boldsymbol{\xi}_3 - 2\boldsymbol{\xi}_2)] \\ &= [\mathbf{k}_{eff} \cdot \vec{A}_1\hat{\mathbf{r}}, \mathbf{k}_{eff} \cdot (\vec{B}_3 - 2\vec{B}_2)\hat{\mathbf{p}}] + [\mathbf{k}_{eff} \cdot \vec{B}_1\hat{\mathbf{p}}, \mathbf{k}_{eff} \cdot (\vec{A}_3 - 2\vec{A}_2)\hat{\mathbf{r}}] \\ &= i\hbar\mathbf{k}_{eff} \cdot \left((\vec{B}_3 - 2\vec{B}_2)\vec{A}_1^T - \vec{B}_1(\vec{A}_3 - 2\vec{A}_2)^T \right) \mathbf{k} \\ &= i\hbar\mathbf{k}_{eff} \cdot (\vec{B}_1 + \vec{B}_3 - 2\vec{B}_2) \mathbf{k} \end{aligned} \quad (\text{A.74})$$

Because $\vec{A}_1 = 1$ and $\vec{B}_1 = 0$. We then get for the total phase

$$\begin{aligned} \phi_{MZ} &= \mathbf{k}_{eff} \cdot (\vec{A}_1 - 2\vec{A}_2 + \vec{A}_3) \hat{\mathbf{r}} \\ &\quad + \mathbf{k}_{eff} \cdot (\vec{B}_1 - 2\vec{B}_2 + \vec{B}_3) \left(\hat{\mathbf{p}} + \frac{\hbar\mathbf{k}_{eff}}{2} \right) \\ &\quad + \mathbf{k}_{eff} \cdot (\boldsymbol{\xi}_1 - 2\boldsymbol{\xi}_2 + \boldsymbol{\xi}_3) + (\theta_1 - 2\theta_2 + \theta_3), \end{aligned} \quad (\text{A.75})$$

where θ now represents the offset phase of the laser during the pulses. This is the result that was obtained in [6].

A.6 Eigenfunctions

We see that the interferometer signal is the expectation value of a function of several operators that are a linear combination of $\hat{\mathbf{r}}$ and $\hat{\mathbf{p}}$ (Eq. 7.25). To evaluate this signal it is thus very useful to take a look at the eigenvectors of such an operator $\hat{\phi} = \mathbf{v} \cdot \hat{\mathbf{r}} + \mathbf{w} \cdot \hat{\mathbf{p}}$. In the \mathbf{r} representation the eigenfunctions $\phi(\mathbf{r}) = \langle \mathbf{r} | \phi \rangle$ of this operator have to satisfy the differential equation

$$\hat{\phi}\phi(\mathbf{r}) = (\mathbf{v} \cdot \mathbf{r} - i\hbar\mathbf{w} \cdot \nabla)\phi(\mathbf{r}) = \Phi\phi(\mathbf{r}), \quad (\text{A.76})$$

where Φ are the eigenvalues. It is not difficult to verify that these eigenfunctions are described by a complex valued 3D-Gaussian:

$$\phi(\mathbf{r}) = e^{i(\mathbf{r}-\mathbf{r}_c) \cdot \vec{W}(\mathbf{r}-\mathbf{r}_c) + i\mathbf{p}_c \cdot \mathbf{r} / \hbar}, \quad (\text{A.77})$$

such that

$$\hat{\phi}\phi(\mathbf{r}) = \left(\left(\mathbf{v} + 2\hbar\vec{W}^T \mathbf{w} \right) \cdot \mathbf{r} - 2\hbar\mathbf{w} \cdot \vec{W}\mathbf{r}_c + \mathbf{w} \cdot \mathbf{p}_c \right) e^{i(\mathbf{r}-\mathbf{r}_c) \cdot \vec{W}(\mathbf{r}-\mathbf{r}_c) + i\mathbf{p}_c \cdot \mathbf{r} / \hbar}. \quad (\text{A.78})$$

This Gaussian $\phi(\mathbf{r})$ is thus an eigenfunction of $\hat{\phi}$ if

$$\mathbf{v} + 2\hbar\vec{W}^T \mathbf{w} = 0 \quad (\text{A.79})$$

with eigenvalues

$$\Phi = -2\hbar\mathbf{w} \cdot \vec{W}\mathbf{r}_c + \mathbf{w} \cdot \mathbf{p}_c = \mathbf{v} \cdot \mathbf{r}_c + \mathbf{w} \cdot \mathbf{p}_c. \quad (\text{A.80})$$

In the special case that the initial wavefunction is exactly equal to one of these eigenfunctions, the expectation value of any operator that is a function of $\hat{\phi}$ can be obtained by simply replacing the operators $\hat{\mathbf{r}}$ and $\hat{\mathbf{p}}$ with their initial expectation value \mathbf{r}_c and \mathbf{p}_c . In all other case one has to average over all eigenfunctions with the appropriate weighting factors.

The matrix \vec{W} as set by Equation A.79 can be obtained from

$$2\hbar\vec{W}^T = -\frac{\mathbf{v} \otimes \mathbf{w}^T}{\mathbf{w} \cdot \mathbf{w}} + \alpha_1 \otimes \mathbf{w}_{\perp,1}^T + \alpha_2 \otimes \mathbf{w}_{\perp,2}^T, \quad (\text{A.81})$$

where the notation \otimes is used for a direct product to emphasize the difference with the inner product. The vectors $\mathbf{w}_{\perp,i}$ are perpendicular to \mathbf{w} and the vectors α_i can be chosen freely. In the simplest form $\alpha_i = \mathbf{0}$ the matrix \vec{W} is a projection from \mathbf{w} to \mathbf{v} but to make \vec{W} invertible, the other components have to be added. It was verified that the choices of α_i have no effect on the calculated phases.

One can create a complete set of eigenfunctions with the free parameter \mathbf{p}_c such that any function can be expanded in terms of these eigenfunctions with coefficients

$$\tilde{f}(\mathbf{p}_c) = \int_{-\infty}^{\infty} d\mathbf{r}^3 f(\mathbf{r}) e^{-i(\mathbf{r}-\mathbf{r}_c)\vec{W}(\mathbf{r}-\mathbf{r}_c) - i\mathbf{p}_c \cdot \mathbf{r}/\hbar}. \quad (\text{A.82})$$

The expansion of the original wavefunction in these eigenfunctions is thus a modified Fourier transform.

For the calculations of the interferometer signal, we will be mostly interested in the transformation of one basis function $|\phi_1\rangle$ to the set of eigenfunctions $\{|\phi_2\rangle\}$ of a different operator $\hat{\phi}$ with different width \vec{W}_2 . For this transformation we have to calculate the overlap between all of these eigenfunctions, which is done by using the \mathbf{r} representation (Eq. A.77). There is no restriction on the parameter \mathbf{r}_c so we will take this to be zero in the following (this has no effect on the overlap integral).

$$\begin{aligned} \langle \phi_1(\mathbf{p}_1) | \phi_2(\mathbf{p}_2) \rangle &= \int_{-\infty}^{\infty} d\mathbf{r}^3 \langle \phi_1(\mathbf{p}_1) | \mathbf{r} \rangle \langle \mathbf{r} | \phi_2(\mathbf{p}_2) \rangle \\ &= \int_{-\infty}^{\infty} d\mathbf{r}^3 e^{i\mathbf{r}\vec{W}_1\mathbf{r} + i\mathbf{p}_1 \cdot \mathbf{r}/\hbar} e^{-i\mathbf{r}\vec{W}_2\mathbf{r} - i\mathbf{p}_2 \cdot \mathbf{r}/\hbar} \\ &= \int_{-\infty}^{\infty} d\mathbf{r}^3 e^{i\mathbf{r}\vec{W}_{12}\mathbf{r} + i\mathbf{p}_{12} \cdot \mathbf{r}/\hbar} \\ &= \int_{-\infty}^{\infty} d\mathbf{r}^3 e^{i\left(\mathbf{r} + \vec{W}_{12}^{-1} \mathbf{p}_{12}/2\hbar\right)\vec{W}_{12}\left(\mathbf{r} + \vec{W}_{12}^{-1} \mathbf{p}_{12}/2\hbar\right) - i\mathbf{p}_{12}\vec{W}_{12}^{-1} \mathbf{p}_{12}/4\hbar^2} \end{aligned}$$

$$\begin{aligned}
&= e^{-i\mathbf{p}_{12}\vec{W}_{12}^{-1}\mathbf{p}_{12}/4\hbar^2} \int_{-\infty}^{\infty} d\mathbf{r}'^3 e^{i\mathbf{r}'\vec{W}_{12}\mathbf{r}'} \\
&= e^{-i\mathbf{p}_{12}\vec{W}_{12}^{-1}\mathbf{p}_{12}/4\hbar^2} \left(\det \vec{W}_{12}\right)^{-1/2} \int_{-\infty}^{\infty} d\mathbf{r}''^3 e^{i\mathbf{r}''\cdot\mathbf{r}''} \\
&= e^{-i\mathbf{p}_{12}\vec{W}_{12}^{-1}\mathbf{p}_{12}/4\hbar^2} \left(\det \vec{W}_{12}\right)^{-1/2} (i\pi)^{\frac{3}{2}}, \tag{A.83}
\end{aligned}$$

where the index 12 indicates the difference 1-2 and det is the determinant of the matrix.

References

- [1] T.L. Gustavson, P. Bouyer and M.A. Kasevich, *Phys. Rev. Lett.* **78** 2046 (1996).
- [2] A. Peters, K.Y. Chung and S. Chu, *Nature* **400** 849 (1999).
- [3] S. Baessler *et al.*, *Phys. Rev. Lett.* **83** 3585 (1999).
- [4] Bordé Ch. J., *Propagation of Laser Beams and of Atomic Systems*, Les Houches Lectures, Session LIII (1990).
- [5] Bordé Ch. J., *Metrologia*, **39**, 435 (2002).
- [6] Bordé Ch. J., *J. Opt. B: Quant. Semiclass. Opt.* **5**, S199 (2003).
- [7] C. Lämmerzahl and Ch. J. Bordé, *Phys. Lett. A* **203**, 59-67 (1995).
- [8] B. Young *et al* in *Atom Interferometry*, (Academic Press, New York, 1997) (ed P. Berman), p366.
- [9] A. Peters, *High precision gravity measurements using atom interferometry* Ph.D. thesis, Stanford University (1998).
- [10] B.G. Adams, *Algebraic approach to simple quantum systems* (Springer, Berlin, 1994), p18
- [11] C. Cohen-Tannoudji, B. Diu and F. Laloe, *Quantum Mechanics Vol 1* (Wiley Interscience 1977), p174.

Chapter 8

Concluding Remarks

This thesis describes the work that was done in preparation for an atom interferometer. Although we did not succeed in getting the interferometer fully operational within the available time, the construction is basically finished and the interferometer is ready for the first tests. Apart from the construction of the setup, a lot of insight has been obtained that should help greatly to get the interferometer operational. At the same time this knowledge can help in the design of other future experiments.

One crucial development is the insight into the acceptance angle with atomic Bragg scattering. In this thesis we develop a relatively simple two-state model that gives an analytical expression for the acceptance angle. This expression allows for a direct optimization of the laser parameters that allows the interferometer to use the maximum number of atoms.

A second important contribution of this thesis is the calculation of the interferometer phase and the sensitivity to all parameters of the setup. The expressions that are obtained from these calculations allow for an easy estimate of the required alignment precision and stability when a disturbance is present in the form of a non-uniform field that interacts with the atoms or a kinetic effect such as rotation of the setup. Although the numerical values are given for the earth's rotation and gravitational field, the calculations are equally valid for any other interaction potential that is maximally quadratic as a function of position. Fields that are studied with an atom interferometer, however, are often more localized and are thus not included in the calculations. If these fields are highly localized, with a very short interaction time, their effect can be approximated with an additional phase factor without a further modification of the atomic wavefunction. More extended fields that are maximally quadratic over a given interaction region can be accounted for by a straight forward extension of the method described in this thesis by the introduction of additional sections in the interferometer. Perturbing fields on the other hand are usually not localized and their effect is very well estimated by the calculations.

From the calculations we find that there are several parameters that have to be very stable or aligned very precisely to obtain an interference signal. The dominant source of phase noise is the relative motion of the retroreflecting mirrors of the standing light waves transverse to the propagation of the atoms. This is already suppressed by passive isolation and an active feedback loop on the position of the third mirror.

Other sources of noise in the interferometer phase arise from the statistical spread in atomic parameters. The effect of these fluctuations can be greatly reduced by an optimal

alignment of the three standing waves. We find that (for 5th order Bragg scattering and 98% contrast) the angles around the atoms propagation axis have to be identical to within $17 \mu\text{rad}$ and the difference in length between the two interferometer sections can not be larger than $23 \mu\text{m}$. These are very high demands that are not easy to meet. For alignment of the laser angles we can use the 2D-detector that has an angular resolution of approximately $50 \mu\text{rad}$ (at 2 m distance). The longitudinal position of the mirrors will have to be set with an accurate ruler. Neither of these two methods have the required accuracy but they should be able to set the alignment to within one order of magnitude. The correct settings then have to be found by a 2D search within the remaining error margins (scanning the position and angle of one mirror is sufficient). It should be noted that the required contrast for the mentioned parameter values is relatively high. Probably, a contrast of 50% (this depends on the actual amount of noise in the setup and the used integration time) is enough to see an interference signal which would alleviate the demands on the alignment accuracy by a factor of 5. It is possible to increase the margins of error by decreasing the divergence and the width of the atom beam. This, however, goes at the expense of the beam flux and therefore slows the data collection and the alignment process. The margins can also be increased by a factor of 5 by taking only first order Bragg scattering. The best approach is then probably to start at first order diffraction and increase the order and the alignment accuracy in an iterative manner.

A serious concern for the alignment procedure is the low beam flux. During the alignment procedure one optimizes the interference contrast. A measurement of the contrast however requires a scan over one full fringe, e.g, by scanning the position of one of the mirrors to determine the maximum and the minimum flux in an output port. In the ideal case that everything is stable ~ 10 data points per fringe would suffice with 100 atoms per point for an signal to noise ratio of 10. One such scan would then already take a several (~ 10) seconds with a flux of 100 atoms per second. Even a relatively small 2D scan can thus become an arduous task. It is therefore imperative to have the atom flux as high as possible. There are two possibilities for this. The first option is to increase the diameter of the second collimating aperture. The maximum transverse velocity is now 0.1 photon recoil while a maximum of 0.5 recoil still gives a clean 2 path interferometer. The second option is to optimize the alignment and operation of the MOC. At this moment it is very difficult to optimize the many parameters of the MOC with only the total flux count as a feedback parameter. A permanent 2D detector in front of the second collimating aperture would be of considerable help. An idea for this that came up recently is to place a metal plate (with a small hole for transmission to the last aperture) under 45 degrees in the atom beam and accelerate all the electrons that are emitted from its surface with a strong electric field to an MCP plus phosphor screen perpendicular to the atom beam. If the electric field is strong enough the electrons go straight to the MCP and give a direct image of the atom beam.

With some luck it takes a few days to get the interferometer operational and see the first interference fringes. The first important measurements are then an experimental verification of the results of the presented theory. The phase term that involves the initial position of the atom is of special interest as this phase might give some insight in the spatial coherence of our atom beam. Because of technical difficulties with the high finesse cavity

it will still take a lot of work before the interferometer can be used for its original goal. However, there are a lot of other interesting experiments that can be performed with only slight modifications. A few examples exploit the high sensitivity of our interferometer to measure properties of helium like its electric polarisability or the quadratic Zeeman effect. Other possibilities are the use of a newly developed scheme to split the atom in three paths and to study the possible advantages of a three path interferometer.

Summary

Atom Interferometry with Cold Metastable Helium

This thesis describes the atom interferometer that is being constructed in the Coherence and Quantum Technology group at the Technische Universiteit Eindhoven (Eindhoven University of Technology). This interferometer is designed to have a macroscopic separation of several millimeters between the two paths which allows objects and fields to be inserted into the paths separately. One of the planned experiments is to place a high finesse optical cavity in one of the arms. The electromagnetic field inside the cavity induces a phase shift on the atomic wavefunction which is measured by the interferometer. By using a high quality cavity the phase shift of even a single photon can be measured. This way we can study the quantum properties of the electromagnetic field inside the cavity.

This thesis describes preparations for this interferometer. The preparations can be divided in three stages. The Chapters 2, 3 and 4 describe the preparation of the atom beam. The requirements of a clean two-path interferometer with a clear interference signal pose some severe restrictions on the atom beam. These requirements are met by using a setup that comprises four laser cooling sections, followed by an additional transverse velocity selection stage. The four laser cooling sections are designed to consecutively cool, slow, focus and compress the atom beam that emerges from a supersonic expansion. After the two final collimating apertures, we obtain a beam of metastable helium which has a transverse velocity spread of 0.1 photon recoil (9 mm/s), a well-defined longitudinal velocity (250 ± 2 m/s) and a total flux of ~ 100 /s.

The second ingredient for the interferometer is a coherent beam splitting mechanism. In this interferometer we use atomic Bragg scattering on a standing light wave. In this process, the atoms are specularly reflected on the node planes of the standing wave if the angle between the laser and the atom beam is such that the change in atomic momentum is equal to an even number of photon momenta. In Chapter 5 we investigate how the maximum number of reflected atoms changes if the laser angle is slightly misaligned from this condition. It was found that each diffraction order has a finite range of the laser angle at which there is still a significant fraction of atoms that can be diffracted. The width of these ranges can very well be estimated by a two state model. Although the process involves the interaction of many transverse momentum states the parameters of the process can apparently be chosen such that the effective transitions are limited to two states. The two relevant states in this case are the states that adiabatically evolve

from the original and the reflected momentum state. Because of the Gaussian profile of the laser the transitions between these two levels are very well described by the Demkov model. This was confirmed by comparing the calculated acceptance angle with a large range of measurements, resulting in excellent agreement. The optimal settings for the interferometer are those at which the acceptance angle for a single order is equal to 1 photon recoil, the maximum range for single order diffraction. From the two state model we found that for this optimal acceptance angle the laser waist has to be around 0.4 mm, almost independent of the diffraction order.

The third and last step before the actual interferometer can be implemented is to make an estimate of the sensitivity of the interferometer phase and the quality of the interference signal to all parameters in the setup. This is essential to determine how stable each of the components needs to be. For these calculations we model the interferometer by four distinct spatial sections that are separated by the lasers, modeled as thin sheets. The effect of a laser on the atomic wave on the transition from one section to the next is summarized by a simple multiplication with a phase factor. The evolution of the atomic wavefunction between two laser sheets is calculated by a WKB (Wentzel-Kramers-Brillouin) approximation along the classical trajectories. The model calculates the effects of the direction of the lasers, gravity, rotation and offset position of the atom on the interferometer phase including all possible cross effects. It was found that the interferometer phase is most sensitive to the relative position of the mirrors of the three standing light waves that therefore have to be stabilized carefully relative to each other. Furthermore, we found that the tolerance on both the angle ($17 \mu\text{rad}$) and the position ($23 \mu\text{m}$) of the lasers is very small.

The final chapter of this thesis is the result of a collaboration with the group of Prof. M. Kasevich at Stanford University. They are building an atom interferometer that is to set a new limit on the equivalence principle by measuring the difference in gravitational acceleration between two species of atoms. They are aiming for a relative accuracy of 10^{-15} . However, the interferometer signal is usually interpreted with a semiclassical model in which the laser pulses are infinitely short and it is unclear to what accuracy these approximations are valid. Therefore, in the final chapter we perform a full quantum mechanical calculation of the interference signal where we account for finite length of the laser pulses. The calculations show that the interferometer phase depends on both the length of the laser pulses and the size of the initial wavefunction. For typical values of the experimental parameters these effects can lead to a phase shift that is larger than the target accuracy. Without a more detailed understanding of the origin of these phase differences, the target accuracy can not be claimed. Although a final analytical expression was not found, the procedure that was developed in this chapter provides an excellent basis for further calculations.

Samenvatting

Atoom interferometrie met koud metastabiel helium

Dit proefschrift beschrijft de atoom interferometer die wordt gebouwd in the onderzoeksgroep Coherence and Quantum Technology op de Technische Universiteit Eindhoven. Deze interferometer is ontworpen om een macroscopische opsplitsing van enkele millimeters tussen de twee paden te krijgen, zodat voorwerpen en velden in ieder pad afzonderlijk geplaatst kunnen worden. Een van de geplande experimenten is het plaatsen van een optische trilhaute met hoge finesse in een van de armen. Het elektromagnetische veld in deze trilhaute induceert een faseverschil in de atomaire golffunctie die vervolgens met de interferometer gemeten kan worden. Indien gebruik gemaakt wordt van een trilhaute met een hoge kwaliteitsfactor, kan een faseverschuiving die door een enkel foton opgewekt wordt, gemeten worden, waardoor quantum eigenschappen van het elektromagnetisch veld in de trilhaute kunnen worden bestudeerd.

Dit proefschrift beschrijft de voorbereidingen voor deze interferometer, die opgedeeld kunnen worden in drie stadia. Hoofdstukken 2, 3 en 4 beschrijven de preparatie van de atoombundel. De eis van een “schone” twee-pads interferometer met een duidelijk interferentie signaal stelt zware beperkingen aan de atoombundel. Aan deze beperkingen wordt voldaan door een opstelling die bestaat uit vier laserkoeling secties en een additionele transversale snelheidsselectie. De vier laserkoeling secties zijn ontworpen om achtereenvolgens te koelen, te vertragen, te focuseren en te comprimeren. Na twee laatste collimerende openingen resulteert een bundel van metastabiel helium met een transversale snelheidsspreiding van 0,1 maal de foton terugstoot snelheid (9 mm/s), een goed bepaalde longitudinale snelheid (250 ± 2 m/s) en een totale flux van ongeveer 100 atomen per seconde.

Het tweede benodigde ingrediënt voor de interferometer is een mechanisme om de atoombundel coherent te splitsen. In dit geval maken we gebruik van het proces van atomaire Bragg diffractie aan een staande licht golf. De atomen worden gereflecteerd op de knopen van de staande golf als de hoek tussen de atoombundel en de laser zodanig is dat de verandering van impuls precies gelijk is aan een even aantal foton terugstoten. In hoofdstuk 5 onderzoeken we hoe het maximale aantal atomen dat gereflecteerd kan worden verandert als de hoek van de laser enigszins verkeerd uitgelijnd staat ten opzichte van deze ideale hoek. We vinden dat elke diffractie orde een bereik heeft voor de laser hoek waarin een significant deel van de atomen verstrooid kan worden. De breedte van dit bereik kan erg goed afgeschat worden met een relatief eenvoudig twee-toestanden model.

Hoewel bij het totale proces vele transversale impuls toestanden betrokken zijn, kunnen de parameters blijkbaar zo gekozen worden dat de effectieve overgangen beperkt zijn tot twee toestanden. De relevante toestanden in dit geval zijn de toestanden die adiabatisch evolueren uit de impuls toestanden met de originele en de gereflecteerde impuls. Door het Gaussische profiel van de laser kunnen de overgangen tussen deze twee toestanden goed beschreven worden met het Demkov model. Dit wordt bevestigd door de metingen die goed overeen komen met de voorspellingen van dit model. De instellingen zijn optimaal voor de interferometer als de acceptantie hoek voor verstrooiing naar een enkele orde gelijk is aan één foton terugstoot. Dit is namelijk het maximale bereik voordat de atomen ook naar andere ordes verstrooid worden. Uit het twee-toestanden model vinden we dat voor deze optimale waarde een laser waist van ongeveer 0.4 mm gekozen moet worden, vrijwel onafhankelijk van de diffractie-orde.

De derde en laatste stap voor de daadwerkelijke bouw van de interferometer is een af-schatting van de gevoeligheid van de interferometer fase en de kwaliteit van het interferentie signaal voor alle parameters van de opstelling. Dit is essentieel om te bepalen hoe stabiel de verschillende onderdelen van de opstelling moeten zijn. Voor de berekeningen hebben we een model genomen waarin de interferometer opgedeeld is in vier secties die gescheiden zijn door de drie laserbundels, die voorgesteld worden als oneindig dunne vlakken. Het effect van de lasers op de atomaire golf tijdens de doorgang van een sectie naar de volgende wordt samengevat door een simpele vermenigvuldiging met een fase factor. De evolutie tussen twee lasers in wordt berekend met een WKB (Wentzel-Kramers-Brillouin) benadering langs het klassieke pad van de atomen. Het model berekent de effecten van de richting van de laserbundel, zwaartekracht, rotatie en initiële off-set positie van de atomen op de interferometer fase, inclusief alle kruistermen. We vonden dat de interferometer het gevoeligst is voor de relatieve positie van de drie spiegels van de staande golven, die daarom goed gestabiliseerd moeten worden ten opzichte van elkaar. Bovendien vonden we dat de tolerantie voor de hoek ($17 \mu\text{rad}$) en de positie ($23 \mu\text{m}$) van de lasers erg klein zijn.

Het laatste hoofdstuk van dit proefschrift is het resultaat van een samenwerking met de groep van Prof. M. Kasevich van Stanford University. Zij bouwen een atoom interferometer die een nieuwe grens moet stellen aan het equivalentie principe door het verschil in versnelling door de zwaartekracht te meten tussen twee atomen van verschillende soort. De beoogde precisie is 10^{-15} . Echter, de gebruikelijke methode om het interferentie signaal te interpreteren is gebaseerd op een semi-klassieke methode waarin de laserpulsen als oneindig kort worden beschouwd. Het is onduidelijk wat het effect van deze aannames is op de nauwkeurigheid van de metingen. Daarom worden in het laatste hoofdstuk volledig quantum mechanische berekeningen gedaan die wel een eindige lengte van de laser pulsen meenemen. Deze berekeningen laten zien dat de interferometer fase zowel van de lengte van de pulsen afhangt als van de breedte van de initiële golffunctie. Voor typische waarden van de experimentele parameters kunnen deze effecten leiden tot een verandering van de interferometer fase die groter is dan de beoogde nauwkeurigheid. Zonder een beter begrip van de oorsprong van dit faseverschil kan de beoogde nauwkeurigheid niet geclaimd worden. Hoewel een definitieve analytische uitdrukking niet verkregen kon worden, biedt de procedure die in dit hoofdstuk beschreven is een uitstekende basis voor verdere berekeningen.

Dankwoord

Bij deze wil ik graag iedereen bedanken die bijgedragen heeft aan mijn onderzoek en het tot stand komen van het proefschrift. In het algemeen bedank ik alle leden van de ex-groep AQT en het huidige CQT die ik tijdens mijn periode heb mogen meemaken voor de gezellige sfeer en de vele zeer nuttige opmerkingen en enerverende discussies. Maar er zijn ook vele mensen buiten de groep die een bijdrage hebben geleverd en die ik hiervoor hartelijk wil bedanken.

Een aantal personen wil ik nog in het bijzonder noemen; Mijn promotor Ton van Leeuwen voor de vele nuttige opmerkingen en tips over het onderzoek en mijn proefschrift en mijn tweede promotor Herman Beijerinck, voornamelijk voor zijn organisatorische inzicht. Ik bedank Kenian Domen voor een goede samenwerking van bijna 6 jaar en zijn welwillendheid om altijd geduldig mee te discussieren over de wildste theorieën en de soms vervelende problemen. Edgar Vredenbregt voor zijn onmisbare experimentele kennis en inzichten in het lab. En verder alle overige mensen die een directe bijdrage hebben geleverd aan het experiment en/of mijn proefschrift: Ton Meesters, Walter van Dijk en Wilbert Rooijackers. Dank aan Louis van Moll en Jolanda van de Ven voor de geweldige technische ondersteuning en Rina Boom voor de administratieve hulp.

Bijzondere dank ook aan Ad Kemper, bijgestaan door Harry en Wim, die zelfs met tegenwerking van bovenaf steeds bereid was voor advies, uitleg en zelfs de bouw van enkele elektronische apparaten. Terugkijkend blijkt deze samenwerking zelfs een voorbode van een fusie tussen de twee groepen.

I would also like to thank Jason Hogan and Mark Kasevich for many very helpful discussion which helped a great deal in understanding the theory of atom interferometers and the sometimes unreadable theoretical papers.

Curriculum Vitae

naam Maarten Arnoldus Hubertus Maria Jansen

29 juli 1978 geboren te Waalwijk

1990-1996 Gymnasium
Dr. Mollercollege te Waalwijk

1996-2002 Studie Technische Natuurkunde
Technische Universiteit Eindhoven
afstudeerverslag: *Preparations for the QND experiment*
o.l.v. Prof.dr. K.A.H. van Leeuwen

2002-2007 Onderzoeker in Opleiding
vakgroep Atoomfysica en Quantumelektronica
Faculteit Technische Natuurkunde
Technische Universiteit Eindhoven
(dit Proefschrift)

april-augustus 2005 werkbezoek Prof. M. Kasevich group
Stanford University
Palo Alto, Californië, USA